E.O. Paton Electric Welding Institute of the National Academy of Science of Ukraine
International Association “Welding”

The Paton Welding Journal

02
2024

International Scientific-Technical and Production Journal ◊ Founded in January 2000 (12 Issues Per Year)

Address of Editorial Board
E.O. Paton Electric Welding Institute, 11 Kazymyr Malevych Str., 03150, Kyiv, Ukraine
Tel./Fax: (38044) 205 23 90, E-mail: journal@paton.kiev.ua, patonpublishinghouse@gmail.com
https://patonpublishinghouse.com/eng/journals/tpwj

State Registration Certificate 24933-14873 ПР from 13.08.2021
ISSN 0957-798X, DOI: http://dx.doi.org/10.37434/tpwj

Subscriptions, 12 issues per year:
$384 — annual subscription for the printed (hard copy) version, air postage and packaging included;
$312 — annual subscription for the electronic version (sending issues in pdf format or providing access to IP addresses).

Representative Office of “The Paton Welding Journal” in China:
China-Ukraine Institute of Welding, Guangdong Academy of Sciences
Address: Room 210, No. 363 Changxing Road, Tianhe, Guangzhou, 510650, China.
Zhang Yupeng, Tel: +86-20-61086791, E-mail: patonjournal@gwi.gd.cn

The content of the Journal includes articles received from authors from around the world in the field of welding, cutting, cladding, soldering, brazing, coating, 3D additive technologies, electrometallurgy, material science, NDT and selectively includes translations into English of articles from the following journals, published in Ukrainian:
- Automatic Welding (https://patonpublishinghouse.com/eng/journals/as);
- Electrometallurgy Today (https://patonpublishinghouse.com/eng/journals/sem);
- Technical Diagnostics & Nondestructive Testing (https://patonpublishinghouse.com/eng/journals/tdnk).

CONTENTS

ORIGINAL ARTICLES

*Translated Article(s) from “Automatic Welding”, No. 12, 2023.

**Translated Article(s) from “Electrometallurgy Today”, No. 4, 2023.

***Translated Article(s) from “Electrometallurgy Today”, No. 4, 2023.

DOI: https://doi.org/10.37434/tpwj2024.02.01

MICROHARDNESS AND CORROSION PROPERTIES OF FRICTION STIR WELDED PHOSPHOR BRONZE

S. Gopi[1], **D.G. Mohan**[2]

[1]Department of Production Engineering, Government College of Technology
Coimbatore, Tamilnadu, India, 641013
[2]School of Engineering Faculty of Technology, University of Sunderland
England, United Kingdom - SR6 0DD

ABSTRACT

This study investigates the microhardness and corrosion properties of friction stir welded (FSW) joints in phosphor bronze ($CuSn_4$), a vital non-ferrous alloy in engineering applications. The research delves into the FSW process, employing varying welding parameters to create joints that exhibit distinct microstructural characteristics. Microhardness distribution across the FSW joints is assessed and correlated with the base material's properties. Corrosion behaviour is rigorously examined through weight loss tests, revealing insights into the susceptibility of FSW joints to various corrosive environments. The study identifies the influence of FSW parameters on microhardness and corrosion performance, thus contributing to understanding the alloy's behaviour under this welding technique. This research shows that the welding speed of 0.25 mm/s, tool rotational speed of 1100 rpm, plunger depth of 0.2 mm, and a hexagonal tool profile produce the better joint with the highest microhardness of 139 *HV* and rate of corrosion of 0.420831 %.

KEYWORDS: friction stir welding, phosphor bronze, corrosion, microhardness, joining

INTRODUCTION

Phosphor bronze, an intricately formulated bronze alloy, has garnered widespread recognition due to its exceptional amalgamation of properties. Its elevated strength and hardness render it a fitting choice for structural components that endure substantial loads. This alloy's intrinsic resistance to corrosion causes it an optimal material for marine apparatus and plumbing systems, imparting longevity and reliability to such critical installations [1]. Phosphor Bronze's inherent resistance to wear qualifies it for pivotal roles in bearings and gears, while its commendable machinability facilitates intricate shaping with ease. Notably, this alloy boasts superior thermal and electrical conductivity, a crucial attribute that finds practical utility in heat exchangers and electrical connectors. The myriad characteristics of Phosphor Bronze collectively position it as the preferred material across industries that demand a harmonious blend of strength, corrosion resistance, wear resilience, machinability, and aesthetic allure [2].

Friction Stir Welding (FSW), an innovative solid-state welding technique, has emerged as an exceedingly promising approach for joining Phosphor Bronze, presenting distinct advantages over conventional fusion welding methodologies. Operating beneath the melting threshold of the materials involved, FSW ensures the retention of Phosphor Bronze's intrinsic properties [3, 4]. This autogenous and continuous process harnesses a non-consumable spinning tool distinguished by its superior hardness relative to the Phosphor Bronze. It generates frictional heat and mechanical agitation to effectuate seamless material fusion [5, 6]. Applying FSW to Phosphor Bronze welding yields a spectrum of noteworthy benefits. By circumventing prevalent challenges inherent to fusion welding, such as oxidation and porosity, FSW orchestrates material fusion in the solid state, curtailing Phosphor Bronze's interaction with oxygen. This prudent measure averts the formation of deleterious oxide layers and porosity, resulting in immaculate welds characterised by heightened structural integrity and diminished imperfections.

Moreover, FSW affords meticulous management of heat input throughout the welding process, curbing distortion and preserving Phosphor Bronze's mechanical attributes [7]. The absence of filler metals simplifies the welding procedure, concurrently curtailing material expenses. Additionally, the mechanical agitation intrinsic to FSW promotes material homogenisation, fortifying joint strength and integrity [8]. As applied to Phosphor Bronze welding, FSW's salient virtues engender it as an enticing alternative to fusion-based welding methodologies across various applications. The solid-state predilection of FSW underscores the safeguarding of material properties, engendering superior control over the heat-affected zone (HAZ) while mitigating thermal distortion.

Besides, the obviation of fusion-induced flaws, exemplified by solidification cracks, augments overall weld joint robustness and endurance [9]. These attributes bear heightened significance when considering Phos-

Table 1. Chemical compositions of $CuSn_4$

Cu, %	Sn, %	Zn, %	Fe, %	P, %	Ni, %	Si, %	Mn, %
96.32	3.45	0.1	0.012	0.740	0.012	0.063	0.0072

phor Bronze, a material hailed for its distinct mechanical and corrosion-resistant traits. The amelioration of typical concerns associated with fusion welding, encompassing oxidation and porosity, culminates in high-calibre welds distinguished by augmented structural integrity and elevated corrosion resistance [10]. The deployment of FSW in welding Phosphor Bronze has the potential to significantly enhance performance and dependability across industries reliant on welded components.

Nevertheless, a conspicuous research void remains in FSW applied to Phosphor Bronze joining. In addressing this lacuna, this research explores the intricacies of joining phosphor bronze through FSW techniques. This study's primary focus lies in the exhaustive analysis of microhardness and corrosion properties — a comprehensive exploration offering invaluable insights into the efficacy and aptness of these welding methodologies vis-à-vis the unique attributes of phosphor bronze. Through this pursuit, a definitive stride is taken towards expanding the frontiers of knowledge surrounding the application of FSW to enrich phosphor bronze's role in many industrial applications.

EXPERIMENTAL METHODOLOGY

This research work was carried out using a phosphor bronze (CuSn4). To facilitate the examination, plates having dimensions of 4mm in thickness, 100 mm in length, and 50mm in width were chosen for FSW. The resultant welds assumed the form of butt joints, meticulously crafted along the axis of lamination under standard atmospheric conditions [11]. The chemical compositions of the specimens have been given in Table 1.

The FSW procedures were executed utilising a vertical milling machine, thereby furnishing a stable and meticulously controlled platform to facilitate the welding process. A non-consumable carbide tool was selected for these operations, with a pin length of 3.6 mm and a pin diameter of 2.6 mm, encompassing three distinct pin profiles — square, pentagon, and hexagon and the shoulder, with a diameter of 25 mm and a flat face, was employed [12]. This rigorous selection process aims to ensure optimal efficacy within this study. A singular-pass welding methodology was used to uphold uniformity and mitigate potential disparities, thereby generating joints of consistent quality and fostering dependable scrutiny of ensuing weld attributes. The definitive process parameters were established post iterative trials and a thorough review of pertinent literature. Consequently, the finalised FSW parameters encompassed a welding speed of 0.25 mm/s, a tool rotational speed of 1100 rpm, a plunge depth of 0.2 mm, and the utilisation of three distinct tool profiles — square, pentagon, and hexagon, each bearing a flat shoulder. Figure 1 shows the FSW process on phosphor bronze plates.

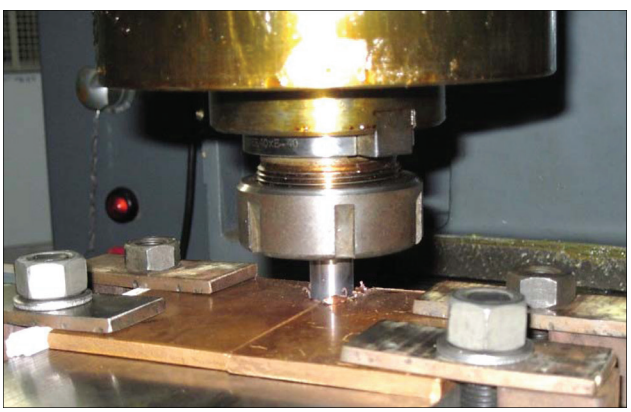

Figure 1. FSW setup with phosphor bronze plates

The FSW joints were subjected to meticulous sectioning along the transverse direction to enable an exhaustive assessment. This controlled sectioning procedure effectively segregated the weld bead and the HAZ from the parent alloy, which is essential for nuanced evaluation. In preparation for corrosion testing, the specimens were meticulously embedded within epoxy resin, thereby confining exposure exclusively to the welded surface, a prerequisite for precise corrosion behaviour evaluation. The specimens underwent successive polishing with emery papers, culminating at a grit size of 1000, thereby guaranteeing the elimination of any extraneous surface impurities or irregularities. Subsequently, a specialised degreaser was employed, achieving a smooth, pristine surface conducive to subsequent characterisation and evaluation. Adhering to ASTM E384 standards, microhardness assessments were systematically conducted for all weldments [13].

Further advancing the analytical process, a weight loss corrosion test was executed in adherence to ASTM G31 standards. The subsequent immersion of the joints' weld zones within 3.5 wt.% sodium chloride solution transpired in individual 500 ml beakers maintained at ambient temperature [14]. This strategic approach provides accurate insights into the corrosion behaviour of the joint.

RESULTS AND DISCUSSION

The FSW operations were performed on a vertical milling machine, providing a stable and controlled platform for the welding process. A non-consumable carbide tool with a pin length of 3.6 mm, a pin diameter of 2.6 mm with three different pin profiles (square, pentagon and hexagon) and a shoulder diameter of 25 mm with a flat face is adopted for this work [15]. Specimen S1

used a square pin profile, S2 used a hexagon pin profile, and S3 used pentagon pin profiles for the FSW process. A single-pass welding technique was employed to fabricate the joints, ensuring uniformity and enabling reliable analysis of the resulting weld characteristics. The process parameters are finalised after conducting trial runs and a literature review. The process parameters selected for FSW are weld speed of 0.25 mm/s, tool rotational speed of 1100 rpm, plunge depth of 0.2 mm and three different tool profiles, square, pentagon and hexagon with flat shoulder.

The FSW joints were carefully sectioned in the transverse direction to obtain representative specimens for analysis. The sectioning process involved cutting along the welding direction, effectively separating the weld bead and the HAZ from the parent alloy. In order to conduct corrosion testing, the specimens were embedded in epoxy resin, ensuring that only the welded surface was exposed to the salt solution, thereby facilitating an accurate assessment of the corrosion behaviour [16]. The specimens were initially cleaned using emery papers up to a grit size of 1000, ensuring the removal of any surface impurities or irregularities. Finally, a degreaser was applied to achieve a smooth and pristine surface, ready for subsequent characterisation and evaluation. Microhardness was conducted for all the weldments made with the optimised input variables following ASTM E384 standards. The weight loss corrosion test was conducted per ASTM G31 standards. After cleaning, the metal samples are blow-dried and weighed. After initial weighing of all the FSW samples, they were suspended, and the weld zones were immersed into 500 ml beakers containing 3.5 wt.% sodium chloride solution separately at room temperature.

In the current Fabricated Friction Stir Welding (FFSW) joints investigation, dissecting and addressing two distinct phenomena inherently yield disparate outcomes is imperative. The first of these phenomena centres around the temperatures to which the materials are subjected during welding. Although these temperatures remain below their respective melting points, the consequences on mechanical properties are undeniable. This influence extends across critical regions, including the nugget, Thermal-Mechanically Affected Zone (TMAZ), and HAZ.

Conversely, the second phenomenon hinges upon the substantial shear stresses engendered by the dynamic motion of the welding tool. This mechanical agitation induces the formation of an exceedingly refined microstructure, a phenomenon prominently manifested within the nugget zone and predominantly evident within the flow arm zone. The outcome is a partial restoration of mechanical properties, marking a discernible pattern of variation as one traverses from the central axis of the weld bead, traverses the TMAZ, and transitions into the HAZ. An intriguing aspect comes to the fore when investigating FSW joints in phosphor bronze alloys akin to those scrutinised herein, as exemplified by the S2 sample [17]. Here, the relatively lower temperatures endured during the welding process can incite a form of ageing that, in turn, leads to a modest yet discernible enhancement in mechanical characteristics.

Ascertaining corrosion properties is integral to this inquiry, where the mass of specimens before and after corrosion, coupled with corresponding percentage weight losses, is provided in Table 2. This calculation of corrosion-induced weight loss aligns with the established rate of corrosion formulas. The pre-corrosion and post-corrosion masses of the welds are judiciously measured, and the resultant weight loss is presented as a percentage relative to the parent weld's mass. The data in Table 2 shows the corrosion behaviour exhibited by the specimens subjected to the weight loss test. A notable trend emerges, notably the substantially lower weight loss attributed to corrosion in FSW samples such as S2, as discerned through meticulous analysis over a 14-day duration [18].

Of particular significance, the representative FSW weld, Specimen S2, exhibits an admirably lesser weight loss of 0.420831 %, a distinctive marker of high corrosion resistance. Corrosion behaviour is governed by an array of factors encompassing temperature, corrosive agent concentration, diffusion rates, and the presence of oxidising agents [19]. These determinants collectively dictate a material's susceptibility to corrosion processes. Beyond these well-established influences, the corrosion resistance of metals is linked to microstructural attributes.

Precisely, the grain size and the presence of precipitated particles wield significant sway over material corrosion properties. A finer grain structure, often achievable through the unique thermomechanical conditions inherent to FSW, can potentiate augmented corrosion resistance by reduced grain boundary pres-

Table 2. Mass of the specimens before and after corrosion of weight loss, %

Specimens	Mass before corrosion, g	Mass after corrosion, g	Weight loss due to corrosion, %
S1 (Square pin)	14.489	8.1265	0.439126
S2 (Hexagon pin)	16.888	9.7810	0.420831
S3 (Pentagon pin)	14.566	7.9640	0.453247

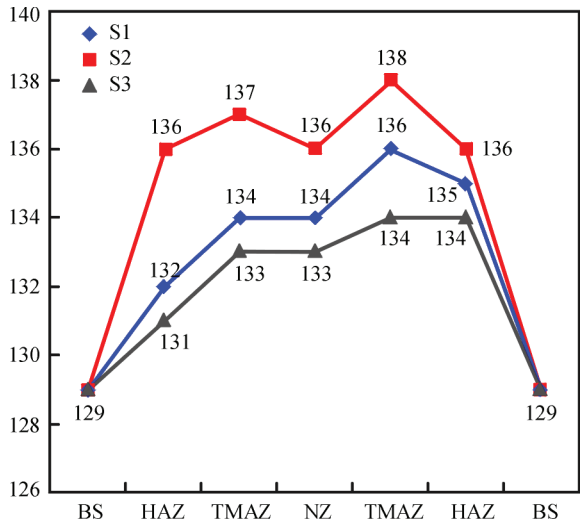

Figure 2. Microhardness of FSW specimen

ence and the concomitant curbing of preferential sites for corrosion initiation [20, 21]. Additionally, the impact of precipitated particles, including second-phase and precipitates stemming from the welding process, cannot be understated. These entities can significantly influence local electrochemical behaviour, subsequently modifying a material's corrosion susceptibility. The amalgamation of grain size refinement and precipitate formation in FSW-welded materials contributes to the heightened corrosion performance observable in Specimen S2.

Conversely, the data elucidated within Table 2 accentuates the remarkable corrosion resistance manifested in the FSW specimens, with Specimen S2 serving as a poignant exemplar in contrast to alternative joints. Although factors such as temperature and chemical environment retain their cardinal roles in corrosion, the salient contribution of microstructural attributes — precisely grain size and precipitate presence — must not be trivialised [22]. This comprehensive comprehension of corrosion behaviour is instrumental in optimising welding processes to elevate material performance and longevity within corrosive settings.

All experimental undertakings involving friction stir were meticulously orchestrated under controlled ambient conditions, maintaining a steady temperature of 30 °C. In the context of the FSW specimens, a notable thermal polarity becomes evident, with the advancing side (AS) registering heightened heat generation relative to the retreating side (RS). This distinctive phenomenon is attributed to the rotational dynamics of the tool, orchestrating the movement of relatively colder material from the AS to the RS. Accordingly, when effecting the fusion of phosphor bronze, strategic placement of the alloy material within the RS is judiciously employed to harness enhanced strength generation at the AS, thereby fostering comprehensive mechanical robustness within the welded interconnections [23]. A graphical representation of average microhardness attributes within butt joints constructed from phosphor bronze through FSW is elegantly presented in Figure 2.

Prominently, Sample S2 emerges as a beacon of elevated joint tensile strength. This pinnacle achievement is underscored by the implementation of specific parameters, notably a tool rotation rate of 1100 rpm, a welding speed of 0.25 mm/s, and a plunge depth of 0.2 mm. Specimen S2 attains the average microhardness of 137 *HV*. It is discernible that the retreating side distinctly boasts heightened microhardness within the TMAZ region, a consequence of the complex interplay between thermomechanical dynamics and resultant grain modification within this domain [24].

CONCLUSION

This study comprehensively explores microhardness and corrosion attributes in FSW joints using phosphor bronze ($CuSn_4$). The study effectively elucidates FSW parameter impact on microhardness and corrosion, enhancing understanding of alloy behaviour in this welding context.

Notably, optimal parameters of welding speed (0.25 mm/s), tool rotational speed (1100 rpm), plunge depth (0.2 mm), and hexagonal tool profile yield exceptional outcomes. These parameters engender superior microhardness (139 *HV*) and minimal corrosion rate (0.420831 %), showcasing their instrumental role in attaining favourable joint attributes.

This study underscores FSW's profound influence on microhardness and corrosion in phosphor bronze joints while highlighting the strategic orchestration of welding parameters. This contribution augments the evolving understanding of FSW's potential, refining material attributes for targeted performance prerequisites.

REFERENCES

1. Hu, D., Chen, M., Wang, L. et. al. (2016) Dynamic tensile behaviour and deformational mechanism of C5191 phosphor bronze under high strain rates deformation. *Materials Sci. and Eng.: A*, **649**, 68–73. DOI: https://doi.org/10.1016/j.msea.2015.09.075
2. Khan, N.Z., Siddiquee, A.N., Khan, Z.A. et. al. (2021) Improvement in joint efficiency with high productivity and narrow weld formation in friction stir welding. Proceedings of the Institution of Mechanical Engineers, Pt E. *J. of Process Mechanical Eng.*, 095440892110424. DOI: https://doi.org/10.1177/09544089211042480
3. Zoeram, A.S., Anijdan, S.H.M., Jafarian, H.R. et. al. (2017) Welding parameters analysis and microstructural evolution of dissimilar joints in al/bronze processed by friction stir welding and their effect on engineering tensile behavior. *Materials Sci. and Eng.: A*, **687**, 288–297. DOI: https://doi.org/10.1016/j.msea.2017.01.071

4. Mohan, D.G., Wu, C. (2021) A review on friction stir welding of steels. *Chinese J. of Mechanical Eng*., 34(**1**). DOI: https://doi.org/10.1186/s10033-021-00655-3
5. Rabiezadeh, A., Salafzon, A., Mostafavi, N. (2023) Dissimilar welding of AA5083/AA7039 by self-reacting friction stir welding. *J. of Adhesion Sci. and Technology*, 1–22. DOI: https://doi.org/10.1080/01694243.2023.2219367
6. Sasikumar, A., Gopi, S., Mohan, D.G. (2022) Prediction of filler added friction stir welding parameters for improving corrosion resistance of dissimilar aluminium alloys 5052 and 6082 joints. *Advances in Materials Sci.*, 22(**3**), 79–95. DOI: https://doi.org/10.2478/adms-2022-0014
7. Yin, K., Cao, L., Wang, N. (2019) Mechanical properties and residual stresses of 5083 to AM60B dissimilar friction stir welding with different process parameters. *J. of Adhesion Sci. and Technology*, 33(**23**), 2615–2629. DOI: https://doi.org/10.1080/01694243.2019.1653593
8. Çam, G. (2011) Friction stir welded structural materials: Beyond al-alloys. *Inter. Materials Reviews*, 56(**1**), 1–48. DOI: https://doi.org/10.1179/095066010x12777205875750.
9. Shokri, V., Sadeghi, A., Sadeghi, M. H. (2017) Effect of friction stir welding parameters on microstructure and mechanical properties of DSS–cu joints. *Materials Sci. and Eng.: A*, **693**, 111–120. DOI: https://doi.org/10.1016/j.msea.2017.03.054
10. Liu, H. J., Shen, J. J., Zhou, L., et. al. (2011) Microstructural characterisation and mechanical properties of friction stir welded joints of aluminium alloy to copper. *Sci. and Technology of Welding and Joining*, 16(**1**), 92–98. DOI: https://doi.org/10.1179/1362171810y.0000000007
11. Vinith, B., Dharshan, S. A., Aravind, S. et. al. (2023) Friction stir welding evolution, hybrid technologies and shoulder shape. *Inter. J. on Interactive Design and Manufacturing*, 17(**4**), 1443–1458. DOI: https://doi.org/10.1007/s12008-023-01208-9
12. Mohan, D. G., Tomków, J., Gopi, S. (2021). Induction assisted hybrid friction stir welding of dissimilar materials AA5052 aluminium alloy and X12Cr13 stainless steel. *Advances in Materials Sci*., 21(**3**), 17–30. DOI: https://doi.org/10.2478/adms-2021-0015
13. Wang, Q., Zhou, X., Wang, B. et. al. (2023) Accelerated role of exogenous riboflavin in Selective desulfovibrio desulfuricans corrosion of pipeline welded joints. *Bioelectrochemistry*, **153**, 108469. DOI: https://doi.org/10.1016/j.bioelechem.2023.108469
14. Liu, P., Li, Y., Geng, H. et. al. (2007) Microstructure characteristics in TIG welded joint of Mg/Al dissimilar materials. *Materials Letters*, 61(**6**), 1288–1291. DOI: https://doi.org/10.1016/j.matlet.2006.07.010
15. Gopi, S., Mohan, D.G. (2021) Evaluating the welding pulses of various tool profiles in single-pass friction stir welding of 6082-T6 aluminium alloy. *J. of Welding and Joining*, 39(**3**), 284–294. DOI: https://doi.org/10.5781/jwj.2021.39.3.7
16. Yelamasetti, Balrm, Adithya, G.S., Ramadevi, R.S. et. al. (2023) Metallurgical, mechanical and corrosion behaviour of pulsed and constant current TIG dissimilar welds of Aisi 430 and Inconel 718. *J. of Materials Research and Technology*, **24**, 6652–6664. DOI: https://doi.org/10.1016/j.jmrt.2023.04.231
17. Tamadon, A., Pons, D.J., Clucas, D. (2020) Analogue modelling of flow patterns in bobbin friction stir welding by the dark-field/bright-field illumination method. *Advances in Materials Sci.*, 20(**1**), 56–70. DOI: https://doi.org/10.2478/adms-2020-0003
18. Yelamasetti, Balram, Vardhan, T.V., Ramana, G.V. (2020) Study of metallurgical changes and mechanical properties of dissimilar weldments developed by interpulse current TIG welding technique. Proceedings of the Institution of Mechanical Engineers, Pt C: *J. of Mechanical Eng. Sci*., 235(**16**), 2985–2997. DOI: https://doi.org/10.1177/0954406220960780
19. Xuan, Y., Yang, J., Liu, H. et. al. (2020) Microstructure and mechanical properties of Invar36 alloy joints using keyhole TIG welding. *Sci. and Technology of Welding and Joining*, 25(**8**), 712–718. DOI: https://doi.org/10.1080/13621718.2020.1830545
20. Dhondt, M., Aubert, I., Saintier, N. et. al. (2011) Intergranular stress corrosion cracking of friction stir welded nugget on a 2050-T8 aluminum alloy. *Advances in Materials Sci.*, 11(**3**). DOI: https://doi.org/10.2478/v10077-011-0016-6
21. Kusano, K., Watanabe, H. (2002) Recent trends in development of high-efficiency TIG welding; high-deposition TIG welding and ultranarrow-gap TIG welding. *Welding Inter.*, 16(**12**), 986–991. DOI: https://doi.org/10.1080/09507110209549651
22. Dudzik, K., Jurczak, W. (2015) Influence of friction stir welding on corrosion properties of AW-7020M alloy in sea water. *Advances in Materials Sci.*, 15(**1**), 7–13. DOI: https://doi.org/10.1515/adms-2015-0002
23. Zhou, D., Xia, Y., Gao, Z. et. al. (2023) Effect of loading conditions on corrosion fatigue process of FSW AA6061-T6 joint in 3.5 % NaCl studied by electrochemical noise. *J. of Materials Research and Technology*, **24**, 9808–9823. DOI: https://doi.org/10.1016/j.jmrt.2023.05.179
24. Qiu, Y., Yang, X., Xu, J. et. al. (2022) Enhanced mechanical property and corrosion resistance of alloy 5182 fsw joints by SC and ZR alloying. *Materials Characterization*, **194**, 112412. DOI: https://doi.org/10.1016/j.matchar.2022.112412

ORCID
S. Gopi: 0000-0002-4652-4198,
D.G. Mohan: 0000-0001-7966-1853

CONFLICT OF INTEREST
The Authors declare no conflict of interest

CORRESPONDING AUTHOR
D.G. Mohan
School of Engineering Faculty of Technology,
University of Sunderland, England,
United Kingdom - SR6 0DD.
E-mail: dhanesh.mohan@sunderland.ac.uk

SUGGESTED CITATION
S. Gopi, D.G. Mohan (2024)
Microhardness and corrosion properties of friction stir welded phosphor bronze. *The Paton Welding J*., **2**, 3–7.

JOURNAL HOME PAGE
https://patonpublishinghouse.com/eng/journals/tpwj

Received: 23.08.2023
Received in revised form: 26.12.2023
Accepted: 31.01.2024

DOI: https://doi.org/10.37434/tpwj2024.02.02

INFLUENCE OF PREHEATING ON TIG WELDING THERMAL CYCLE OF HIGH-TEMPERATURE TITANIUM ALLOY OF Ti–Al–Zr–Sn–Mo–Nb–Si SYSTEM

R.V. Selin[1], **V.Yu. Bilous**[1], **S.B. Rukhanskyi**[1], **I.B. Selina**[2], **L.M. Radchenko**[1]

[1]E.O. Paton Electric Welding Institute of the NASU
11 Kazymyr Malevych Str., 03150, Kyiv, Ukraine
[2]National Technical University of Ukraine "Igor Sikorsky Kyiv Polytechnic Institute"
37 Prospect Beresteiskyi (former Peremohy), 03056, Kyiv, Ukraine

ABSTRACT

The main direction of improving the operational characteristics of titanium alloys is creation of heat-resistant and high-temperature titanium alloys. The high specific strength and corrosion resistance of this type of alloys at temperatures up to 500–600 °C, enables making them the main structural material for aircraft and rocket engineering. However, their widespread use is associated with the problem of precipitation of brittle phases during welding, which requires additional technological operations, such as local heat treatment or preheating. In this paper, the finite element modeling method was applied to study the influence of the TIG welding thermal cycle of high-temperature titanium alloy of Ti–6.5Al–5.3Zr–2.2Sn–0.6Mo–0.5Nb–0.75Si system with and without the use of preheating and to plot the cooling rate diagrams of the produced welded joints.

KEYWORDS: high-temperature titanium alloy, TIG welding, finite element modeling, preheating

INTRODUCTION

Owing to a unique combination of physical and mechanical characteristics, titanium alloys are one of the most promising structural materials. Continuous expansion of production and application of titanium in different technology fields is due, first of all, to its higher specific strength (ratio of ultimate strength to density). Excellent corrosion resistance of titanium under atmospheric conditions, in sea water and other environments determines its effective application for fabrication of various structures [1]. The main direction of further improvement of mechanical and service properties of titanium alloys is creation of new generation high-temperature titanium alloys, doped by refractory elements, such as niobium. High specific strength and corrosion resistance of alloys of this type at up to 500–600 °C temperatures allows making them the main structural material for aircraft and rocket engineering. Their wide application, however, is related to poor weldability, which requires taking additional technological measures, such as pre- or concurrent heating and postweld heat treatment. Application of mathematical modeling of the welding thermal cycle allows establishing the cooling rate distribution, determination of the structural-phase state of metal of the weld and HAZ, optimizing the conditions of phase transformation occurrence due to application of welding modes with higher values of energy input or use of preheating, in order to form the state required for achieving higher mechanical properties of welded joints, and possible improvement of welding operation productivity [2].

Table 1. Chemical composition of the high-temperature titanium alloy

Ti	Al	Zr	Sn	Mo	Nb	Si
Base	6.5	5.3	2.2	0.6	0.5	0.75

OBJECTIVE OF THE WORK

is to study the peculiarities of the influence of thermal cycle of tungsten electrode argon-arc (TIG) welding with preheating on the shape and size of the penetration zone and HAZ, as well as distribution of cooling rates in the metal of the weld and HAZ.

INVESTIGATION MATERIALS AND METHODS

Investigation of the influence of thermal cycle of TIG welding with preheating was conducted for high-temperature titanium alloy, the chemical composition of which is given in Table 1 [3, 4].

Computational study of the influence of welding thermal cycle on the structural-phase state of welded joints on two-phase titanium alloys was performed using a nonstationary thermal finite element analysis, taking into account the heat of phase transition. Mathematical modeling of TIG welding was performed by finite element method. A 3D mathematical model of thermal processes in titanium in welding with

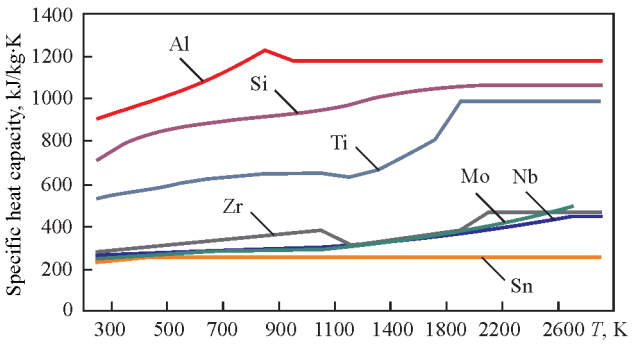

Figure 1. Heat capacity of alloying elements of high-temperature titanium alloy Ti–6.5Al–5.3Zr–2.2Sn–0.6Mo–0.5Nb–0.75Si

a moving heat source was constructed. To perform nonstationary thermal analysis with phase transition, it is necessary to determine the enthalpy dependence on temperature for high-temperature alloy Ti–6.5Al–5.3Zr–2.2Sn–0.6Mo–0.5Nb–0.75Si [5, 6]. Among the numerous empirical relationships of solids, proposed for calculation of heat capacities, the most widespread is the Neumann–Kopp rule, also known as the rule of heat capacity additivity [7]. It allows approximate calculation of chemical compound heat capacity. In keeping with this rule, the molar heat capacity of chemical compounds in the solid state is equal to the sum of molar heat capacities of elements included into this compound. A relationship of the following type is used for an approximate evaluation of specific heat capacity of the alloy [7]:

$$C = pC_1 + qC_2 + \ldots, \quad (1),$$

where C is the specific heat capacity of the alloy; p, q are the weight fractions of the alloy components; C_1, C_2 are the specific heat capacities of the alloy components.

Heat capacities of alloying elements are given in the graph (Figure 1). The given formula (1) was used to establish the temperature dependence of enthalpy for the experimental high-temperature titanium alloy Ti–6.5Al–5.3Zr–2.2Sn–0.6Mo–0.5Nb–0.75Si, compared to heat capacity of VT1-00 titanium alloy (Figure 2).

Heat capacity at 0 °C temperature is equal to 0.526 (kJ/kg·K). In the temperature range from 327 up to 1127 K, the heat capacity of alloy Ti–6.5Al–5.3Zr–2.2Sn–0.6Mo–0.5Nb–0.75Si is approximately 5–7 % higher than that of VT1-00 alloy, and in the temperature range from 1527 to 1860 K it is by 7–10 % lower.

During investigations the influence of such TIG process parameters as welding current, arc voltage, speed of anode spot movement on the dimensions and shape of base metal penetration and HAZ, and probable phase composition of the metal of the weld and HAZ was taken into account.

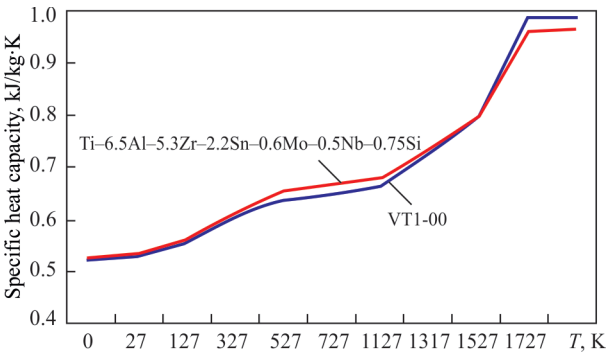

Figure 2. Heat capacity of high-temperature titanium alloy Ti–6.5Al–5.3Zr–2.2Sn–0.6Mo–0.5Nb–0.75Si

Modeling was performed for plates of 200×600×6 mm dimensions. A computational finite element additive grid with sizes shown in Figure 3 was applied to the model constructed by these dimensions.

A 3D mathematical model of thermal processes in titanium during welding was plotted for computational determination of the influence of welding mode parameters on weld formation, taking into account the above assumptions. The model is based on the following differential equation of heat conductivity [9, 10]:

$$\rho c\left(\frac{\delta T}{\delta t}\right) = \frac{d}{dx}\left(\lambda_x \frac{dT}{dx}\right) + \frac{d}{dy}\left(\lambda_y \frac{dT}{dy}\right) + \frac{d}{dz}\left(\lambda_z \frac{dT}{dz}\right), \quad (2)$$

where t is the current time, s; ρ is the material density, kg/m^3; c is the specific heat conductivity, kJ(kg·K); λ is the coefficient of heat conductivity, W/(m·K).

Boundary conditions were formulated, which describe the sample heat exchange with the environment, as well as the welding heat source. In the general case, the following initial and boundary conditions were determined:

1. $T_{t=0} = T_{am}$ is the specified product temperature at the initial moment of time, which is equal to ambient temperature (20 °C).

2. The heat flow on the surface in the zone of impact of the welding heat source is equal to:

$$-\lambda \frac{\partial T}{\partial t} = q_T + q_n + q_s, \quad (3)$$

where q_n is the convective heat exchange, W/(m^2·K):

$$q_T = h_f (T - T_{am}), \quad (4)$$

where h_f is the coefficient of convective heat transfer; in this model it is believed to be constant and equal to 70 W/(m^2·K), T_{am} is the ambient temperature; T is

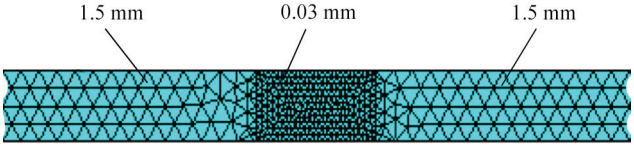

Figure 3. Finite element adaptive grid used for computations

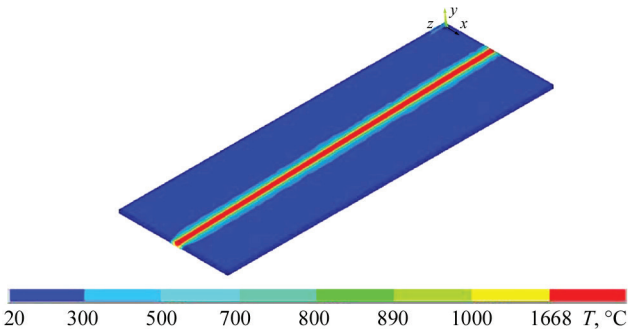

Figure 4. Distribution of maximal temperatures in the welded joint after argon-arc welding simulation

the model surface temperature; q_n is the radiation heat transfer, W/(m²·K):

$$q_n = \varepsilon\sigma\left(T^4 - T_{am}^4\right), \quad (5)$$

where ε is the radiation coefficient, equal to 0.3; σ is the Stephan–Boltzmann constant (σ = 5.6704·10⁻⁸ W/(m⁻²·K⁻⁴); q_s is the distribution of the heat flux from the heat source, W/(m⁻²·K):

$$q_s = q_m \exp\left\{-\frac{(x-Vt)^2 + y^2}{R^2}\right\}, \quad (6)$$

where q_m is the largest heat flow in the heating center, W/(m²·K), V is the welding speed, m/s, R is the radius of the heating spot, m.

Thermal field calculation was performed for 3 welding modes (Table 2). Mode 1 envisages producing a welded joint with incomplete penetration and without preheating, mode 2 is the same, as mode 1, but with preheating to produce complete penetration; mode 3 ensures the same penetration depth, as in mode 1, but with lower energy input and preheating (Mode 3).

INVESTIGATION RESULTS

Thermal fields in the welded product were calculated taking into account the abovementioned initial and boundary conditions. Calculation results were the base to plot the isotherms of maximal temperatures, which were used to determine the geometry and dimensions of the penetration zone, HAZ, and polymorphous transformation zone. Figure 4 shows the result

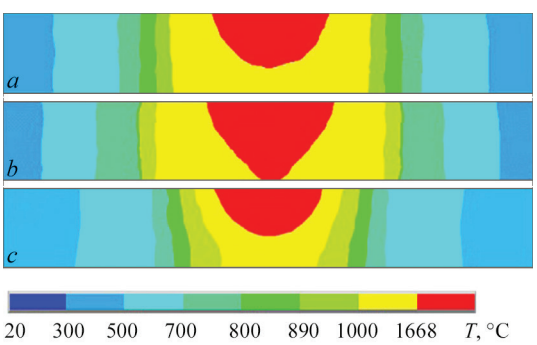

Figure 5. Shape and dimensions of penetration zone (weld metal) and HAZ: *a* — mode 1; *b* — mode 2; *c* — mode 3

Table 2. Modes of argon-arc welding of high-temperature titanium alloy Ti–6.5Al–5.3Zr–2.2Sn–0.6Mo–0.5Nb–0.75Si

Mode No.	Welding current, A	Arc voltage, V	Welding speed, m/h	Preheating, °C
1	310	12	8	–
2	310	12	8	400
3	190	12	8	400

of thermal field calculation in the welded joint in the 3D format.

Such welding modes were selected, at which complete and incomplete penetration of the weld metal can be achieved. This was done in order to determine the influence of preheating on the shape and dimensions of the metal of the weld and HAZ. No complete penetration was achieved in mode 1 (Figure 5, *a*). Penetration depth is 4.2 mm, deposited bead width — 9.2 mm, area — 28.5 mm², HAZ width is equal to 13 mm, area — 73 mm². The same depth, width and area were produced in mode 3 (Figure 5, *c*).

In mode 2 (Figure 5, *b*) the penetration zone width is equal to 10. 8 mm (by 17 % larger than in mode 1), area is 56 mm² (by 96 % larger than in mode 1). HAZ width in this mode is equal to 18.05 mm, and area is 107 mm².

Comparison of calculation results with experimental data confirmed the adequacy of the developed mathematical model (Figure 6). The difference in the penetration zone width in the calculated and experimental sample was 4 %, and for the reverse bead width it was 3 %.

Graphs of the welding thermal cycle for all the modes were plotted in four points: point 1 – on the surface in the weld middle, point 2 — in the weld middle at 3 mm distance from the surface; point 3 — on the HAZ surface at 14 mm distance from the weld middle, point 4 — in the HAZ at 3 mm distance from the surface and 14 mm distance from the weld middle.

One can see from the plotted graphs that in the weld metal the fastest to cool is the metal in mode 1. Preheating application allowed lowering the cooling rates of the samples (Figure 7).

Experimental thermal cycles of TIG welding were obtained to confirm the calculations. TIG welding of high-temperature titanium alloy Ti–6.5Al–5.3Zr–2.2

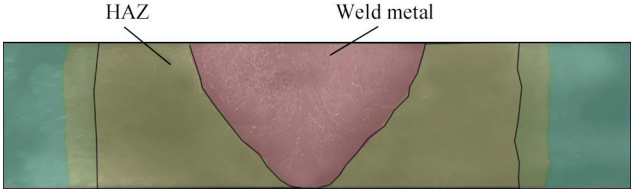

Figure 6. Verification of model adequacy using a macrosection of the welded joint of high-temperature titanium alloy Ti–6.5Al–5.3Zr–2.2Sn–0.6Mo–0.5Nb–0.75Si made in mode 2

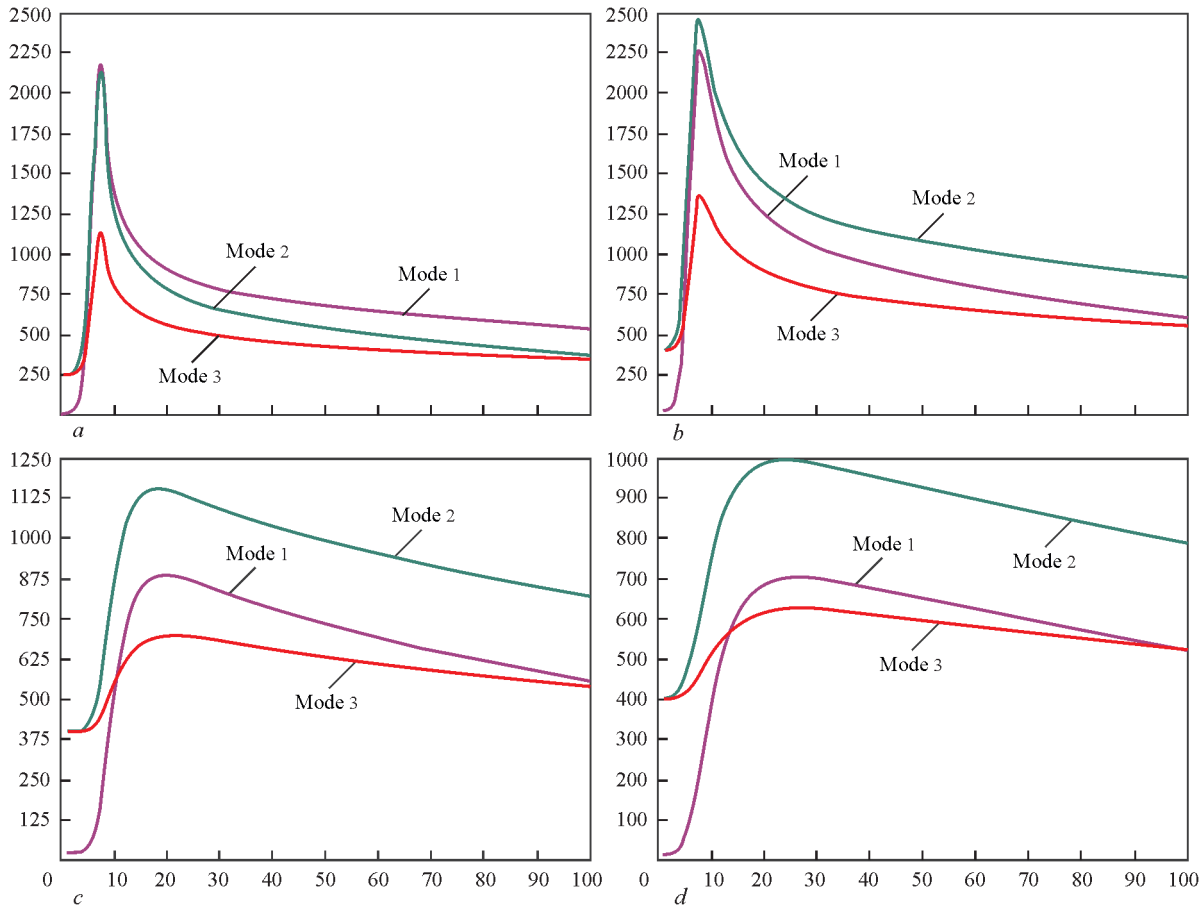

Figure 7. Welding thermal cycles produced by mathematical modeling: *a* — on the surface in the weld center; *b* — in the sample middle in the weld center; *c* — in the specimen middle in the HAZ

Sn–0.6Mo–0.5Nb–0.75Si was performed in OB1826 unit at straight polarity direct current using VDU 511 power source. Specimens were preheated in an electric furnace fitted with heating of shielding gas — argon to protect the welded joint reverse side. Application of an electric furnace with shielding gas heating allowed preheating the samples of high-temperature titanium alloy Ti–6.5Al–5.3Zr–2.2Sn–0.6Mo–0.5Nb –0.75Si up to temperatures of 400 °C.

Welding was performed in modes 1 and 2 (see Table 2), sheet thickness was 6 mm, sample length was 180 mm, and their width was 100 mm. In mode 2 complete penetration of the welded joint of experimental high-temperature titanium alloy Ti–6.5Al–5.3Zr–2.2Sn–0.6Mo–0.5Nb–0.75Si was produced. Experimental thermal cycles were derived using thermocouples of chromel-alumel composition, which were located in point 3 – on the HAZ surface, at 14 mm distance from the weld middle. The derived experimental thermal cycles together with the calculated thermal cycles determined by modeling, are given in Figure 8. As one can see from the Figure, the difference between the experimental and calculated data is equal to 2–5 %.

The diagrams of cooling rate distribution in the temperature range of 600–1200 °C in the welded joint cross-section were plotted as a result of the work performed. It was found that at cooling from 1200 to 1100 °C temperature the cooling rates on the surface in the middle of the weld are higher than 130 °C/s, those in the weld metal lower part and on the boundaries of the weld and the HAZ are equal to 70–130 °C/s, in the rest of the HAZ the metal is cooled at the rate not lower than 31 °C/s (Figure 9, *a*). In the case of application of preheating at 400 °C temperature, at cooling from the temperature of 1200 to 1100 °C the cooling rates on the weld center surface also exceed 130 °C/s, in the weld metal lower part and on the boundaries of

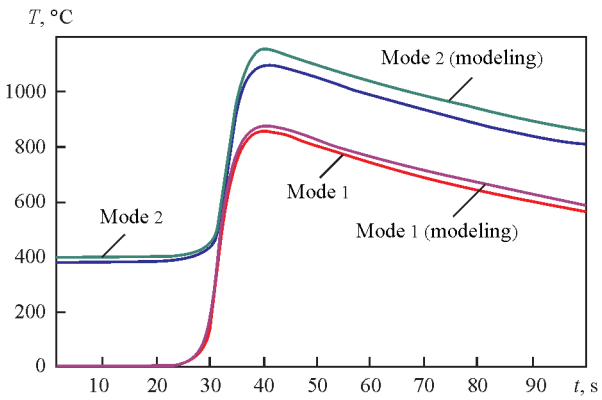

Figure 8. Comparison of experimental and calculated welding thermal cycles

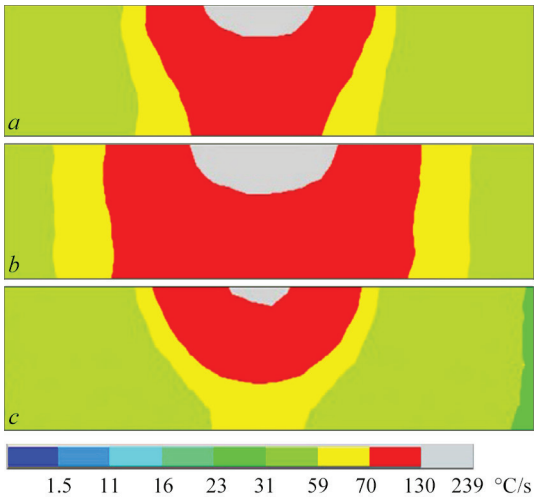

Figure 9. Distribution of cooling rates in the temperature range of 1200–1100 °C: *a* — mode 1; *b* — mode 2; *c* — mode 3

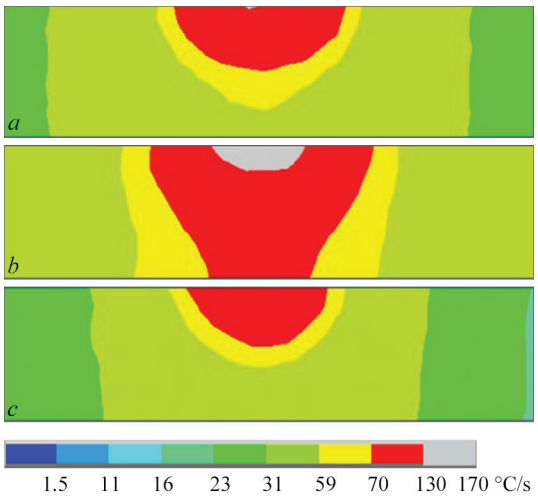

Figure 10. Distribution of cooling rates in the temperature range of 1000–900 °C: *a* — mode 1; *b* — mode 2; *c* — mode 3

the weld and HAZ they are equal to 70–130 °C/s, in the rest of the HAZ the metal is cooled at the rate not lower than 31 °C/s (Figure 9, *b*). Compared to mode 1, in mode 2 the zone with cooling rates higher than 70 °C /s becomes wider.

The mode with lower energy input (Figure 9, *c*) allows reducing the cooling rates by 30–32 % relative to mode 2 and by 35–60 % relative to mode 1 in the entire temperature range.

A similar pattern is observed also in the temperature range of 1000–900 °C (Figure 10, *a*), except that the zone of maximal cooling rates (more than 130 °C/s) is somewhat smaller, but in this zone higher maximal cooling rates are recorded. At application of preheating (mode 2), maximal cooling rates are recorded in the same temperature range in the weld center on the surface and they are equal to 130 °C/s. In the HAZ these values are 59–70 °C/s (Figure 10, *b*). In mode 3 the cooling rates higher than 130 °C/s are not recorded at all in the weld metal (Figure 10, *c*).

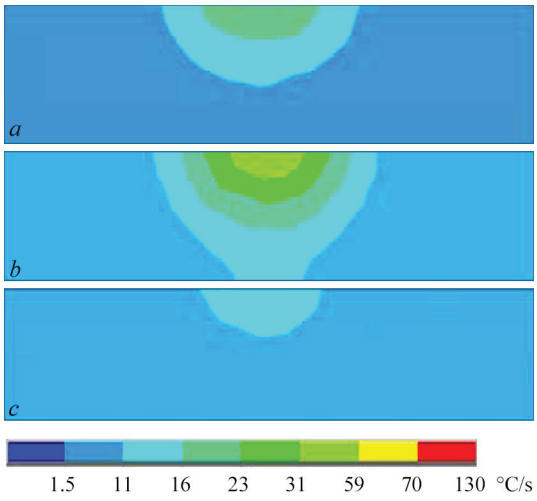

Figure 11. Distribution of cooling rates in the temperature range of 700–600 °C: *a* — mode 1; *b* — mode 2; *c* — mode 3

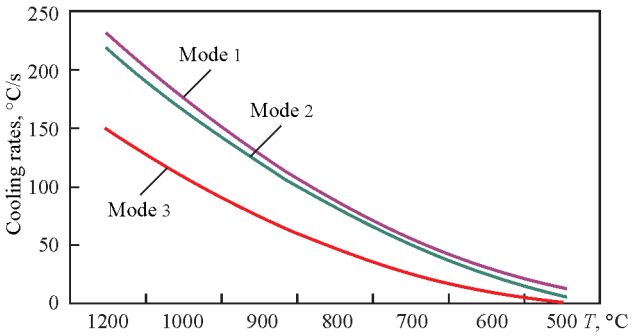

Figure 12. Comparison of cooling rate values

At cooling from the temperature of 700 °C and lower, the cooling rates still remain at a sufficiently high level (120 °C/s in the weld center, 31–70 °C/s in the HAZ) (Figure 11, *a*). Here, the maximal cooling rates in mode 1 have higher values, than in mode 2 with preheating. At cooling from the temperature of 700 °C in mode 2 (Figure 11, *b*), the total range of cooling rates grows noticeably, being equal to 1.5–31 °C/s, compared to the mode without preheating. Mode 3 with smaller energy input and with preheating allows lowering the cooling rates by 35–60 % relative to mode 1 and ensures sample penetration depth of 4.15 mm. Such a penetration depth is achieved in welding in mode 1.

A comparative graph of the dependence of maximal cooling rates on temperatures in the range from 1200 to 500 °C was plotted for points on the surface in the middle of the weld, where the maximal cooling rates are recorded respectively. It was found that in welding 6 mm samples of high-temperature alloy Ti–6.5Al–5.3Zr–2.2Sn–0.6Mo–0.5Nb–0.75Si in mode 2 (with preheating up to 400 °C) the cooling rates are lower than those in mode 1 (without preheating) — by 7–12 % (Figure 12).

CONCLUSIONS

A mathematical model of TIG welding of high-temperature titanium alloy of Ti–6.5Al–5.3Zr–2.2Sn–0.6Mo–0.5Nb–0.75Si system was developed allowing for preheating of the welded joint to 400 °C temperature.

It was found that the heat capacity of experimental high-temperature titanium alloy of Ti–6.5Al–5.3Zr–2.2Sn–0.6Mo–0.5Nb–0.75Si system in the temperature range from 327 to 1127 K, is by 5–7 % higher than that of VT1-00 alloy, and in the temperature range from 1527 to 1860 K it is by 7–10 % lower.

It is shown that application of preheating to the temperature of 400 °C allows increasing the penetration depth of welded joints of high-temperature alloy Ti–6.5Al–5.3Zr–2.2Sn–0.6Mo–0.5Nb–0.75Si by 30 %, the weld width increasing by 17 %.

The plotted distribution of welded joint cooling rates in the temperature range of 500–1200 °C led to the conclusion that the cooling rates in welding with preheating to 400 °C are lower than those in welding without preheating — by 7–12 %, respectively.

References

1. Taranova, T.G., Tunik, A.Yu., Akhonin, S.V. et al. (2012) Peculiarities of structure of Ti–Si–X titanium alloy joints with dispersion hardening performed by electron beam welding. *Visnyk NUK,* **5**, 125–130 [in Ukrainian].
2. Anca, A., Cardona, A., Risso, J., Fachinotti, V.D. (2011) Finite element modeling of welding processes. *Applied Mathematical Modelling*, 35(**2**), 688–707.
3. Akhonin, S.V., Berezos, V.O., Pikulin, O.M. et al. (2022) Producing high-temperature titanium alloys of Ti–Al–Zr–Si–Mo–Nb–Sn system by electron beam melting. *Suchasna Elektrometal.*, **2**, 3–9 [in Ukrainian]. DOI: https://doi.org/10.37434/sem2022.02.01
4. Akhonin, S.V., Severin, A.Yu., Pikulin, O.M. et al. (2022) Structure and mechanical properties of high-temperature titanium alloy of Ti–Al–Zr–Si–Mo–Nb–Sn system after deformation treatment. *Suchasna Elektrometal.*, **4**, 43–48 [in Ukrainian]. DOI: https://doi.org/10.37434/sem2022.04.07
5. Akhonin, S.V., Bilous, V.Yu., Selin, R.V. et al. (2022) Argon-arc welding of high-temperature titanium alloy doped by silicon. *The Paton Welding J.*, **5**, 26–32. DOI: https://doi.org/10.37434/tpwj2022.05.04
6. Akhonin, S.V., Belous, V.Yu., Selin, R.V. (2021) Effect of pre-heating and post-weld local heat treatment on the microstructure and mechanical properties of low-cost β-titanium alloy welding joints, obtained by EBW. *Defect and Diffusion Forum*, **416**, 87–92.
7. Bros, H., Michel, M., Castanet, R. (1994) Enthalpy and heat capacity of titanium based alloys. *J. of Thermal Analysis and Calorimetry*, 41(**1**), 7–24.
8. Maglić, K.D., Pavičić, D.Z. (2001) Thermal and electrical properties of titanium between 300 and 1900 K. *Inter. J. of Thermophysics*, **22**, 1833–1841.
9. Akhonin, S.V., Belous, V.Y., Selin, R.V., Kostin, V.A. (2021) Influence of TIG welding thermal cycle on temperature distribution and phase transformation in low-cost titanium alloy. In: *Proc. of IOP Conf. Series: Earth and Environmental Sci*., 688(**1**), 012012.
10. Akhonin, S.V., Belous, V.Yu., Muzhichenko, A.F., Selin, R.V. (2013) Mathematical modeling of structural transformations in HAZ of titanium alloy VT23 during TIG welding. *The Paton Welding J.*, **3**, 24–27.

ORCID

R.V. Selin: 0000-0002-2990-1131,
V.Yu. Bilous: 0000-0002-0082-8030,
I.B. Selina: 0000-0002-4010-3819

CONFLICT OF INTEREST

The Authors declare no conflict of interest

CORRESPONDING AUTHOR

R.V. Selin
E.O. Paton Electric Welding Institute of the NASU
11 Kazymyr Malevych Str., 03150, Kyiv, Ukraine.
E-mail: selinrv@gmail.com

SUGGESTED CITATION

R.V. Selin, V.Yu. Bilous, S.B. Rukhanskyi, I.B. Selina, L.M. Radchenko (2024) Influence of preheating on TIG welding thermal cycle of high-temperature titanium alloy of Ti–Al–Zr–Sn–Mo–Nb–Si system. *The Paton Welding J.*, **2**, 8–13.

JOURNAL HOME PAGE

https://patonpublishinghouse.com/eng/journals/tpwj

Received: 13.03.2023
Received in revised form: 28.11.2023
Accepted: 29.01.2024

DOI: https://doi.org/10.37434/tpwj2024.02.03

STRENGTH AND STRUCTURE OF MA2-1M MAGNESIUM ALLOY BUTT JOINTS PRODUCED BY ARGON-ARC WELDING WITH A NONCONSUMABLE ELECTRODE AND BY FRICTION STIR WELDING

A.G. Poklyatskyi[1], V.E. Fedorchuk[1], S.I. Motrunich[1], Yu.V. Falchenko[1], M. Sahul[2]

[1]E.O. Paton Electric Welding Institute of the NASU
11 Kazymyr Malevych Str., 03150, Kyiv, Ukraine
[2]Czech Technical University
166 36, Prague, Czech Republic

ABSTRACT

The paper analyzes the results of research of structural features and tensile strength of butt joints of 2 mm thick sheets of structural MA2-1M magnesium alloy produced by nonconsumable electrode argon-arc welding and by friction stir welding. It is shown that in friction stir welding as a result of intensive plastic deformation of the metal, a fine crystalline structure is formed in the welds. It was determined that microhardness of the metal in such a welded joint has minimal values in the zone of thermomechanical impact on the retreating side near the heat-affected zone, where fracture of the specimens occurs during their static tension. Tensile strength of specimens of welded joints produced by friction stir welding, and specimens with root penetration removed to the level of the base material and additionally scraped reinforcement of welds produced by fusion welding, is at the level of 233–236 MPa, which amounts to ~84 % of this value for base material.

KEYWORDS: magnesium alloy, friction stir welding, argon-arc welding, structure, microhardness, strength

INTRODUCTION

Magnesium alloys are widely used as structural materials to manufacture lightweight strong components of aerospace and automotive equipment, as well as moving elements of textile and printing equipment, which allows reducing the force of inertia at high speeds of their movement [1–3]. The effectiveness of such alloy application is due to a low specific weight of magnesium (1.74 g/cm^3), high strength of its alloys (228–290 MPa) and their considerable heat resistance (up to 450 °C) [4].

The majority of magnesium alloys are successfully welded by fusion welding methods. Similar to aluminium alloys, nonconsumable (tungsten) electrode argon-arc welding (GTAW) is most often used. Welded joints of magnesium alloys produced by fusion processes are characterized by the same defects in the form of pores, macroinclusions of oxide films and hot cracks, which arise in aluminium alloy welding [5, 6]. Therefore, friction stir welding (FSW) is a promising method for producing sound permanent joints of magnesium alloys [7]. The abovementioned defects can be avoided due to weld formation in the solid phase, without melting of the edges being welded. Moreover, FSW does not require filler wire (manufacture of which is complicated by high brittleness of magnesium alloys) or shielding inert gas, which increases material cost savings [8].

Experimental investigations conducted by foreign specialists are indicative of the efficiency of application of this welding method for magnesium alloys. The produced joints have fine-crystalline structure of the welds and high mechanical properties [9, 10].

The objective of this work is investigation of structural features and determination of mechanical properties of welded joints on 2 mm sheets of structural MA2-1M magnesium alloy, produced by GTAW and friction stir welding.

INVESTIGATION PROCEDURE

Mechanical properties of welded joints were assessed using 2 mm sheets of serial MA-21M magnesium alloy of Mg–Al–Zn–Mn alloying system, which in addition to magnesium contains, wt.%: 4.5 Al, 0.95 Zn, 0.47 Mn, 0.3 Fe, 0.06 Si, 0.01 Cu. Mechanical properties of such sheets are given in the Table 1.

The process of mechanized GTA welding was conducted in ASTV-2M unit with MW-450 power source (Fronius, Austria). Square-wave current of 200 Hz frequency was used [11] for intensive stirring of weld pool molten metal, creating favourable conditions for its degassing and reducing the probability of pore formation in the welds. The nonconsumable electrode diameter was 3.2 mm, and the length of its extension

was 4 mm. The torch movement speed of 20 m/h was selected, considering on the one hand the wish to ensure the minimal thermal impact on the metal being welded, and on the other hand, the possibility for the welding operator to adjust the electrode orientation relative to the butt axis or the arc length, if required. To obtain chemical composition of the weld metal close to that of the base material, a strip from base material 2 mm thick was used as the filler material to form the weld reinforcement. The strip was fixed between the edges being welded, lowering it to the bottom of 1 mm deep and 4 mm wide groove. The height of this strip was 6–7 mm, which ensured formation of the required weld reinforcement. The possible defects characteristic for this welding process, which have the form of pores and macroinclusions of oxide films, mostly arising in the weld root part, come to the root penetration, which is scraped flush with the base metal in critical structures. Mechanical cleaning of the edges to be welded (from three sides) and of filler material strip (from four sides) to the depth of 0.10–0.12 mm was performed immediately before welding. To ensure a reliable protection of the metal from oxidation, high grade argon was used in the welding zone. The inner diameter of the protective ceramic nozzle was 16 mm, and gas flow rate was 20–22 l/min. Sound weld formation under such conditions was ensured at the current of 145–150 A. Current reduction led to incomplete fusion of the filler material strip placed into the butt with the base material, and current increase resulted in violation of weld formation.

FSW of the studied alloy sheets was performed in a laboratory unit developed at PWI. It ensures the speed of the tool linear movement along the butt (welding speed) in the range of 8–38 m/h, and constant frequency of its rotation of 1420 rpm. A special tool of our design [12] with shoulder diameter of 12 mm and 1.85 mm long pin in the form of a truncated cone of 3.4 mm diameter at the shoulder base was used for welding. Butt joints of the sheets were produced at three welding speeds of 8, 16 and 24 m/h for evaluation of their properties. At higher welding speeds the probability of internal defect occurrence in the welds in the form of cavities characteristic for this process, becomes higher [13]. More over, in the laboratory unit tool pressing to the surfaces of the edges being welded is performed by the welding operator using a support, which makes the uniformity of its regulation more complicated at higher welding speeds. Mechanical cleaning of the edges to be welded (from three sides) to the depth of 0.10–0.12 mm was performed directly before welding to prevent penetration of possible surface contamination or oxide films into the weld formation zone.

Table 1. Mechanical properties of 2 mm sheets of structural MA2-1M magnesium alloy

Characteristic	Specimens cut out along the sheet rolling direction	Specimens cut out across the sheet rolling direction
σ_t, MPa	279–274 277	283–279 281
$\sigma_{0.2}$, MPa	200–179 187	219–203 210
δ_5, %	20.3–19.5 19.9	26.3–23.5 25.0
α, deg	38–32 35	45–38 42

Note. The numerator shows the maximal and minimal values, and the denominator gives their average values by the results of testing three specimens.

The produced welded joints were used to make sections for studying the structural features of the welds and for assessing the degree of metal softening in the welding zone. Metal microhardness was measured on the section end faces by PMT-3 microhardness meter. Assessment of structural features of the welded joints was performed using MMT-1600B optical microscope. Determination of tensile strength at uniaxial tension of specimens with working part width of 15 mm was conducted in keeping with DSTU EN ISO 4236x in an all-purpose servohydraulic complex MTS 318.25. GTA welded samples were tested with both excess penetration cut off flush with the base material, and with the additionally scraped weld reinforcement.

RESULTS AND DISCUSSION

Analysis of the microstructure of FSW joint showed that it consists of welding zones classical for such a welding method: base material, thermomechanical impact zone, HAZ and weld metal with the formed nugget (Figure 1). Weld metal grains are 3–5 times finer than those in the metal being welded. The most fine-grained structure is observed in the weld metal nugget. Measurements of metal microhardness in the transverse sections in different zones of FS welded joint showed that its values are minimal in the thermomechanical impact zone from the retreating side near (2.5–3.0 mm) the HAZ (Figure 2). Accordingly, at static tension of specimens of such welded joints, they failed in the thermomechanical impact zone from the retreating side (Figure 3). On the face side fracture occurred exactly at the distance of 2.5–3.0 mm from the boundary of this zone with the HAZ, and from the root side it ran in the zone of the weld transition

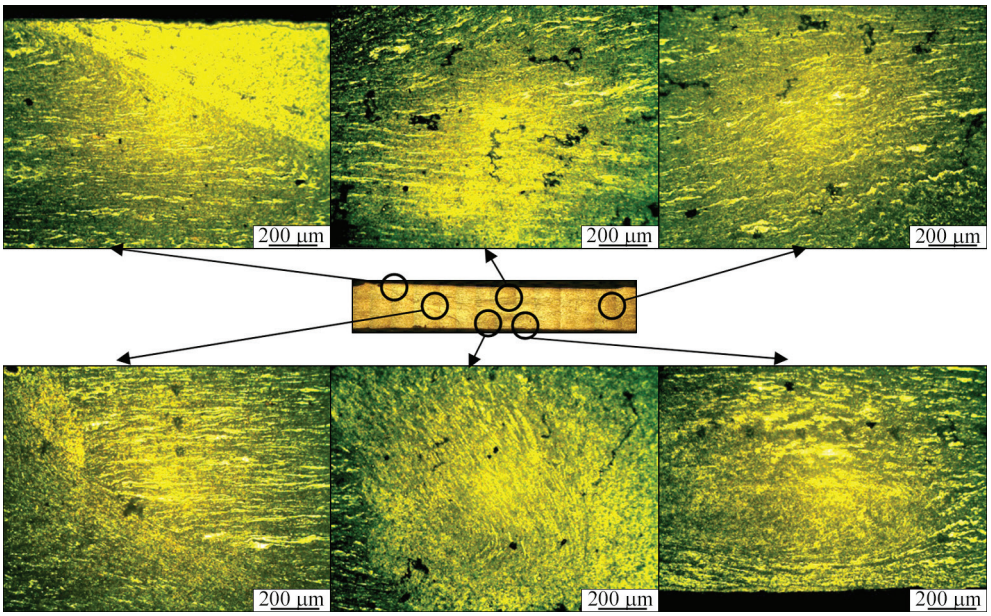

Figure 1. Fragments of the microstructure of FSW butt joint of structural MA2-1M magnesium alloy

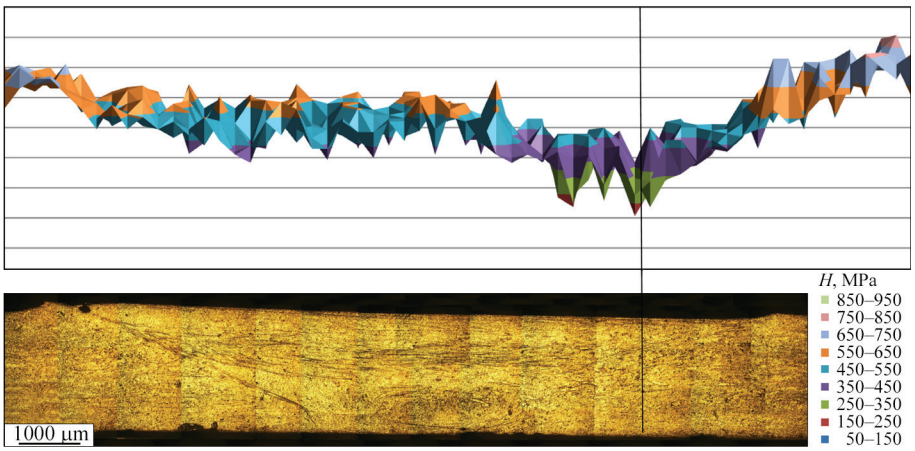

Figure 2. Metal microhardness in different zones of FS welded joint of 2 mm MA2-1M alloy produced at welding speed of 14 m/h

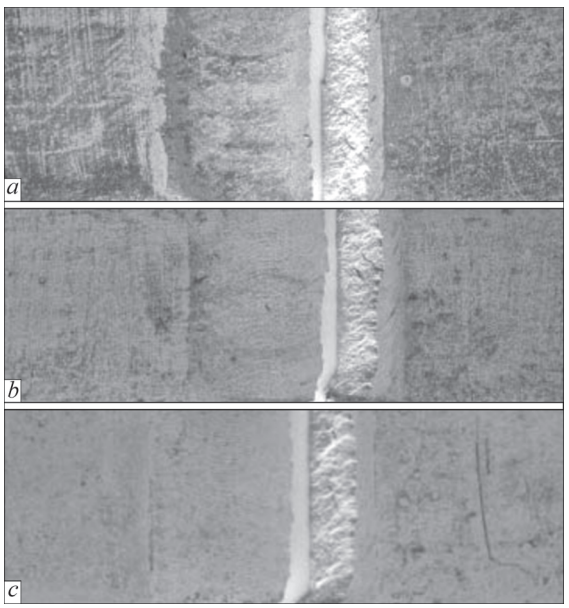

Figure 3. Appearance of the face surface of working part of 2 mm MA2-1M magnesium alloy specimens fractured as a result of static tension, which were produced by FSW at welding speeds of 8 (*a*), 16 (*b*) and 24 m/h (*c*)

to base material. The tensile strength of FS welded specimens is at the level of 234–236 MPa, and it is independent on the welding speed in the studied range.

Microstructural studies of GTAW butt joints of structural MA2-1M magnesium alloy showed that the weld metal has a dendritic structure (Figure 4). Columnar dendrites directed away from the fusion line into the weld metal are observed in it near the line of weld fusion with the base material. Recrystallization of base metal grains occurred in the HAZ. Directly next to the fusion line the grains are partially melted.

Specimens of GTA welded joints with weld reinforcement have the tensile strength of 267 MPa, which is equal to 96 % of this value for base metal. Their fail from the weld face side in the zone of weld fusion with the base material, and from the root side — in the base metal in the HAZ at approximately 5 mm distance from the line of weld fusion with the base material (Figure 5). Specimens with root penetration cut off flush with the base material and with addition-

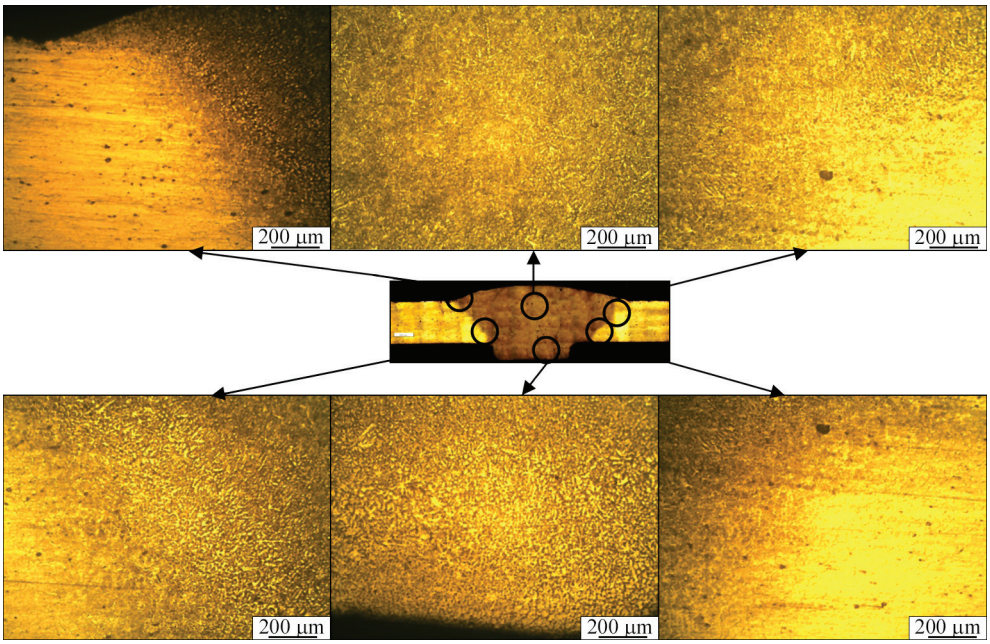

Figure 4. Fragments of the microstructure of GTA welded butt joint of 2 mm structural MA2-1M magnesium alloy

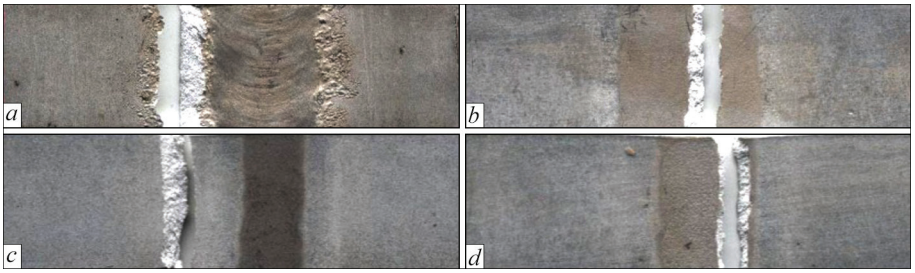

Figure 5. Appearance of the face (*a*, *c*) and root (*b*, *c*) surfaces of the working part of GTA welded specimens of 2 mm MA2-1M magnesium alloy with weld reinforcement (*a*, *b*) and without it (*c*, *d*)

ally scraped weld reinforcement failed at static tension in the weld metal and their ultimate strength was at the level of 233 MPa, which is confirmed by minimal hardness in the weld central part (Figure 6). Accordingly, specimen fracture from the weld face side occurred near its central part, and from the root side it ran in the zone of weld fusion with base material.

CONCLUSIONS

1. Microhardness of FS welded joint is minimal in the zone of thermomechanical impact from the retreating side near (2.5–3.0 mm) the HAZ, which is exactly the region where such specimens fail at their static tension.

2. The structure of GTA weld metal is dendritic. Columnar dendrites directed away from the fusion line into the weld metal are found in it near the zone of weld fusion with base material. Minimal hardness is observed in the weld center. In friction stir welding of this alloy intensive plastic deformation of the metal in the weld central part (nugget) results in formation of grains 5 times finer than the base metal structure. In the thermomechanical impact zone a complete reorientation of the grains in the direction of movement of the tool working surfaces

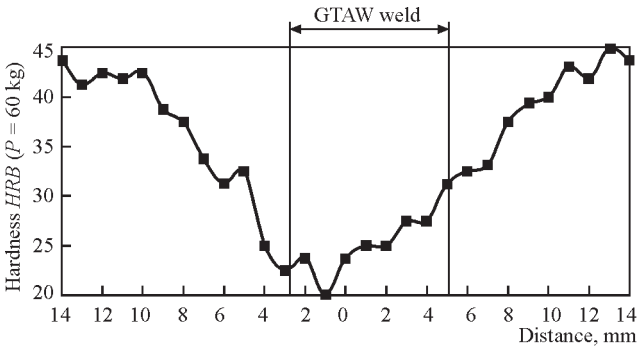

Figure 6. Hardness of metal of GTA welded joint of 2 mm MA2-1M alloy

takes place. It results in formation of extended elongated grains oriented along this trajectory.

3. GTA welded specimens with weld reinforcement have the maximal tensile strength (267 MPa), which is equal to 96 % of this value for base material. Tensile strength of FS welded joints, as that of specimens with root penetration cut off flush with base material and with additionally scraped weld reinforcement of welds made by the fusion process, is at the level of 233–236 MPa.

REFERENCES

1. Zuemer, N. (1998) Magnesium alloys in new aeronautic equipment. In: *Proc. of the Conf. on Magnesium Alloys and their Applications*, Wolfsburg, Germany, 125–132.
2. Luo, A.A. (2002) Magnesium: Current and potential automotive applications. *JOM*, February, 42–48.
3. Shapiro, A.E. (2005) Brazing magnesium alloys and magnesium matrix composites. *Welding J.*, **10**, 33–43.
4. Avedesian, M.M., Baker, H. (1999) *Magnesium and magnesium alloys, metals*: Handbook. Materials Park. Ohio, ASM Int.
5. Sachin, K., Chuansong, W. (2017) Review: Mg and its a loy — scope, future perspectives and recent advancements in welding and processing. *J. of Harbin Institute of Technology (New Series)*, 24(**6**), 1–37. Doi: 10.11916/j.issn.1005-9113.17065.
6. Hongjie, L., Jis, M., Wencai, L. et al. (2022) Influence of TIG welding process parameters on microstructure and mechanical properties of as-cast Mg–8Li–3Al–2Zn–0.5Y alloy. *J. of Materials Research and Technology*, **20**, 4114–4129. DOI: https://doi.org/10.1016/j.jmrt.2022.08.157
7. Thomas, W.M., Nicholas, E.D., Needham, J.C. et al. (1991) *Friction stir butt welding*. Int. Pat. Appl. No. PCT/GB 92/02203; GB Patent Applications No. 9125978.8.
8. Defalco, J. (2006) Friction stir welding vs. fusion welding. *Welding J.*, **3**, 42–44.
9. Lee, W.B., Leon Y.M., Jung, S.B. (2003) Joint properties of friction stir welded AZ31B–H24 magnesium alloy. *Mater. Sci. and Technol.*, **6**, 785–790.
10. Aritoshi, M. (2005) Friction stir welding of magnesium alloys sheets. *J. of the Japan Welding Society*, **3**, 18–23.
11. Poklyatsky, A.G., Grinyuk, A.A. (2001) Effect of parameters of asymmetric and modulated currents on quality of aluminium alloy welded joints. *The Paton Welding J.*, **7**, 33–36.
12. Ishchenko, A.Ya., Poklyatskyi, A.G. (2020) *Tool for friction stir welding of aluminium alloys*. Pat. 54096 Ukraine, Int. Cl. B23K 20/12; PWI, No. u201005315, Fill. 30.04.2010, Publ. 25.10.2010 [in Ukrainian).
13. Poklyatskii, A.G. (2019) Prediction of parameters of friction stir welding of sheet aluminium alloys. *The Paton Welding J.*, **8**, 37–42. DOI: https://doi.org/10.15407/tpwj2019.08.06

ORCID

V.E. Fedorchuk: 0000-0002-9929-3231,
S.I. Motrunich: 0000-0002-8841-8609,
Yu.V. Falchenko: 0000-0002-3028-2964

CONFLICT OF INTEREST

The Authors declare no conflict of interest

CORRESPONDING AUTHOR

A.G. Poklyatskyi
E.O. Paton Electric Welding Institute of the NASU
11 Kazymyr Malevych Str., 03150, Kyiv, Ukraine.
E-mail: pag556a@gmail.com

SUGGESTED CITATION

A.G. Poklyatskyi, V.E. Fedorchuk, S.I. Motrunich, Yu.V. Falchenko, M. Sahul (2024) Strength and structure of MA2-1M magnesium alloy butt joints produced by argon-arc welding with a non-consumable electrode and by friction stir welding. *The Paton Welding J.*, **2**, 14–18.

JOURNAL HOME PAGE

https://patonpublishinghouse.com/eng/journals/tpwj

Received: 22.09.2023
Received in revised form: 27.11.2023
Accepted: 29.01.2024

DOI: https://doi.org/10.37434/tpwj2024.02.04

ELECTRON BEAM WELDING OF SHEET INTERMETALLIC ALLOY WITH A CONTROLLED COOLING RATE

E.L. Vrzhyzhevskyi, N.V. Piskun, O.A. Velykoivanenko, I.I. Statkevych, T.G. Taranova

E.O. Paton Electric Welding Institute of the NASU
11 Kazymyr Malevych Str., 03150, Kyiv, Ukraine

ABSTRACT

The objective of this study is development and testing of elements of the technological process of electron beam welding (EBW) of intermetallic alloys of TiAl system, which allows performance of welding, preheating and subsequent local heat treatment of welded joints in one pass in one chamber, that enables preventing defects of the type of cold cracks, due to a controlled cooling rate. The work explains why EBW is exactly the most suitable process for welding titanium-based intermetallic alloys. A welding method is proposed and described in detail, which is performed in the gravity position at cantilever fastening of the samples in a special device, while heat treatment is conducted immediately after completion of the welding process, ensuring an optimal cooling rate of the welded joint. It is found that cold cracking in the intermetallic welded joints is related to a low ductility of as-welded material. A mathematical model was developed for numerical prediction of the temperature field kinetics and stressed state calculation. The model was used as a basis to conduct a computational experiment and to determine the thermal conditions leading to cracking in EBW process. It is shown that the highest level of residual stresses is formed directly after completion of the welding process; it is equal to 350 MPa and is observed in the weld center. In order to prevent cold cracks in welded joints of titanium aluminide samples, a technological measure was proposed, which combines EBW of Ti–44Al–5Nb–3Cr–1.5Zr (at.%) intermetallic with preheating and postweld local heat treatment (LHT). It was numerically shown and experimentally confirmed that application of a distributed source of sample preheating before welding allows creating favorable conditions during welding and at further cooling, namely lowering the tensile stresses. The way the process is implemented and its influence on the stressed state and structure of the produced joints are described in detail. The work gives the modes of EBW of sheet intermetallic alloy with a controlled cooling rate and results of structural and mechanical studies of the welded joints, produced by the proposed technology.

KEYWORDS: electron beam welding, TiAl system intermetallics, sheet plates, controlled cooling rate, stressed state, "gravity" welding, local heat treatment

INTRODUCTION. RELEVANCE

Literature review showed that the intermetallic alloys of TiAl system have been ever wider applied recently in manufacture of parts and components of gas turbine aircraft engines, as well as in other industries.

At this stage of welding technology development the question of sheet metal welding is of considerable importance. Use of thin materials in various structures enables lowering the weight and overall dimensions of welded structures, and, thus, reducing their cost, which is particularly noticeable when using titanium-based intermetallics.

Intermetallic alloys of TiAl system [1] have the most unfavourable characteristics for welding in sheet structures. It is associated with low ductility of this material at normal temperature, as well as with considerable chemical activity.

Intermetallic alloys of TiAl system, having low specific weight, high heat resistance, long-term strength and creep in the temperature range of 750–850 °C are finding application in manufacture of parts and components of gas-turbine aircraft engines, as well as in other industries [2].

As this alloy of TiAl system is a promising material for wide application in structures of aircraft engine turbines, automotive parts and in some other sectors [2], it requires joining methods, which allow welding products of diverse geometrical shapes, making welds of different length, as well as intermittent welds. In our opinion, electron beam welding (EBW) is the most promising method to produce intermetallic joints. Compared to other welding methods, it has the following advantages: first, as it is conducted in high vacuum, it completely ensures protection of any active material, which titanium is; secondly, a very narrow weld and a very small HAZ form at EBW, which, in its turn should lead to minimal deformations of the welded joint [3].

However, a significant drawback of these alloys are cold cracks, arising at welded joint cooling at temperatures below 700 °C, when the material goes from the tough into the brittle state [2].

At increase of welding stresses during cooling a low ductility of the welded joint in as-welded state leads to development of defects of the type of cold cracks. In this connection, in order to produce a sound welded joint and avoid cold cracking, it is necessary to lower the temperature gradient and the welding stresses, respectively, which is ensured by a slowed down cooling rate.

Table 1. Chemical composition of experimental alloy

Alloy	Ti	Al	Nb	Cr	Zr
wt.%	52.82	28.8	11.72	3.51	3.16
at.%	45.92	44.54	5.26	2.82	1.46

Modern methods and technologies of welding sheet metal envisage application of heat sinks, different kinds of forming backing [1], or other equipment, which would prevent thin metal burning-through. Such a process is characterized by rather low welding speeds. This, in its turn, has a negative impact on productivity, material costs for production and, eventually, the product cost.

The authors of work [4] use copper backing. Here, it is important to ensure their tight contact with the edges to be welded along the entire length, as in the places where gaps remain between the backing and the edge, the welding process is accompanied by burn-through and sagging of the weld. In welding sheet materials, it is exactly the concentration of the heating source heat which is important, as it is favourable not only for formation of the weld, but also for the HAZ.

Known is a method of controlling the cooling rate of intermetallic welded joints described in work [5], when the sample is welded on a ceramic plate, which slows down the welded joint cooling rate that influences the magnitude of welding stresses. A disadvantage of this method is that the heat conductivity and the cooling rate of the welded joint, respectively, are determined by thermophysical properties of this ceramic backing, the cooling rate being practically not controlled.

Therefore, development and optimization of the technological process, which enables controlling the electron beam due to distribution of power of the electron beam thermal impact, in order to create the specified temperature field at EBW with simultaneous preheating and further heat treatment of the plate being welded, are highly important.

INVESTIGATION MATERIAL AND PROCEDURE

An intermetallic alloy of the following composition Ti–44Al–5Nb–3Cr–1.5Zr at.%, developed and produced at PWI by the method of cold-hearth electron beam melting (Table 1), was studied in the work [6].

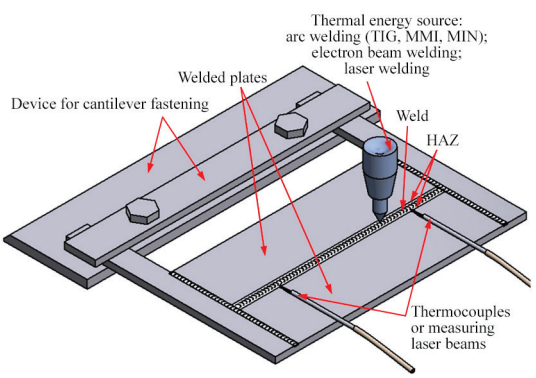

Figure 1. Scheme of performance of EBW process

Electron beam welding of the intermetallic was performed in the welding chamber of UL-144 unit of 2.16 m^3 volume (1200×1200×1500 mm). It has a 60 kW power unit at 60 kV accelerating voltage, and wide adjustment capabilities to implement additional technological processes. The diagram of EBW process is shown in Figure 1.

Manipulator of UL-144 welding chamber was upgraded for welding Ti–44Al–5Nb–3Cr–1.5Zr (at.%) intermetallic. The upgraded sealed lead-in ensures lowering of the resistance at shaft rotation using an oil "wedge". FL 86STH156-620B step motors with software for gun movement are mounted on the manipulator. Such upgrading allows assigning and reproducing the assigned movement trajectories with 0.1 mm accuracy. Moreover, additional equipment was installed, which provides cantilever fastening of the sample to be welded.

Software support of EBW and local heat treatment was performed using industrial computer Advantech 610.

Samples for investigation were prepared after EBW (Figure 1). Plates of 100x30 mm size 3 mm thick from Ti–44Al–5Nb–3Cr–1.5Zr (at.%) alloy were welded. Before welding the plates were ground from all sides and assembled end-to-end without a gap.

To avoid deplanation of the plates during welding the run-on and run-off tabs from VT1-0 titanium alloy were mounted from two sides and welded across the sample. The length of run-off tabs, which were fastened in a special device, was 160 mm. The weld was started and ended on the run-on and run-off tabs.

The ingot microstructure was revealed through etching in a solution of hydrofluoric and nitric acid (1 part of hydrofluoric (HF) and 3 parts of nitric (HNO_3) acid).

Intermetallic hardness was measured by Leco hardness meter at 25 g load.

Fractographic studies were conducted in scanning electron microscope JSM-840 of JEOL, Japan, which is fitted with microanalyzer of Link system 860/500 (Great Britain).

As cracking occurs not only at the cooling stage, but also at the stage of metal heating before the start of the welding process, it is necessary to create a technology, which allows producing defectfree welded joints. Experiments on welding and investigation of welded joints of intermetallic alloy Ti–44Al–5Nb–3Cr–1.5Zr (at.%) were conducted on 3 mm sheet samples. Sample thickness for optimization of the welding modes was selected proceeding from the fact that 3 mm thicknesses can be used for blades of high and low pressure turbines.

EBW was conducted without preheating by the scheme shown in Figure 1 in the following mode:

$$U_{acc} = 60 \text{ kV}; I_b = 35 \text{ mA}; V_w = 7 \text{ mm/s};$$
$$P = 5 \cdot 10^{-3} \text{ Pa}.$$

After welding the weld was cooled to room temperature in the chamber.

In order to ensure a uniform cooling of the material, welding is performed with the sample in unrestrained position (gravity welding) [7]. Welding and heat treatment are conducted with cantilever fastening of the samples in a special device. Heat treatment is performed immediately after completion of the welding process, ensuring a cooling rate of not more than 70 °C/s. Such a method allows determination of the shape of the temperature field in welding of any joints of various metals, a characteristic feature of which is that the temperature fields are determined under the conditions of cantilever fastening without the possibility of heat removal through mechanical contact.

Formation of the weld in "gravity' position is particularly important, as it allows avoiding a considerable number of problems associated exactly with welding sheet materials. Better results are achieved in welding of a butt joint with the sample in unrestrained position without application of forming devices or backing, as here a two-sided exit of gases and metal vapours from the penetration channel is ensured, when gas evolution is facilitated [8].

INVESTIGATION RESULTS

Visual investigation of the welded butt joints showed that transverse cold cracks (Figure 2, *a*) are observed in the weld, which pass through the welded joint and end in the base material on both sides of the sample. As mentioned above, the main source of crack initiation is the low ductility of the material at room temperatures (ductile-brittle transition temperature is 700 °C) and impossibility of resisting crack initiation, as a result of welding stress formation.

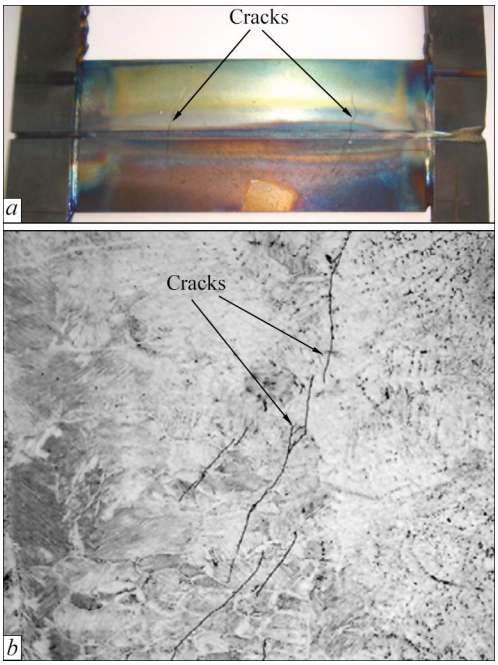

Figure 2. Sample of EB welded joint of intermetallic alloy of Ti–44Al–5Nb–3Cr–1.5Zr, at.% system: *a* — general view; *b* — microstructure (×200) of weld metal [8]

When studying the microstructure of the weld zone, an inhomogeneity of the weld metal structure in the form of $(\gamma+\alpha_2)$-phase colonies is observed. They are located along the fusion zone and have the microhardness of 5110–5270 MPa. Numerous cracks of 100 to 300 μm length, located parallel to the fusion line, were also found in this region (Figure 2, *b*) [9].

Fractographic studies showed that the main crack developed in steps in the weld metal (Figure 3, *a*). A change in the structure from the face to the reverse side of the weld is observed. In the face side region the structure is fine-grained (Figure 3, *a*), and in the metal of the weld reverse side the structure consists of elongated lamellas (Figure 3, *b*). Weld metal fracture is intergranular with small secondary cracks. One can see a γ-phase fragmentation (Figure 3, *b*) due to dispersed α_2-phase precipitates. Sections where no γ-phase fragmentation occurred were also found on the fracture surface.

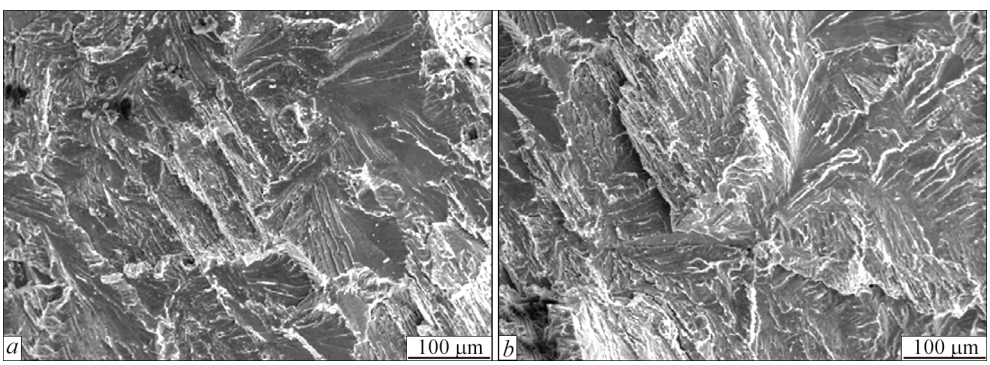

Figure 3. Fractogram of fracture surface of weld of a sample of 3 mm thick Ti–44Al–5Nb–3Cr–1.5Zr, at.% intermetallic alloy: *a* — weld structure (face side), ×200; *b* — fracture area with elongated lamellas on the reverse side, ×200

As shown by experience of previous researchers, residual stresses form in welded joints at EBW, which in combination with the structure lead to cracking in the weld.

Proceeding from the above, further research consisted in development of EBW technology, which will ensure a lowering of the level of residual welding stresses, and will improve weld ductility, which will allow avoiding cold cracking.

INVESTIGATIONS OF THERMAL CONDITIONS, UNDER WHICH DEFECTS FORM IN WELDED JOINTS

A numerical experiment was used to determine the thermal conditions, under which stresses arise in 3 mm samples, leading to cracking [10].

Temperature field kinetics was considered at sample preheating, welding and further cooling to room temperature. The kinetics of the sample stress-strain state (SSS) was predicted proceeding from these numerical results. At initiation of cold cracks, a higher level of tensile welding stresses is the determinant factor.

Given below are the calculated graphs of residual longitudinal stress distribution in the cross-section of the welded joint along the length of a 3 mm plate, which were derived in a computational experiment (Figure 4, *a*). Investigations of the stressed state of the welded joints showed that in as-welded state tensile stresses form in the weld center and in the fusion zone, the level of which changes from 350 to 370 MPa. Longitudinal tensile stresses acting along the weld are nonuniform. This is on average 5 % higher than the transverse stresses in some regions (Figure 4, *b*). With greater distance from the weld center, the level of residual stresses becomes lower and at 7 mm distance from the center (in the base metal) the stresses become smaller at approximately 100 MPa, and then they gradually decrease to 0 and at the plate ends they change from tensile into the compressive ones.

Thus, cold crack initiation in welding occurs both at the cooling and at the heating stage, as a result of high stresses in the area of the weld and the fusion zone, where the tensile stress field is formed.

The nature of distribution of residual longitudinal stresses in the cross-section of a welded joint produced using a computational experiment, is shown in Figure 4, *b*. One can see that residual longitudinal stresses are nonuniformly distributed in the cross-section across the width. Tensile stresses act in the weld and zone adjacent to it and compressive stresses are present in the other part of the cross-section.

The highest level of dangerous residual tensile stresses forms in the center of the weld and HAZ, and it is equal to 350 MPa, which is also confirmed by the data obtained by X-ray structural analysis — 315 MPa. These stresses change from tensile into compressive ones in the base material. It is known that the stress magnitude is influenced by the chemical and phase composition of the welding consumables.

A factor which determines the process of residual stress formation in welding is the temperature field at the stable stage of the process in the plates being welded. Nonuniform heating of the welded joint in welding results in development of residual plastic shrinkage deformation, leading to formation of residual stresses. The nature of this stress distribution depends on many factors, (geometrical dimensions of the welded joint, welding mode, etc.). The zone heated in welding is covered by tensile stresses. The highest stress gradients coincide with the direction with the highest temperature gradients, i.e. residual stress distribution is typical for the field of intrinsic stresses formed under the conditions of nonuniform heating and cooling. Formation of tensile stresses caused by welding results in deterioration of the technological strength of the welded joint, which may lead to cracking in the welds and near-weld zone.

Rational development of the technology aimed at lowering the level of residual welding stresses as a result of reduction of the rigidity of welded joints and stress raisers allows avoiding cold cracking or facilitating their prevention using technological measures.

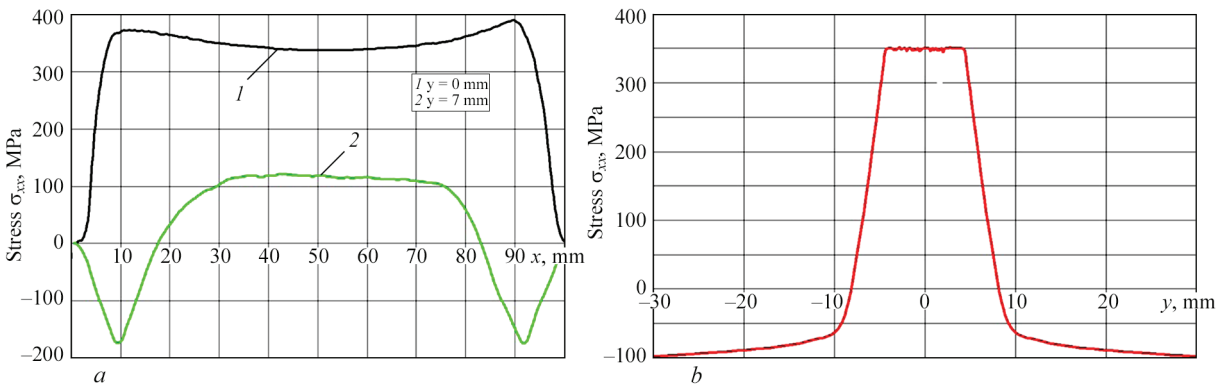

Figure 4. Distribution of residual longitudinal welding stresses: *a* — by welded plate length; *b* — in welded joint cross-section

DEVELOPMENT OF THE TECHNOLOGY OF EBW WITH A CONTROLLED COOLING RATE

Investigations by the authors of [11] conducted at PWI revealed that it is necessary to perform sample preheating to 450 °C prior to EBW, in order to prevent cold cracking in the welds at the heating stage.

Considering the above-said, we selected the temperature of 450 °C for preheating of the alloy at EBW. This method decreases the rate of temporary stress increase in welding and lowers the level of residual welding stresses [11].

Figure 5 shows a sample of 3 mm intermetallic of TiAl system, which was made by EBW with preheating in the following mode:

$$T_{\text{pre-heat}} = 450\ ^\circ\text{C},\ U_{\text{acc}} = 60\ \text{kV};\ I_{\text{b}} = 35\ \text{mA};$$
$$V_{\text{w}} = 7\ \text{mm/s};\ P = 5\cdot10^{-3}.$$

Preheating was performed by reciprocal motion of the gun with a defocused beam, which was unfolded by a special program.

As one can see from the Figure, the number of cold cracks across the welded joint on the surface of a 3 mm sample was reduced due to sample preheating up to the temperature T =450 °C before the start of the welding process, but it was not possible to completely prevent them.

As a result of theoretical studies of the stressed state by numerical experiment method it was found that preheating at the temperature of 450 °C promotes stress relaxation, and residual stresses σ_{xx} decrease by almost 40 % from 350 to 225 MPa (Figure 6).

As was noted above, stresses arising during welding, as well as the cooling rate which is ensured by local heat treatment (LHT), have a significant role in crack formation. This conclusion was the base for proposing the technological measure of welding sheet intermetallic plates with a controlled cooling rate.

This process allowed successively performing in one cycle the preheating, welding of 3 mm plates and postweld annealing, performed by a stationary gun by an unfolded electron beam for the entire sample.

Transverse stresses are also nonuniformly distributed. The middle part is exposed to tensile stresses, and the end portions — to compressive stresses. The magnitude of maximal stresses in the weld zone σ_{max} depends on weld length and, as a rule, is not higher than the value of 0.3 σ_{y} of the initial material, equal to 225 MPa in the weld center and to σ_{y} 837 MPa of the initial material. Thus, two zones can be singled out in the longitudinal direction in the butt welded joint: zone of tensile stress action and zone of compressive stress action.

The hot cracking susceptibility of the metal in welding is one of the main indices of their weldability.

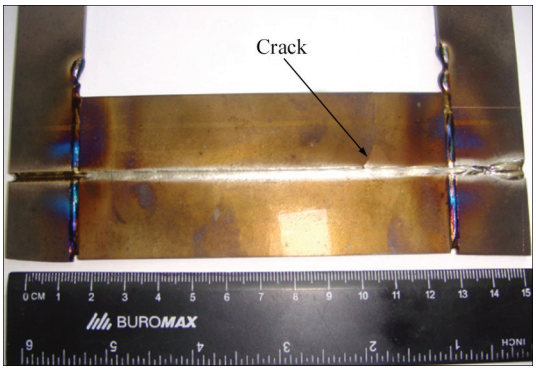

Figure 5. EB welded joint of 3 mm thick Ti–44Al–5Nb–3Cr–1.5Zr, at.% intermetallic alloy made with preheating, T = 450 °C

It ensures the technological strength of the materials in welding. Cold cracks can arise during phase and structural transformations in the solid state, practically immediately after welding.

As a result of generalization of previous research, it was shown that in addition to preheating, it is necessary to perform LHT right after welding by electron beam scanning along the weld immediately after welding is completed. It will allow lowering the rate of temporary stress increase in welding, as well as the level of residual welding stresses, which will enable lowering the cracking probability.

To solve this important task, as well as to optimize the structural and phase state of the intermetallic, the modes of welded joint LHT by the electron beam were developed.

In this case, postweld heat treatment was provided by the following program: immediately after completion of welding the electron gun was brought to the weld middle, the electron beam was unfolded and focused to the required configuration to one and to the other side from the weld middle to its end by a special computer program. It continued to heat the surface of the entire product in modes allowing compensation of excess heat removal and ensuring such a cooling rate which was taken by us as the optimal one. The frequency of electron beam scanning is 100 Hz, and the welding current decreases by 1/3.

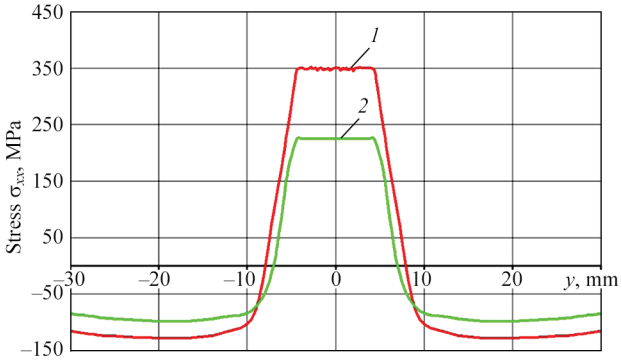

Figure 6. Computational estimate of the distribution of longitudinal residual stresses in the welded joint cross-section: *1* — without preheating; *2* — with preheating of the sample

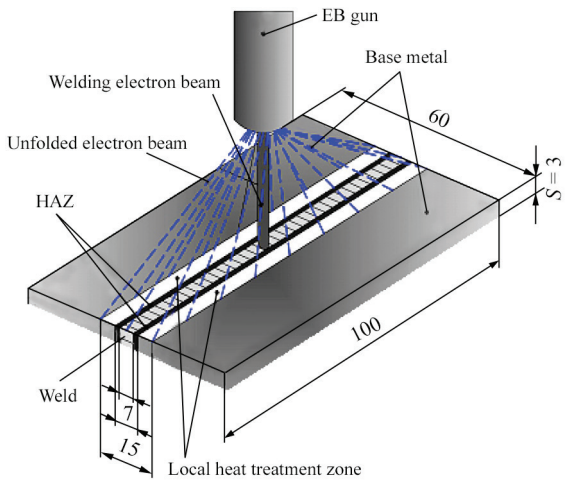

Figure 7. Scheme of EBW process with preheating and local heat treatment with a regulated cooling rate

The scheme of heat treatment with a controlled cooling rate is shown in Figure 7.

The total time of the abovementioned heat treatment was 10 min. Here, the welded joint temperature of 1000 °C was maintained for 5 min. The temperature of 1000 °C was selected because it was found earlier that appearance of β-phase as a result of phase transformations at cooling from the temperature of ~1000 °C has a plasticizing effect on the weld metal, thus increasing its ductility and toughness. After that, owing to a slow (~ 5 min) decrease of current by a special program, in keeping with the dependence, as shown in Figure 8, the welded joint was cooled to 500 °C temperature [12]. Then the electron gun was switched off, and slow cooling of the sample occurred. At slow cooling α-phase is transformed into lamellar $(\gamma+\alpha_2)$-phase, and a certain amount of B2-phase is preserved in the alloy, which is an ordered structure of β_0-phase [13].

EBW and LHT performed by the above scheme result in reduction of the rate of temporary stress increase and of the level of residual welding stresses. It allows avoiding the appearance of cold cracks and producing defectfree joints. These technological recommendations were used to produce a defectfree welded joint of 3 mm thick plates (Figure 8). Figure 9

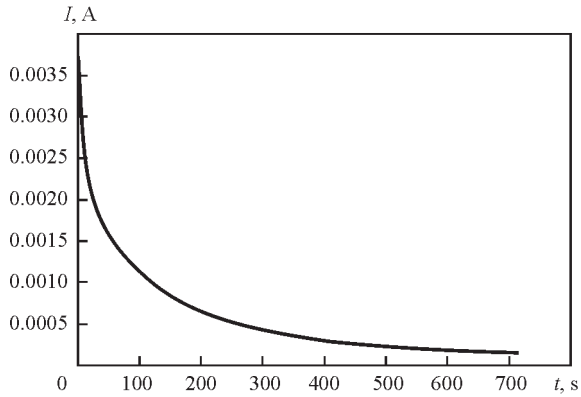

Figure 8. Dependence of current change on time to ensure controlled cooling of the weld across its thickness δ = 3 mm [10]

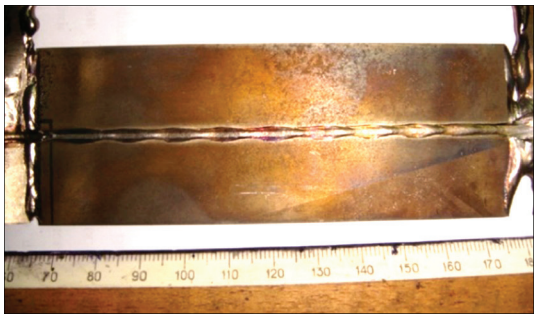

Figure 9. A sample of intermetallic alloy Ti–44Al–5Nb–3Cr–1.5Zr, at.%, δ = 3 mm after EBW and heat treatment by the scheme shown in Figure 7

shows the appearance of 3 mm thick sample, welded by the proposed scheme. The thermal cycle of the process of EWB of 3 mm intermetallic with preheating and local controlled annealing is shown in Figure 10.

Figure 10 also shows phase transformations during EBW with preheating and subsequent local heat treatment of 3 mm thick samples, which represent the structural transformations and fracture surface at different process stages.

As one can see from Figure 10, the weld metal has a three-component structure: γ-phase matrix, $(\gamma+\alpha_2)$-phase colonies and precipitates of residual δ-phase on the colony boundaries. Such a structure leads to increase of the HAZ ductility in 3 mm thick samples.

Moreover, the microhardness of all the regions of this sample subjected to preheating and subsequent local heat treatment is lower than the hardness of samples made without LHT application, as heat accumulation occurs, which leads to lowering of the sample cooling rate, and of internal stresses, respectively.

In work [10] it was established that at cooling of the intermetallic weld from 1000 °C temperature phase transformation takes place, due to which an additional β_0 (B2) phase appears in the structure, which is a Ti-based ordered phase. It is located on the colony boundaries and blocks crack initiation and propagation in α_2-phase as a result of stress lowering. Formation of a favorable three-component structure in the weld: γ-phase, $(\gamma+\alpha_2)$-phase and β-phase promotes an increase of its strength and ductility.

Fractures of welded joints of 3 mm thick titanium aluminides, welded with a controlled cooling rate, demonstrate a mixed fracture mode (with 30 % of the ductile component).

Fractogram of welded joint fracture surface reveals that cleavage facets observed in the fracture, are separated by tear regions, which are due to plastic shear.

Figure 11 shows that the stressed state of 3 mm thick intermetallic welded joint after LHT which allows lowering the level of residual welding stresses, ensures a slow cooling rate of the welded joints.

The cooling rate in this case decreased from 0.7 to 0.9 °C/s. In this connection, the residual welding

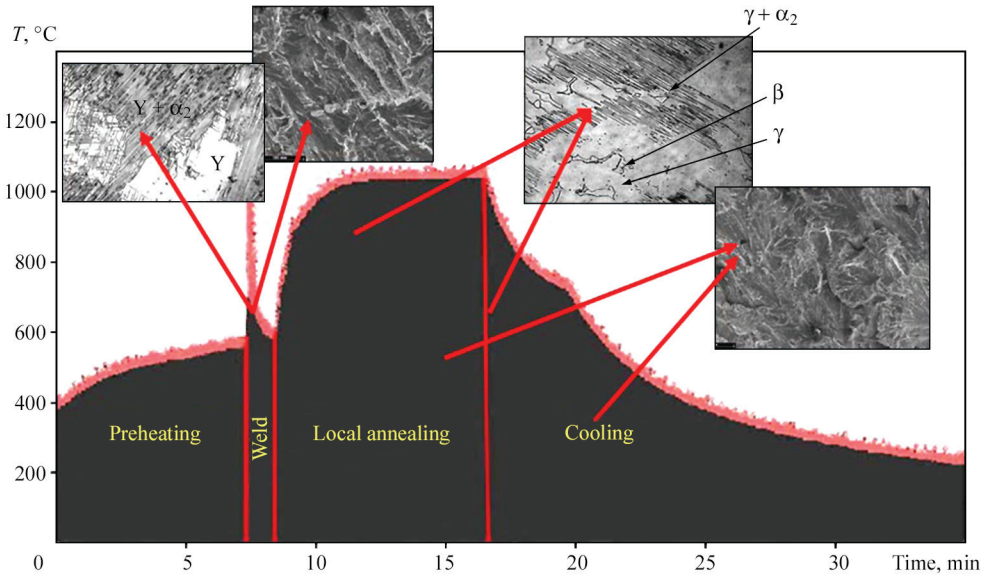

Figure 10. Influence of local heat treatment on the structural state of the welded joint of intermetallic alloy Ti–44Al–5Nb–3Cr–1.5Zr, at.%

Table 2. Ultimate strength of EB welded joints with LHT

Sample number	Thickness δ, mm	Value σ_t, MPa	Fracture site
1	3	310.9	BM
2	3	319.1	BM

Table 3. Ultimate strength of the intermetallic welded joints produced by EBW without LHT

Sample number	Thickness δ, mm	Value σ_t, MPa	Fracture site
1	3	197.8	BM
2	3	152.1	BM
3	3	175.5	BM

stresses decreased by almost 30 % and were equal to 162 MPa (Figure 11).

The data for plotting the graphs were derived using a mathematical model. The graph shows the changes in temperature, stressed state and cooling rate at application of this kind of heat treatment of 3 mm thick samples at the cooling stage. As one can see from the Figure, after 500 °C the change of sample temperature occurs very slowly. Here, the stresses are equal to 180 MPa.

The shape of σ_x curve is associated with a small width of the plate, at which the compressive stresses in its cross-section do not reach zero values.

Prevention of cold cracking and producing a defectfree joint due to a controlled cooling rate occur through lowering of the residual welding stresses, as well as formation of an optimal structure [14].

A lower level of stresses in the weld is attributable to formation of β-phase during cooling after welding, which promotes a significant relaxation of temporary stresses [10].

Static tensile testing was performed to assess the welded joint strength [14]. Results of mechanical testing of welded joint samples, obtained during tensile testing are given in Table 2.

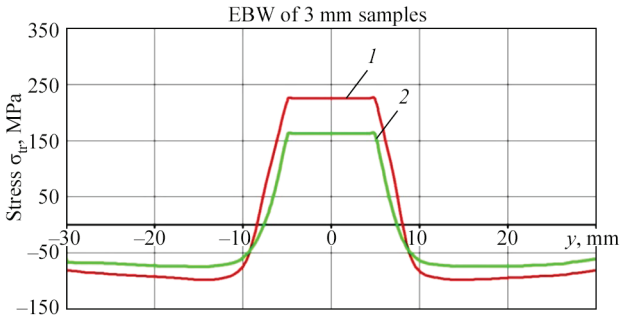

Figure 11. Computational evaluation of the distribution of residual longitudinal stresses in the cross-section of intermetallic welded joint, δ = 3 mm after: *1* — EBW with preheating; *2* — EBW with preheating and annealing at T = 1000 °C, t = 5 min

Mechanical testing of welded joints of samples made by EBW without LHT was conducted for comparison. Table 3 gives the test results.

As one can see from Tables 2 and 3, the ultimate strength values in samples welded using postweld local heat treatment are much higher than for samples produced without LHT application.

Analysis of the test data showed that postweld local heat treatment has a positive influence on the level of strength at mechanical testing, namely it allows increasing the ultimate strength of the welded joint approximately 1.8 times by average values from 175 to 315 MPa [15].

Thus, preheating and further postweld heating of the products, as well as selection of the optimal welding modes have a positive influence on reduction of the possibility of cracking.

CONCLUSIONS

1. It was established that in order to prevent cold cracking in welding sheet plates of TiAl system intermetallic, it is necessary to conduct preheating of the samples

and postweld local heat treatment of the welded joints. It was numerically demonstrated and experimentally confirmed that use of the distributed source of sample preheating before welding allows providing favourable conditions during welding and at further cooling, namely lowering the tensile stress magnitude.

2. A technology of electron beam welding of intermetallic has been developed, which envisages successive performance in one chamber of preheating, and electron beam welding of the intermetallic with postweld local heat treatment.

3. Modes of controlled cooling of 3 mm thick plates were proposed, which allow compensation of excess surface heat removal.

4. At application of this technology for 3 mm thick samples, it is recommended to perform heat treatment by an electron beam unfolded and defocused to one and the other side from the weld middle to its end with gradual lowering of its power using a special computer program. Here, the optimal welded joint cooling rate, which lowers the level of residual welding stresses by almost 30 % from 225 to 160 MPa and allows avoiding cracking in the weld is the rate of 0.7–0.9 °C/s.

5. Mechanical tensile testing of welded joints showed that sample fracture occurs through the initial material. Application of local heat treatment increases the level of ultimate strength of the welded joint approximately 1.8 times.

REFERENCES

1. Nochovnaya, N.A., Panin, P.V. (2014) *Analysis of residual macrostresses in welded joints of different class titanium alloys.* Moscow, VIAM [in Russian].
2. Iliin, A.A., Kalachev, B.A., Polkin, I.S. (2009) *Titanium alloys — composition, structure, properties.* Moscow, VILS-MATI [in Russian].
3. Makhnenko, V.I., Poznyakov, V.D., Velikoivanenko, E.A. et al. (2009) Risk of cold crack formation in welding of structural high-strength steels. *Zbirnyk Nauk. Prats NUK,* **3**, 5–12 [in Russian].
4. Mandelberg, S.L., Gordonny, V.G. (1961) One-sided two-layer argon-arc welding of thin sheet alloyed steel. *Avtomatich. Svarka,* **9**, 68–73 [in Russian].
5. Chen Guoqing, Zhang Binggang, Liu Wei, Feng Jicai. (2011) Crack formation and control upon the electron beam welding of TiAl-based alloys. *J. Intermetallics*, **19**, 1857–1863.
6. Zhuk, G.V., Trigub, N.P., Zamkov, V.N. (2003) Producing of titanium gamma-aluminide ingots using EB'HM method. *Special Electrometallurgy*, **1**, 19–21 [in Russian].
7. Nesterenkov, V.M., Bondarev, A.A. (2014) Electron beam welding of large-size thick-wall structures of magnesium alloys. *The Paton Welding J.,* **2**, 37–41.
8. Olshanskaya, T.V., Fedoseeva, E.M. (2019) Selection of main criteria of thermal cycle for methods of prediction of weld structure in electron beam welding. *Vestnik Permskogo NPU, Mashinostroenie, Materialovedenie,* 21(**2**), 73–81 [in Russian].
9. Piskun, N.V., Vrzhizhevskyi, E.L., Kostin, V.A. et al. (2022) Influence of time of existence of molten pool in electron beam processes on the level of evaporation of elements with a high vapor tension. *The Paton Welding J.,* **1**, 26–32. DOI: https://doi.org/10.37434/as2022.01.04
10. Velikoivanenko, E.A., Milenin, A.S, Rozynka, G.F. et al. (2019) Forecasting of inclination of welded joints of titanium γ-aluminide based alloy towards cold cracking under electron beam welding. *Tekhnologicheskie Sistemy,* **3**, 59–66 [in Russian]. DOI: https://dx.doi.org/10.29010/88.9
11. Zamkov, V.N., Velikoivanenko, E.A., Sabokar, V.K. et al. (2001) Selection of temperature of preheating of γ-titanium aluminide in electron beam welding. *The Paton Welding J.,* **11**, 17–20.
12. Lobanov, L.M., Asnis, A.E., Piskun, N.V. et al. (2019) Investigation of stress-strain state of welded joints of the system TiAl intermetallics. *The Paton Welding J.,* **11**, 8–11. DOI: https://doi.org/10.15407/tpwj2019.11.02
13. Imaev, V.M., Imaev, R.M., Gaisin, R.A. et al. (2017) Heat-resistant intermetallic alloys and composites based on titanium: Microstructure, mechanical properties and possible application. *Materials Physics and Mechanics,* **33**, 80–96.
14. Imaev, V.M., Imaev, R.M., Khismatullin, T.G. (2008) Mechanical properties of cast intermetallic alloy Ti–43Al–7(Nb, Mo)–0,2 V (at.%) after heat treatment. *Fizika Metallov i Metallovedenie,* 105(**5**), 516–522 [in Russian]. DOI: https://doi.org/10.1134/S0031918X08050098
15. Lobanov, L.M., Asnis, A.E., Piskun, N.V. et al. (2020) Influence of local heat treatment on mechanical properties of welded joints of TiAl system intermetallics produced by electron beam welding method. *Avtomat. Zvaryuvannya,* **9**, 36–41 [in Ukrainian]. DOI: https://doi.org/10.37434/as2020.09.04

ORCID

E.L. Vrzhyzhevskyi: 0000-0001-8651-8510,
N.V. Piskun: 0000-0003-1459-2310,
O.A. Velykoivanenko: 0009-0007-3704-2000,
I.I. Statkevych: 0000-0001-9403-2123,
T.G. Taranova: 0000-0002-2656-4693

CONFLICT OF INTEREST

The Authors declare no conflict of interest

CORRESPONDING AUTHOR

N.V. Piskun
E.O. Paton Electric Welding Institute of the NASU
11 Kazymyr Malevych Str., 03150, Kyiv, Ukraine.
E-mail: nadamova54@gmail.com

SUGGESTED CITATION

E.L. Vrzhyzhevskyi, N.V. Piskun, O.A. Velykoivanenko, I.I. Statkevych, T.G. Taranova (2024) Electron beam welding of sheet intermetallic alloy with a controlled cooling rate. *The Paton Welding J.*, **2**, 19–26.

JOURNAL HOME PAGE

https://patonpublishinghouse.com/eng/journals/tpwj

Received: 10.10.2023
Received in revised form: 06.12.2023
Accepted: 12.02.2024

DOI: https://doi.org/10.37434/tpwj2024.02.05

PLASMA-ARC SKULL MELTING AND CASTING OF AUSTENITIC STEEL WITH SUPER EQUILIBRIUM NITROGEN CONTENT

V.O. Shapovalov, V.P. Burnashev, T.I. Grishchenko, V.V. Yakusha, Yu.O. Nikitenko

E.O. Paton Electric Welding Institute of the NASU
11 Kazymyr Malevych Str., 03150, Kyiv, Ukraine

ABSTRACT

Shown is the possibility of melting and casting high-nitrogen Kh21G17AN2 steel under the conditions of plasma-arc skull melting. Boundary conditions of nit riding Kh12G17|N2 steel in order to produce sound castings were determined. Castings in the form of 12 mm wire were produced. Casting quality and properties were studied. Investigation of weldability of the produced steel with super equilibrium nitrogen content was conducted at manual argon-arc welding.

KEYWORDS: plasma-arc skull melting, Kh12G17N2 steel, nitrogen,, casting, properties, weldability

INTRODUCTION

Nitrogen n the composition of alloyed steels demonstrates austenite stabilizing properties, and it is used as a replacement of expensive nickel, which is traditionally added to form the austenite phase [1–3]. So far, a significant progress has been achieved in metallurgical production of steels alloyed by nitrogen. Development of high-nitrogen steels with special functional properties (high strength, corrosion resistance, biocompatibility, etc.) stimulates the increase of the scope of industrial application of nitrogen-containing steels in manufacture of products for critical purposes [4–6]. Steels containing nitrogen in the quantity greater than its solubility under equilibrium conditions are usually considered as high-nitrogen steels.

Ingots and castings from steels with super equilibrium nitrogen content are produced by a number of special electrometallurgy methods, namely high-pressure induction melting, electroslag remelting in a controlled atmosphere, plasma-arc remelting [7–10]. At present the method of autoclave induction melting is the most widely accepted technique for producing nitrogen-containing steels. Not considering the popularity of this method, it has certain significant disadvantages, which are associated with the long-time process of melting and soaking of the liquid metal at excess pressure and complexity of the technological equipment, while the obvious advantages of this method occurring in production of steels with nitrogen concentration below the equilibrium one (approximately 0.4 %), are practically absent, when producing high-nitrogen steels. Contrarily to the above-mentioned melting processes, at plasma-arc remelting of nitrogen-containing steels nitrogen additionally interacts with the liquid metal surface in an excited condition, which allows obtaining its super equilibrium concentration in the metal, and significantly intensifying the absorption process, shortening the processing duration by an order [8]. Relative simplicity of the technological equipment, performance of metal remelting at significantly lower gas pressures, no need for long-term soaking of liquid metal at excess pressure show the good prospects for plasma-arc processes when producing steels with super equilibrium nitrogen content.

Alongside the need to produce ingots from high-nitrogen steels, not less important is producing shaped castings from them. Increase of the requirements to casting quality, as well as expansion of manufacturing of cast products from nigh-nitrogen steels, requires development of new technology solutions, which will ensure the high quality of the melted and cast metal. The complex of practical measures to improve the casting quality is chiefly aimed at improvement of the processes of melting and treatment of liquid metal, including deoxidizing, refining, alloying; metal pouring into moulds in modes ensuring high physical-mechanical properties of the castings; engineering casting moulds based on materials with high physical-mechanical and thermophysical properties to ensure maximum closeness of casting dimensions to those of the finished parts.

As a variety of plasma-arc processes, the method of plasma-arc skull melting [11, 12] allows conducting melting and pouring of nitrogen-containing steel in one process installation. For melting sound metal and ensuring high technical and economic indices of the melting process the skull crucible should meet the following requirements: prevent interaction of crucible material with the molten metal, ensure the required time of metal soaking in the liquid state; and provide the maximal coefficient of metal pouring (K_p).

Interaction of liquid metal with the crucible material can be prevented, using a metal, for instance, copper water-cooled crucible, which improves the operational conditions of the melting installation and contributes to casting quality.

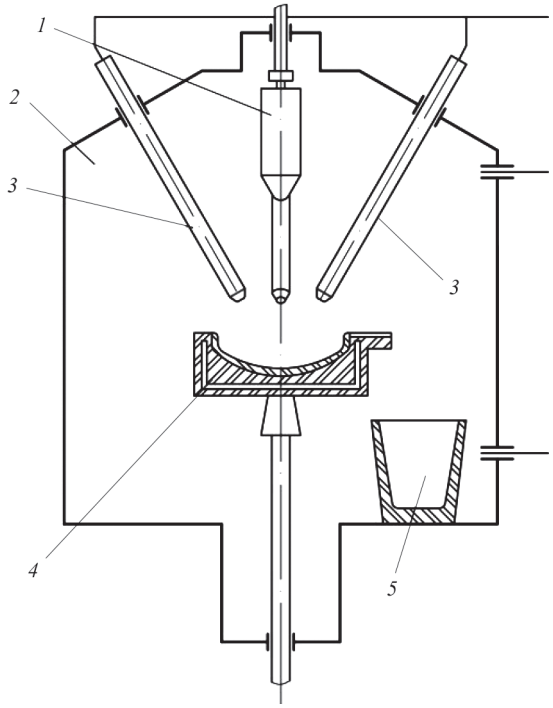

Figure 1. Block-diagram of UPG-1L plasma-arc installation: *1* — consumable billet; *2* — furnace chamber; *3* — PDM-7 plasmatrons; *4* — crucible; *5* — mould

Development of methods to join nitrogen-containing steels by welding is one of the priority tasks for rational manufacture of both the individual parts, and elements of structures from them [6, 13]. Austenitic steels with super equilibrium nitrogen content have limited weldability when arc welding methods are used. Steels containing more than 0.5 % nitrogen are prone to porosity. Weld porosity in welding is influenced not only by absolute nitrogen content, but also by the conditions of weld pool existence (volume, shape, welding speed, preheating temperature). It is noted that lowering of welding energy input promotes reduction of the total number of defects and their dimensions. Lowering of welding current to 80 A, and increase of the number of passes to 3–4 promotes a reduction of the total number of pores in the welds [14].

RESEARCH OBJECTIVE

The objective of research conducted in this work, consisted in optimizing the technological modes of plasma-arc skull melting (PASM) and casting of Kh21G17N2 steel sparsely-alloyed by nickel with super equilibrium nitrogen content, studying the features of nitrogen influence on its structure, determination of the parameters of TIG welding of high-nitrogen steel samples and welded joint characteristics.

Figure 2. Copper water-cooled mould

EQUIPMENT AND MATERIALS

Investigations of the technological features of the process of PASM and casting of high-nitrogen steel were conducted in plasma-arc skull installation UPG-1L developed by PWI (Figure 1). Plasma-arc installation was fitted with a copper water-cooled crucible of 1000 cm^3 volume (Figure 2) and DC plasmatrons of PDM-7 type with up to 500 A admissible current.

The melting-pouring installations with a radial heating scheme enable either dispersing heat input to the pool surface or concentrating it in the specified zones, adjusting the heating of different regions of the liquid metal pool. With such a heating scheme the surface of the billet being remelted partially shields the plasma arc radiation, thus increasing the thermal efficiency of melting.

Two-phase austenitic-ferritic Kh21G17N2 steel was selected as the initial material for investigations. Chromium of Kh98 grade, Armco iron, cathode nickel of N1 grade, metallic manganese MP-1 were applied to produce the grade chemical composition. Initial charge was used to melt under PASM conditions samples of steel, the chemical composition of which is given in Table 1.

Results of chemical analysis of steel of melt 1 showed a lower content of manganese and nickel, compared to calculated values. Correction of the composition of charge materials for subsequent melts 2 and 3 ensured melting steel of the required grade composition. Obtained steel compositions were used to melt samples with super equilibrium nitrogen concentration.

Table 1. Chemical composition of produced steel, wt.%

Melt	Cr	Mn	Ni	C	S	P	[O]	[N]
1	20.4	13.9	1.67	0.1	0.025	0.02	0.042/0.03	0.016/0.73
2	20.9	16.8	1.90	–»–	–»–	–»–	–»–	0.018/0.74
3	21.0	16.9	2.10	–»–	–»–	–»–	0.023/0.028	0.017/0.90
Note. [O] and [N] content in the initial metal is shown in the numerator; in the metal after nitriding — in the denominator.								

EXPERIMENTAL INVESTIGATIONS

MELTING AUSTENITIC Kh21G17AN2 STEEL WITH SUPER EQUILIBRIUM NITROGEN CONTENT

Under the conditions of excess gas pressure in the melting chamber and distributed heating of liquid metal pool chromium evaporation is practically absent, small losses of manganese are observed, which can grow somewhat with lowering of total gas pressure and increase of plasma-forming gas flow rate.

Dependence of nitrogen solubility on melt temperature and partial pressure of nitrogen in the furnace atmosphere was calculated for the respective chemical composition of the produced steels (Table 1), using an equation given in work [10]:

$$\lg k = -\frac{293}{T} - 1.16 - \left(0.042 - \frac{167}{T}\right)[\text{Cr}\,\%] -$$
$$-0.5\left(\frac{3{,}3}{T} - 0.001\right)[\text{Cr}\,\%]^2 - \left(0.022 - \frac{73}{T}\right)[\text{Mn}\,\%] -$$
$$-\left(\frac{18.4}{T} + 0.00042\right)[\text{Ni}\,\%] - \left(\frac{171}{T} - 0.031\right)[\text{Si}\,\%] -$$
$$-\left(\frac{274}{T} - 0.06\right)[\text{C}\,\%] - \left(\frac{1640}{T} - 1.14\right)[\text{O}\,\%] -$$
$$-\left(\frac{859}{T} - 0.487\right)[\text{Al}\,\%].$$

In keeping with the conducted calculations, standard solubility of nitrogen in steels at melt temperature of 1873 K was equal to 0.49 and 0.57 %, respectively for melt 1 and melts 2 and 3. It was determined that with melt temperature increase by 100 K the standard solubility of nitrogen in the metal decreases by 17 % on average, and at increase of nitrogen partial pressure in furnace atmosphere by 100 kPa it grows by 40 %.

Calculated data on nitrogen solubility were used at optimization of technological modes of PASM of Kh21G17N2 steel with super equilibrium nitrogen content. Experimental melts were conducted in UPG-1L furnace, using a plasma-forming mixture of nitrogen and argon gases. Gas flow rate was equal to 80 l/min. Metal melting and soaking were performed at plasmatron current of 280–300 A and 70 V voltage. According to the data in Table 2, the required working pressure of gases was maintained in the furnace chamber, and the specified partial pressure of nitrogen was provided.

PRODUCING CASTINGS FROM AUSTENITIC Kh21G17AN2 STEEL WITH SUPER EQUILIBRIUM CONTENT OF NITROGEN

The method of conducting the melting at excess pressure of nitrogen allows treating the metal not only during its melting, soaking and pouring, but also during its solidification. It greatly widens the possibility of controlling the gas-shrinkage, liquation and other processes at formation of the casting structure to improve the density and other physical-mechanical properties of the metal.

Table 2. Parameters of pressure and composition of plasma-forming gas mixture

Melt	Working pressure in the chamber, kPa	Nitrogen content in the gas mixture, vol.%	Partial pressure of nitrogen during melting, kPa
1	185	85–86	160
2	200	–»–	170
3	210	–»–	180

The main problem of producing the ingots and castings from steels with super equilibrium nitrogen content is related to the high probability of formation of gas porosity in the metal at its hardening. It is known that the limit concentration of nitrogen at plasma-arc treatment of the melt is determined by nitrogen boiling of the metal pool, from the viewpoint of technology, which is indicative of reaching the dynamic equilibrium of the sorption process at these thermodynamic conditions [8, 15]. Its value is determined by the conditions of existence of gas bubbles in the melt volume, and it is in equilibrium with the total pressure of gases in the furnace, and not with partial pressure of nitrogen. Further increase of partial pressure of nitrogen does not influence its content in the metal. The start of nitrogen boiling of the pool depends on nitrogen absorption rate, convection conditions, standard solubility of nitrogen in the melt and total gas pressure in the melting chamber.

Application of such a technological measure as gas pressure increase in the furnace chamber during metal pouring into the mould allows inhibiting the dissolved nitrogen desorption in the metal and preventing gas porosity formation. In work [11], devoted to PASM of critical castings from 0Kh20N5AG2 steel with super equilibrium nitrogen content, a nomogram was proposed for determination of limit pressure of gas in the plasma-arc furnace, which should be maintained at pouring to produce porefree castings. Guided by the theoretical principles of this work, the respective nomogram was plotted for the studied Kh21G17AN2 steel (Figure 3). The nomogram contains two dependencies, one of which corresponds to limit concentration of nitrogen in steel in the mode of nitrogen boiling of the pool, depending on total gas pressure in the furnace (curve *1*) and the second corresponds to nitrogen content in steel, depending on nitrogen partial pressure (curve *2*). Proceeding from nitrogen content in Kh21G17AN2 steel which should be achieved a horizontal line is drawn up to intersection with dependencies 1 and 2. The abscissas of the points of their intersection indicate the limit pressure of gases in the furnace chamber at metal pouring to ensure solid cast products and the partial pressure of nitrogen, required to produce metal with the specified nitrogen content.

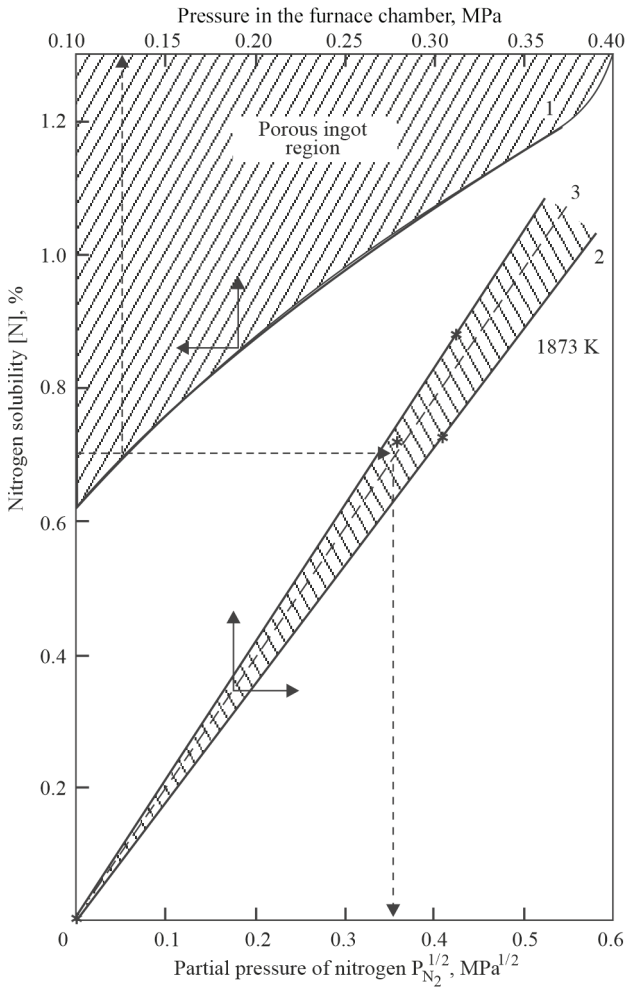

Figure 3. Nomogram for determination of limit pressure at pouring under the conditions of PASM of nitrogen-alloyed steels: *1* — nitrogen solubility calculated under the conditions of metal pool boiling using equation $[N] = S_N\sqrt{P_\Sigma}$, where S_N is the standard nitrogen solubility, %; P_Σ is the total pressure of gases, at; *2* — dependence of nitrogen content in steel on nitrogen partial pressure; *3* — isotherm of nitrogen solubility in steel at 1873 K

Used as a mould in the experiments was a detachable steel mould (Figure 4), which as a result of one-time pouring ensured metal crystallization in the form of cylindrical rods (18 pcs) of 12 mm diameter and 180 mm length (Figure 5). After metal melting and inducing the pool, the melt was soaked for 10–15 min under the conditions of plasma-arc heating at the specified partial pressure of nitrogen, eliminating the possibility of its nitrogen boiling, and then the treated metal was poured into the mould. During metal melting the pressure of gases in the furnace and the composition of plasma-forming mixture were maintained in keeping with the data given in Table 2.

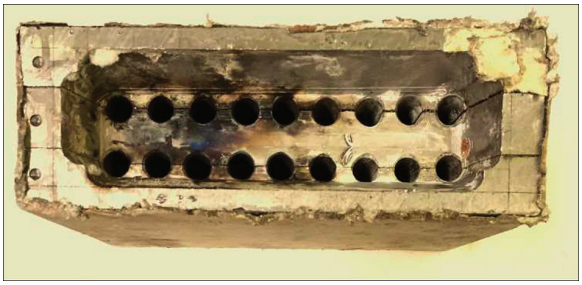

Figure 4. Detachable steel mould

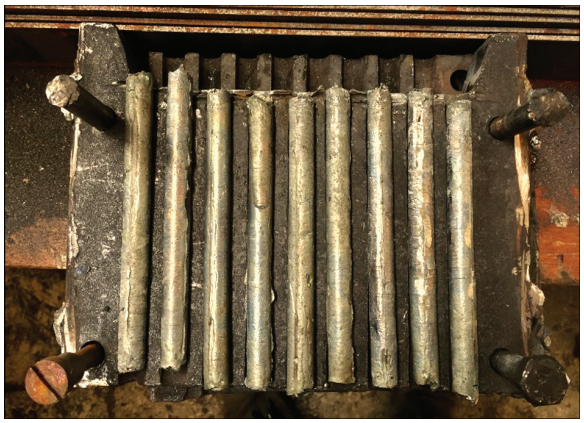

Figure 5. Appearance of the mould with cast rods

Produced castings were used to prepare longitudinal macrosections to study the cast structure of the rods and to take samples for chemical and gas analysis.

INVESTIGATIONS OF TIG WELDING OF SAMPLES FROM NITROGEN-ALLOYED AUSTENITIC STEEL Kh21G17AN2

Weldability of high-nitrogen Kh21G17AN2 steel was studied in the case of manual nonconsumable tungsten electrode argon-arc welding. With this purpose 6 and 3 mm plates were produced from the rods by rolling. Rectangular samples were directly made from 6 mm plates for optimization of the welding technology. Milling of the edges was performed from the welding side on the adjacent faces of the samples on both sides. The 3 mm plates were used to produce filler material in the form of the so-called “noodles”. Thus, filler electrodes of the same steel grade were applied for TIG welding of samples of Kh21G17AN2 steel. Butt welding of the samples was performed, conducting it in two passes from both sides, in keeping with the welding modes, given in Table 3.

The produced welded joint samples were used to prepare transverse macrosections to study the metal structure in the joint zone. Mechanical properties of the welded joints and their nitrogen and oxygen content were additionally studied.

Figure 6. Macrostructure of the longitudinal section of rods with different nitrogen content, %: *1* — 0.73; *2* — 0.74; *3* — 0.9

Table 3. Modes of manual argon-arc welding

Sample	Voltage, V	Current, A	Gas composition, %		Gas flow rate, l/min	Welding speed, cm/s	Number of passes
			Ar	N_2			
1	20	100	80	20	10	0.20	2 from each side
2	18	80	90	10	–»–	0.15	–»–

Table 4. Mechanical properties of the welded joint

Sampling area	$\sigma_{0.2}$, MPa	σ_t, MPa	δ, %	ψ, %	*KC,* MJ/mm^2	Fracture site
Base metal	841	933.0	25.9	42.7	1.45	–
Weld	540	860.0	28.0	41.2	1.58	Weld

Table 5. Content of gas admixtures in the metal of the weld of Kh21G17AN2 steel welded joint

Gas admixtures	Base metal	Weld metal				
		1	2	3	4	5
[O]	0.042	0.033	0.028	0.032	0.036	0.034
[N]	0.74	0.74	0.73	0.74	0.73	0.74
Note. 1–5 are samples taken every 25 mm along the weld length.						

DISCUSSION OF THE RESULTS

As a result of the conducted experiments, technological modes of alloying Kh21G17N2 steel of austenitic-ferritic grade by nitrogen from the gas phase in plasma-arc skull melting and its pouring into a steel mould. Castings from high-nitrogen steel were produced in the form of small diameter rods. The results of gas analysis of the rods by Kjeldahl, given in Table 1, show that nitrogen content in the rods of all the three batches exceeds the standard nitrogen solubility by more than 1.3 times, being equal to 0.73, 0.74 and 0.9 % for melts 1, 2, and 3, respectively. Comparing the derived concentrations with the calculated values of equilibrium nitrogen content at 1873 K, it was found that the nitriding mode, followed during melts 1 and 3, ensures such a nitrogen concentration in the castings, which is by 7 and 15 % higher than the equilibrium one, respectively. Investigations of the cast structure of the rods showed that the rods of the first and second melt are solid, without visible pores or nonmetallic inclusions in the macrosection field of vision (Figure 6). In both the cases metal pouring into the mould was performed at the total gas pressure in the furnace higher than the limit gas pressure determined by the nomogram (Figure 3). Coarse pores of 0.5 to 2.0 mm diameter were found in the entire thin section field in the body of the rods of the third melt. Despite the fact that metal pouring was conducted at the pressure exactly corresponding to the limit value (Figure 4), it turned out to be insufficient to prevent gas porosity for this concentration of nitrogen,. Thus, in order to inhibit development of this process, it is necessary to maintain a pressure during pouring with a certain excess over the one determined by the nomogram.

Performed weldability studies of high-nitrogen Kh21G17AN2 steel showed that the mechanical properties of the weld and base metal are within the expectations (Table 4). Somewhat lower ultimate strength (σ_t), yield limit ($\sigma_{0.2}$) of weld metal, but higher relative elongation (δ) and impact toughness (*KC*) are noted.

Analysis of gas admixtures content in the welded joint showed that compared to base metal a certain lowering of oxygen is found, while nitrogen concentration practically does not change (Table 5). The proposed welding modes ensure formation of a joint with a pool of limited dimensions and short time of its existence, which, probably does not allow development

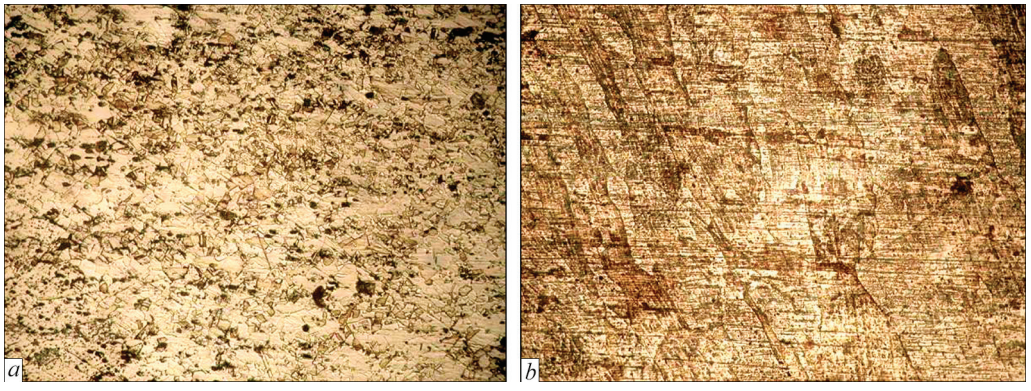

Figure 7. Microstructure (×100) of base (wrought) metal (*a*) and weld (*b*)

of the reaction of nitrogen desorption from the weld metal or porosity formation.

Metallographic studies of the weld and base metal (Figure 7) showed that their microstructure is completely austenitic. No pores, cracks or other defects were detected in the joint. Considering the above data, one can state weldability of high-nitrogen Kh21G17AN2 steel is satisfactory.

CONCLUSIONS

1. Conducted investigations showed that the PASM technology allows actively conducting alloying by nitrogen from the gas phase of Kh21G17AN2 steel sparsely-alloyed by nickel, producing castings with a super-equilibrium nitrogen content and austenitic structure.

2. It is found that in order to produce castings without defects in the form of pores, it is necessary to conduct pouring of Kh21G17AN2 steel at total gas pressure in the plasma furnace, exceeding the limit pressure of gases, determined using a nomogram.

3. Experiments on weldability of Kh21G17AN2 steel show that the proposed modes of argon-arc welding ensure satisfactory mechanical characteristics of the welded joint, without porosity or cracks in the HAZ or weld metal.

REFERENCES

1. Uggowitzer, P.J., Magdowski, R., Speidel, M.O. (1996) Nickel free high nitrogen austenitic steels. *ISIJ Inter.*, 36(**7**), 901–908. DOI: https://doi.org/10.2355/isijinternational.36.901
2. Gavriljuk, V., Petrov, Y., Shanina, B. (2006) Effect of nitrogen on the electron structure and stacking fault energy in austenitic steels. *Scr. Mater*., **55**, 537–540. DOI: https://doi.org/10.1016/j.scriptamat.2006.05.025
3. *Nithi* Saenarjhan, Jee-Hyun Kang, Sung-Joon Kim (2019) Effects of carbon and nitrogen on austenite stability and tensile deformation behavior of 15Cr–15Mn–4Ni based austenitic stainless steels. *Materials Sci. and Eng.*, *A*, **742**, 608–616. DOI: https://doi.org/10.1016/j.msea.2018.11.048
4. Patnaik, L., Maity, S.R., Kumar, S. (2020) Status of nickel free stainless steel in biomedical field: A review of last 10 years and what else can be done. *Mater. Today Proc*., **26**, 638–643. DOI: https://doi.org/10.1016/j.matpr.2019.12.205
5. Chail, G., Kangas, P. (2016) Super and hyper duplex stainless steels: Structures, properties and applications. *Procedia Structural Integrity*, **2**, 1755–1762. DOI: https://doi.org/10.1016/j.prostr.2016.06.221
6. Mohammed, R., Madhusudhan Reddy, G., Srinivasa Rao, K. (2017) Welding of nickel free high nitrogen stainless steel: Microstructure and mechanical properties. *Defence Technology*, 13(**2**), 59–71. DOI: https://doi.org/10.1016/j.dt.2016.06.003
7. Sheiko, I.V., Grigorenko, G.M., Shapovalov, V.A. (2016) Alloying of steels and alloys with nitrogen from the arc plasma. Theory and practice (Review. Pt 1). *Sovrem. Elektrometall.,* **1**, 32–37 [in Russian].
8. Paton, B.E., Grigorenko, G.M., Sheiko, I.V. et al. (2013) *Plasma technologies and equipment in metallurgy and foundry.* Kyiv, Naukova Dumka [in Russian].
9. *Nabil* Ghali, S., Eissa6 M., El-Faramawy, H. et al. (2013) Production and application of advanced high nitrogen steel. In: *Proc. of Inter. Conf. on Sci. and Technology of Ironmaking and Steelmaking* At. Jamshedpur, India, 1. DOI: https://www.researchgate.net/publication/262698868_Production_and_Application_of_Advanced_High_Nitrogen_steel
10. Burnashev, V.P., Nikitenko, Yu.O., Yakusha, V.V. et al. (2020) Some aspects of melting high-nitrogen steel Kh21G17AN2 in plasma arc furnace. *Suchasna Elektrometal.,* **2**, 23–26 [in Ukrainian]. DOI: https://doi.org/ 10.37434/sem2020.02.04
11. Granovsky, V.K. (1982) *Study of physical-chemical processes and development of technology of plasma-arc skull melting of high-nitrogen steels and alloys*: Syn. of Thesis for Cand. of Tech. Sci. Degree. Kyiv [in Russian].
12. Burnashev, V.R., Zhadkevich, M.L., Shapovalov, V.A. (2002) Plasma-arc skull melting and casting of refractory metals and alloys. *Advances in Electrometallurgy,* **2**, 30–33.
13. Zeng, Liu, Chenglei, Fan, Chunli, Yang et al. (2022) *Dissimilar welding of high nitrogen stainless steel and low alloy high strength steel under different shielding gas composition: Process, microstructure and mechanical properties. Defence Technology*. DOI: https://doi.org/10.1016/j.dt.2022.10.010
14. Yushchenko, K.A., Solokha, A.M., Kazennov, N.P. (1989) Technological peculiarities of welding of high-nitrogen steels. In: *Proc. of Inter. Conf. on High-Nitrogen Steels 89 (1–3 October, 1989, Varna, Bulgaria)*, Vol. 2, 12–15 [in Russian].
15. Erokhin, A.A. (1975) *Plasma-arc melting of metals and alloys.* Moscow, Nauka [in Russian].

ORCID

V.O. Shapovalov: 0000-0003-1339-3088
V.P. Burnashev: 0000-0001-6807-3810,
T.I. Grishchenko: 0000-0001-7840-9832,
V.V. Yakusha: 0000-0001-5962-9194,
Yu.O. Nikitenko: 0000-0002-3603-2333

CONFLICT OF INTEREST

The Authors declare no conflict of interest

CORRESPONDING AUTHOR

V.O. Shapovalov
E.O. Paton Electric Welding Institute of the NASU
11 Kazymyr Malevych Str., 03150, Kyiv, Ukraine.
E-mail: vash52@ukr.net

SUGGESTED CITATION

V.O. Shapovalov, V.P. Burnashev, T.I. Grishchenko, V.V. Yakusha, Yu.O. Nikitenko (2024) Plasma-arc skull melting and casting of austenitic steel with super equilibrium nitrogen content. *The Paton Welding J*., **2**, 27–32.

JOURNAL HOME PAGE

https://patonpublishinghouse.com/eng/journals/tpwj

Received: 12.06.2023
Received in revised form: 07.12.2023
Accepted: 14.02.2024

DOI: https://doi.org/10.37434/tpwj2024.02.06

EFFECTIVENESS OF UNLOADING NPP PIPELINE SECTION WITH A PIPE WALL THINNING DEFECT BY MOUNTING A BAND OR A WELDED COUPLING

G.V. Vorona, O.V. Makhnenko, O.S. Milenin

E.O. Paton Electric Welding Institute of the NASU
11 Kazymyr Malevych Str., 03150, Kyiv, Ukraine

ABSTRACT

Formation of erosion-corrosion wear defects in NPP pipelines is one of the urgent problems of nuclear power engineering. During pipeline repair, a defective section is cut out and a new pipe spool is mounted using welding, which is a rather labour-consuming process, and requires draining of the transported liquid. To prolong the service life, a defective pipeline section can be reinforced by mounting a repair structure, for instance a band or a welded coupling. In order to substantiate the rationality of application of reinforcing structures in pipeline repair, the finite element analysis of the stress-strain state of a rectilinear pipeline section with an erosion-corrosion wear defect under the impact of internal pressure, as well as evaluation of the effectiveness of unloading a defective section in the case of application of a reinforcing structure of the type of a band or a welded coupling in repair were performed. The analysis results have shown a high effectiveness of applying such structures. The obtained results can be used in substantiation of introduction of alternative technologies for repair of pipelines in the Ukrainian NPP, predominantly technological ones, particularly in those cases when repair by traditional methods is not possible or rational for technical or economic reasons.

KEYWORDS: NPP, pipeline, erosion-corrosion wear, wall thinning defect, reinforcing structure, band, coupling, stress-strain state, ductile fracture, finite element method

INTRODUCTION

Formation of erosion-corrosion wear (ECW) defects in pipelines of nuclear power plants (NPP) is one of the urgent problems in nuclear power engineering [1, 2]. Erosion-corrosion wear is a combination of two processes - mechanical wear of the pipeline wall metal due to the action of erosion and chemical fracture due to the action of corrosion [3–5]. As a result of the combination of these two phenomena, the resistance of a pipeline to loads decreases and the tendency to the occurrence of critical defects and material fracture grows [1, 6, 7].

In practice, in case of ECW detection, a defective section of an NPP pipeline is cut out and a new pipe spool is mounted using welding. Such repair takes place during shutdown of a power unit and when it is possible to drain the transported liquid. Also, an alternative technology is available, namely, to prolong the service life, a defective pipeline section can be reinforced by mounting a repair structure, for instance a band or a welded coupling [8–10, 15]. Pipeline banding is reinforcing with metal rings, a band, a wire or nonmetallic materials along the perimeter of its wall. Possible options as to the method of mounting a band in the form of metal rings on a defective pipeline section are shown in Figure 1. Mounting a welded coupling (Figure 2) is used to reinforce a defective section and eliminate leakage by sealing a reinforcing structure with welds. Repair with mounting a coupling or

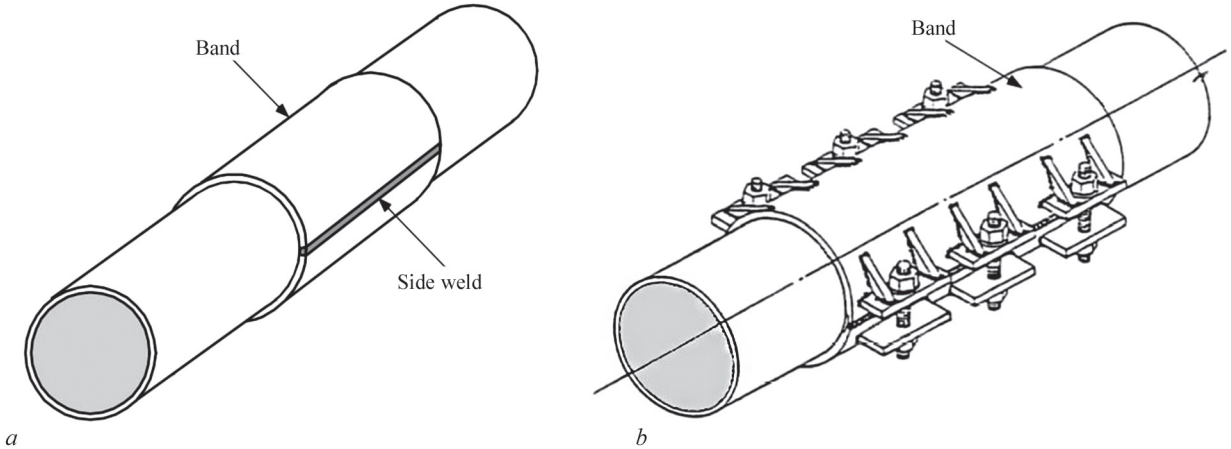

Figure 1. Types of bands according to the method of mounting: *a* — welded; *b* — on bolted joints

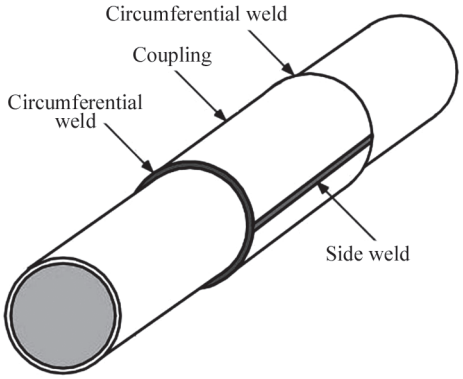

Figure 2. Reinforcing a defective pipeline section with a welded coupling

a band may be rational, as it is less labour-consuming than replacing the entire section, does not require draining the liquid from the pipeline and can be performed even when a power unit is operating.

A band differs from a coupling in the fact that it is mounted on the pipeline without welding-on to the supporting pipe. It provides reinforcement of a defective section and, if necessary, can be easily dismantled for a major pipeline repair. A band can also be used multiple times. The use of a band is rational only for those defects that will not lose their tightness over a long period of operation or as a temporary measure before the next planned repair [9].

THE AIM OF THE WORK

is to substantiate the use of alternative repair technologies for pipelines with ECW defects for the needs of nuclear power engineering, to develop mathematical models and to conduct a finite element analysis of the stress-strain state (SSS) of a rectilinear pipeline section with an ECW defect under the action of internal pressure, as well as to evaluate the effectiveness of unloading a defective section in the case of using a reinforcing structure of the type of a band or a welded coupling in the repair.

When assessing the admissibility of a pipeline section with an ECW defect for further operation, the limiting condition of the pipeline is evaluated from the point of view of ductile fracture, for example, based on the results of predicting the intensity of plastic deformations in the defect zone. The influence of the geometric parameters of a reinforcing structure (thickness, length, and initial gap between the outer surface of the pipeline and the inner surface of a reinforcing structure) on the operability of a rectilinear pipeline section with an ECW defect was investigated using the finite element method.

PROBLEM STATEMENT

As an example, a rectilinear pipeline section was considered, which has standard dimensions and loading parameters for NPP technological pipelines (material — steel 20): outer diameter D = 630 mm, wall thickness s = 25 mm, design pressure P = 11.8 MPa, temperature T= 300 °C.

The critical, i.e., unacceptable geometric parameters of a pipeline wall thinning defect (Figure 3) were determined in accordance with the MT-T.0.03.224-18 procedure [11, 18], which regulates the procedure for calculating the allowable thickness of elements of NPP pipelines of carbon steel, which are subjected to erosive and corrosive wear and which was put into operation by the SE NNEGC “Energoatom” in 2019. An express assessment of the acceptability of a pipeline section with different geometric parameters of an ECW defect for further operation was carried out and based on its results, the dimensions of a critical wall thinning defect were determined, namely, an idealized ECW defect of a semi-elliptical shape with a length $2L = 4s$ = 100 mm, width $2h = 2s$ = 50 mm, with a depth a = 20 mm (Figure 3).

The dimensions of a reinforcing structure of the type of a band and a coupling were chosen as follows (Figure 4): inner diameter D = 630 mm, half-length L_b = 630 mm, thickness $s_b = s$ = 25 mm. The geometric

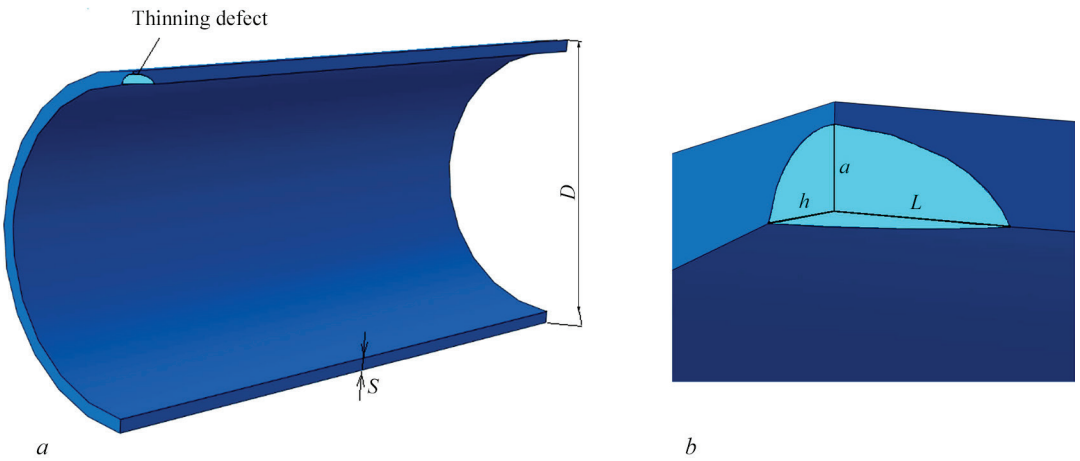

Figure 3. Geometric model of 1/4 of a rectilinear defective pipeline section (*a*) and internal semi-elliplyptical wall thinning defect (*b*)

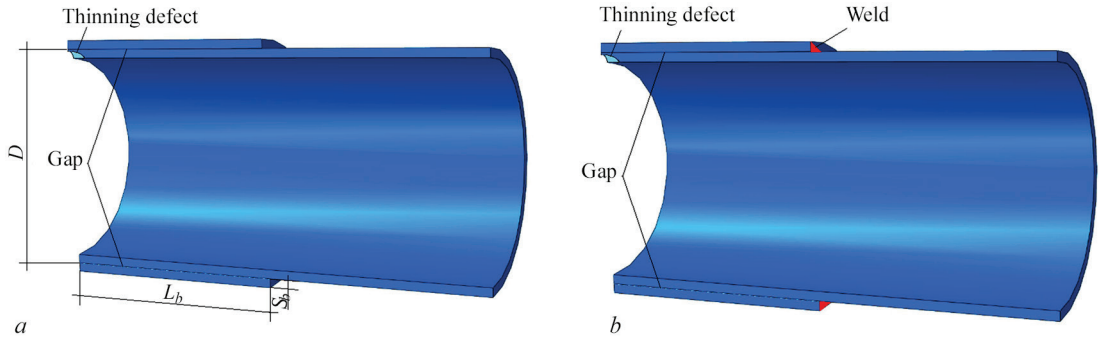

Figure 4. Geometric models of a rectilinear pipeline section, reinforced by a band (*a*) or a welded coupling (*b*)

models of a band and a welded coupling differ only in the presence of circumferential welds for joining a coupling to the pipeline.

DEVELOPMENT OF FINITE ELEMENT MODEL

According to the specified parameters, a geometric and finite element model of a rectilinear pipeline section with a thinning defect was built (Figure 3). Taking into account the presence of two planes, the model includes 1/4 of this pipeline section with a defect. The following mechanical properties of the material were used: Young's modulus $E = 2.1 \cdot 10^5$ MPa, Poisson's ratio $\mu = 0.3$, yield strength for steel 20 at a temperature of $T = 300$ °C, $\sigma_y = 177$ MPa [12]. Similarly, finite element models with the use of reinforcing structures of the type of a band and a welded coupling were created (Figures 4, 5).

The problem of SSS of a pipeline section is considered in an elastic-plastic formulation, since under the action of internal pressure in the zone of a wall thinning defect, the formation and propagation of plastic deformations is probable. Deformation strengthening of the material in the developed model of elastic-plastic deformation is not taken into account, which makes the model more conservative in terms of determining plastic deformations. The design pressure $P = 11.8$ MPa is applied to the inner surface of the pipeline and the defect zone. The boundary conditions in the form of axial tensile stresses σ_{zz} are added to the end surface of the model having the value [14]:

$$\sigma_{zz} = \frac{P\frac{D}{2}}{2s} \rightarrow \sigma_{zz} = 72.6 \text{ MPa}. \quad (1)$$

The minimum size of a finite element (hexagonal volumetric element) is 3 mm (Figure 5). The model of a pipeline section with a wall thinning defect consists of 149556 elements, and the model with the use of a repair structure consists of 213316 elements. The minimum size of a grid element was chosen on the condition that the value of the maximum equivalent plastic strain changes by less than 5 % when the grid size is reduced twice.

The limiting condition of typical structures is usually determined by complex physical and mechanical phenomena, such as irreversible plastic deformation, triaxiality of stresses, subcritical fracture, interaction of subcritical defects, nucleation and propagation of macrofractures. Since pipelines with detected ECW are not characterized by sharp geometric stress concentrators, fracturing is predetermined by a ductile mechanism. A deformation criterion can be used for numerical prediction of the critical state by the mechanism of ductile fracture in the pipeline material under the internal pressure with the erosion-corrosion loss of metal [13]:

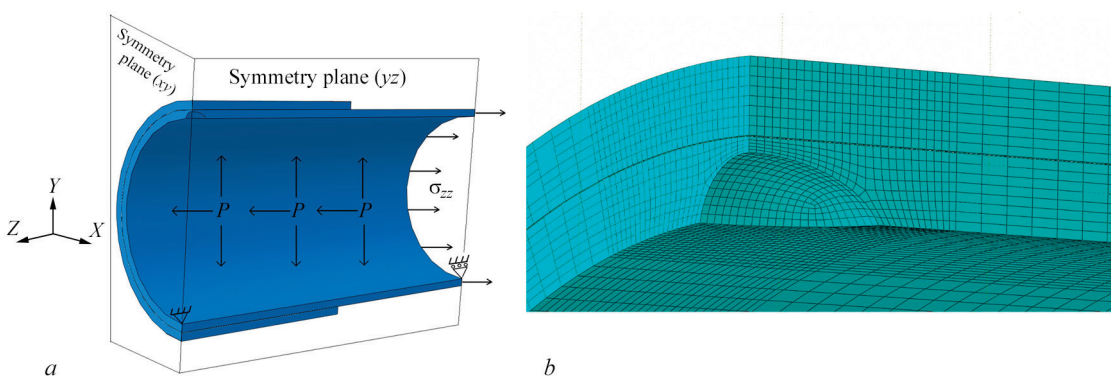

Figure 5. Finite element model of a rectilinear pipeline section with a wall thinning defect and a reinforcing structure: *a* — model scheme; *b* — finite element grid in the defect zone

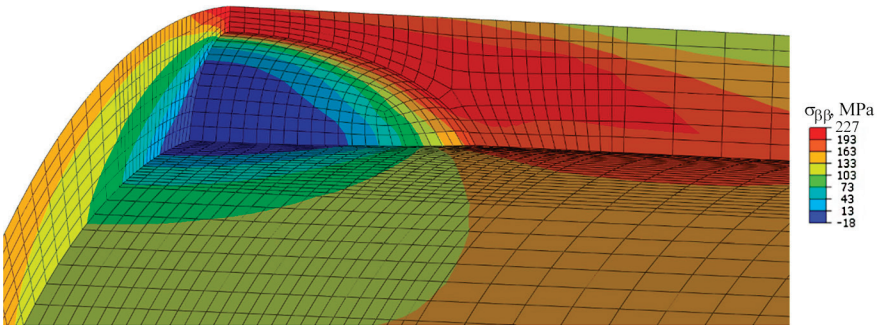

Figure 6. Distribution of circumferential stresses $\sigma_{\beta\beta}$ in the pipeline wall thinning defect zone without a reinforcing structure

$$\int \frac{d\varepsilon_i^p}{\varepsilon_c} > 1, \qquad (2)$$

where $d\varepsilon_i^p$ is an increment in the intensity of plastic deformations,

$$d\varepsilon_i^p = \frac{\sqrt{2}}{3}\sqrt{(d\varepsilon_{xx}^p - d\varepsilon_{yy}^p)^2 + (d\varepsilon_{yy}^p - d\varepsilon_{zz}^p)^2 + (d\varepsilon_{zz}^p - d\varepsilon_{xx}^p)^2 + \frac{3}{2}(d\varepsilon_{xy}^{p\,2} + d\varepsilon_{yz}^{p\,2} + d\varepsilon_{zx}^{p\,2})},$$

or in the tensor form $d\varepsilon_i^p = \frac{\sqrt{2}}{3}\sqrt{d\varepsilon_{ij}^p\, d\varepsilon_{ij}^p}$, $d\varepsilon_{ij}^p$ are the tensor components of the increment of intensity of plastic deformations; ε_c is a critical value of plastic deformation, which depends on the triaxiality of stresses, temperature, material heterogeneity, etc.

RESULTS OF FINITE ELEMENT ANALYSIS OF SSS

The results of SSS numerical analysis of the given pipeline section without a reinforcing structure showed that under the action of internal pressure P = 11.8 MPa in the zone of a thinning defect, the maximum circumferential stresses of up to 227 MPa (Figure 6) occur, which exceed the yield strength of the material (177 MPa) at the specified temperature T = 300 °C, and also, of course, exceed the rated allowable stress of static strength, which is determined according to PNAE G 7-002–86 [12] under the following conditions:

$$[\sigma] = \min\left\{\sigma_t / 2.6;\ \sigma_y / 1.5\right\}. \qquad (3)$$

The yield strength and tensile strength for steel 20 at a temperature T = 300 °C are σ_y = 177 MPa and σ_t = 363 MPa, respectively. According to (3), the allowable stress is equal to [σ] = 118 MPa.

But such an approach, based on a comparison of effective stresses in the pipeline wall due to internal pressure with the allowable static strength stresses for the pipeline material, is used in practice to select rated dimensions during designing, whereas to assess the limiting condition determined by the propagation of ductile fracture of the pipeline metal with an ECW defect, it is too conservative. Therefore, the abovementioned (2) approach based on the analysis of the results of the increment of intensity of plastic deformations in the defect zone is more rational.

According to the results of finite element modeling, the maximum intensity of plastic deformations in the ECW defect zone is 0.0112 (1.12 %) (Figure 7, *a*), which exceeds the "conditional" boundary deformation ε_c = 0.01 (1 %) [13]. This means that the conditions for the nucleation of ductile fracture of the material are realized. In order to prevent further deformations and fracture of the pipeline, a repair of a reinforcing structure of the type of a welded coupling band can be mounted. At the same time, the maximum stresses (227 MPa) still exceed the allowable stresses of static strength, but due to mounting a reinforcing structure, the maximum intensity of plastic deformation does not exceed the boundary deformation of 1 % (Figure 7, *b*).

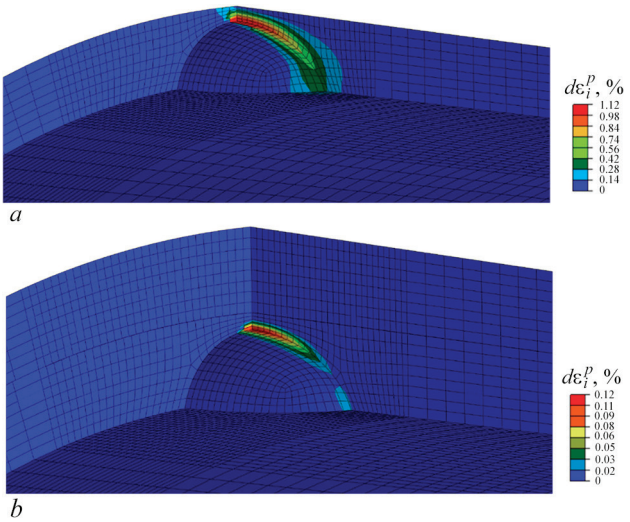

Figure 7. Distribution of the increment of intensity of plastic deformations $d\varepsilon_i^p$ of a pipeline section with a defect: *a* — without a reinforcing structure $d\varepsilon_i^p$ = 1.12 %; *b* — with a reinforcing structure $d\varepsilon_i^p$ = 0.12 % (by an order of value lower)

DETERMINATION OF THE MINIMUM WALL THICKNESS OF DEFECTIVE PIPELINE SECTIONS

In order to verify the correctness of using a deformation approach (2) for assessment of the limiting con-

Table 1. Comparison of minimum wall thicknesses in defective pipeline sections according to MT-T.0.0.03l24-18 Procedure and by the approach (2)

Pipeline parameters					MT-T.0.03.224-18		Approach (2)	
D, mm	s, mm	L/h, mm	T, °C	P, MPa	s_{min}, mm	$d\varepsilon_i^p$, %	s_{min}, mm	$d\varepsilon_i^p$, %
89	2.8	5.6/2.8	295	7.85	0.5	0.43	0.3	1.00
325	16	32/16	150	9.8	4.5	0.07	4.05	1.01
630	25	50/25	300	11.78	5	1.12	5.5	1.00
720	24	48/24	150	10.8	3	1.94	4.6	0.95

Note. s_{min} is the minimum acceptable thickness in the defect zone; $d\varepsilon_i^p$ is the intensity of plastic deformations.

dition according to the criterion of ductile fracture of a pipeline with an ECW defect, based on the analysis of the increment of intensity of plastic deformations in the defect zone, a comparison of the values of the minimum wall thickness of defective sections was made for different pipelines, determined according to the MT-T.0.03.224-18 Procedure [11] and according to the approach (2) by the method of finite element modeling. The results presented in Table 1, showed that the minimum wall thicknesses according to the Procedure in most variants are approximately equal to the results of the calculation based on the used deformation approach. Only in a one variant of the pipeline of 720×24 mm, the minimum wall thickness according to the Procedure is by 30 % lower than that calculated according to the criterion (2). I.e., the results of using the approach (2) of evaluating the critical state of ductile fracture of a pipeline with an ECW defect are consistent with the MT-T.0.03.224-18 Procedure [11, 18]. However, the wider capabilities of finite element modeling in terms of the accuracy of describing the physical and mechanical processes that determine the reliability of welded structures make it more rational for use, in particular when planning repair and restoration works.

EFFECT OF THE INITIAL GAP

The initial gap between the pipeline and repair structure significantly affects unloading of a defective pipeline section [15]. Too large value of the gap can lead to the fact that unloading a repair structure will not occur, and its mounting will not be effective. Therefore, in practice, the specialized equipment is used in order to clamp a reinforcing structure to the pipeline during mounting and provide a minimum gap. The results regarding the dependence of the increment value of intensity of plastic deformations on the gap value are shown in Figure 8.

The results of numerical prediction of the degree of unloading of the pipeline defect zone when mounting a band and a welded coupling showed that these repair structures operate to unload the wall thinning defect zone almost equally. The difference in the axial movements of a band and a coupling relative to the pipeline was not determined. But a welded coupling, due to the presence of a welded joint, additionally ensures tightness in case of defect propagation to a through defect. When the initial gap between the pipeline and a repair structure increases, the value of the maximum plastic deformations grows. With a value gap of 0.2 mm or more, a repair structure continues to operate to unload the given section, because under the action of internal pressure (11.8 MPa) in the pipeline (D = 630 mm, s = 25 mm), radial deformations arise, which amount to 0.22 mm, and the pipeline only selects the initial gap, and a band or a coupling do not reinforce a defective section. Therefore, such technological parameters as initial gap, drop of internal pressure before mounting a reinforcing structure and rising after its mounting are important.

EFFECT OF THICKNESS AND LENGTH OF A REINFORCING STRUCTURE

The effect of such geometric parameters as thickness and length of a repair structure on unloading a fractured pipeline section was considered. It is also worth noting that to facilitate the analysis, these models were built without taking into account the gap between a repair structure and a pipeline, that is, a repair

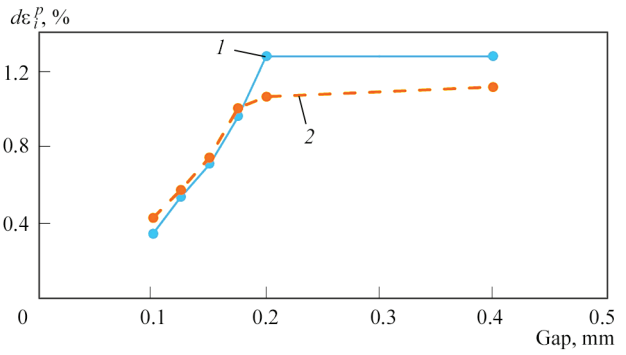

Figure 8. Dependences of maximum values of the increment of intensity of plastic deformations $d\varepsilon_i^p$ on the initial gap between the pipeline and a reinforcing structure: *1* — coupling; *2* — band

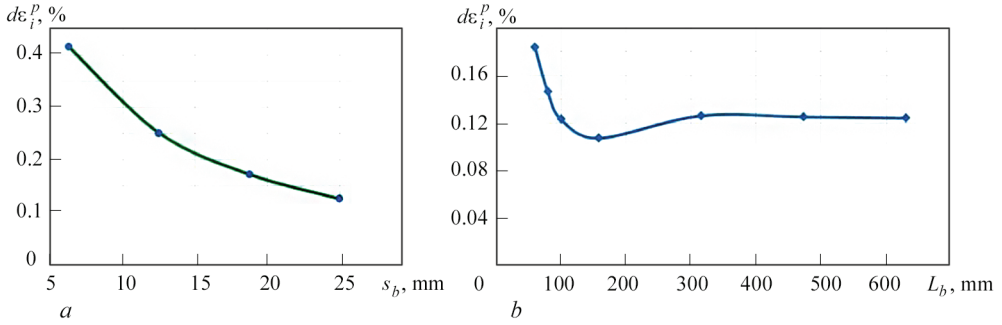

Figure 9. Dependence of maximum values of the increment of intensity of plastic deformations $d\varepsilon_i^p$ in the zone of the pipeline ECW defect (D = 630 mm, s = 25 mm) on the geometric parameters of a reinforcing structure; *a* — thickness s_b; *b* — half-length L_b

structure starts operating for unloading immediately. The results of the analysis of the effect of a change in the thickness at a constant length of a structure and a change in the length at a constant thickness, respectively, were shown on the diagrams (Figure 9).

As is seen from Figure 9, *a*, when the thickness of a repair structure decreases, the maximum value of the equivalent plastic deformation grows. On the other hand, when the half-length of a repair structure is reduced, as shown in Figure 9, *b*, from 630 mm to ≈300 mm, the intensity of plastic deformations almost does not increase, and when it decreases to 150 mm, their values are the lowest. From this it can be concluded that the use of a too long repair structure is not rational, and shortening its length to 300 mm will reduce the costs on repair of a fractured pipeline section.

EFFICIENCY OF UNLOADING DUE TO A REINFORCING STRUCTURE

To check the efficiency of the repair, the load on a defective pipeline section was calculated before the repair and after mounting a reinforcing structure. The ratio of unloading due to mounting a reinforcing structure is determined by the formula:

$$\eta = 1 - \frac{P_{ld}}{P_l}, \qquad (4)$$

where P_{ld} is the limit pressure in a defective pipeline section without a reinforcing structure; P_l is the pressure at which the ultimate plastic deformation ε_c = 0.01 is reached in a defective pipeline section with a reinforcing structure.

The calculated unloading ratios of the considered typical variants of the pipelines were recorded in Table 2. The determined values of the unloading ratios (0.43–0.51) of defective sections when using a reinforcing structure of the type of band with a thickness equal to the wall thickness for the pipelines of different sizes showed the high effectiveness of applying such structures.

PREDICTION OF LIFE OF A DEFECTIVE SECTION AFTER REPAIR

The residual service life of a defective pipeline section with an ECW defect can be estimated [16]:

$$t_r = \frac{s_r - s_{\min}}{w_{\text{ECW}}}, \text{ if } s_r > s_{\min}, \qquad (5)$$

where s_r is the residual wall thickness in the defect zone, mm; $s_{\min}$ is the calculated minimum acceptable wall thickness, mm; w_{ECW} is the rate of ECW defect propagation, mm/year.

The period of safe operation of a defective pipeline section with an ECW defect after mounting a reinforcing structure can be predicted from the condition of propagation of a wall thinning defect into a through defect. If a band or a coupling of the same thickness as the pipeline is mounted, then in the case of defect propagation, the through wall thinning will ensure strength, and for a coupling — also the tightness of the section. Thus, if we make an assumption about the

Table 2. Determination of unloading ratios η of pipeline sections when mounting a reinforcing structure

D, mm	s, mm	P, MPa	T, °C	$L/h/a$, mm	$s_{\min}$, mm	Critical pressure P, MPa		η
						P_{ld}	P_l	
89	2.8	7.85	295	5.6/2.8/2.3	0.5	7.85	16	0.51
325	16	9.8	150	32/16/13.5	2.5	9.8	18	0.46
630	25	11.78	300	50/25/20	5	11.78	21	0.44
720	24	10.8	150	48/24/19.5	4.5	10.8	19	0.43
820	18	1.57	188	36/18/16	2.0	6	11	0.45

constant propagation rate of an ECW defect, the term of safe operation t_r of a defective pipeline section with a mounted band or a coupling is:

$$t_r = \frac{s_r}{w_{\text{ECW}}}, \quad (6)$$

The propagation rate of an ECW defect w_{ECW} can be determined in a first approximation based on the data regarding the service life of a pipeline section before repair t_E, year, and the difference between the initial s and the residual s_r wall thickness in the ECW defect zone at the time of repair, mm:

$$w_{\text{ECW}} = \frac{s - s_r}{t_E}. \quad (7)$$

For example, for the pipeline D = 630 mm, s = 25 mm, which already operates under the action of an internal pressure of 11.8 MPa for 30 years, at a planned testing, an ECW defect with the size of 50×25 mm with a minimum thickness of 5 mm was revealed. Then, mounting a band of s_b = 25 mm thickness can extend the life of a defective section approximately by:

$$t_r = \frac{s_r \cdot t_E}{(s - s_r)} = 5 \cdot 30/(25–5) = 7.5 \text{ years}.$$

In the case of mounting a welded coupling, the life of a defective section can be even longer, which can be compared with the service life of a section after repair according to the traditionional technology of inserting a new spool, but this requires additional substantation of strength of circumferential welded joints under the action of internal pressure in the cavity between the pipe and the coupling.

The larger the residual thickness of the pipeline wall in the ECW zone and the lower rate of the defect propagation, the more rational is mounting a repair reinforcing structure, since the life of its use before the next repair will be longer. Thus, according to the requirements of GBN [17], mounting a band on the main pipeline is performed in the case when the maximum depth of single defects or group corrosion fractures does not exceed 50 % of the rated thickness of the pipeline wall.

CONCLUSIONS

According to the results of SSS analysis of a rectilinear section pipeline with an ECW defect under the action of internal pressure, it can be concluded that evaluation of the limiting condition of ductile fracture of the pipeline with an ECW defect on the basis of comparing the effective stresses in the pipeline wall from the internal pressure with acceptable stresses of static strength for the pipeline material is too conservative. It is more rational to use an approach based on the analysis of the formation of plastic deformations in the defect zone and the assumption that an increment of intensity of plastic deformations does not exceed a conditional boundary deformation, for example, ε_c = 1 %. The results of using this approach of assessment of the limiting condition of ductile fracture of the pipeline with an ECW defect are well consistent with MT-T.0.0.0.03.224-18 procedure, introduced into operation by the SE NNEGC “Energoatom” in 2019, which regulates the determination of acceptable thicknesses of NPP pipeline elements of carbon steels under the action of erosion-corrosion wear.

In order to substantiate the use of alternative repair technologies of pipelines for the needs of nuclear power engineering, mathematical models and means of their finite element implementation were developed to determine SSS and the limiting condition of a defective pipeline section when mounting a reinforcing structure of the type of a band or a welded coupling. The results of the finite element analysis have shown the following:

1. Unloading a defective pipeline section is significantly influenced by the initial gap between the pipeline and repair structure, since the presence of a gap causes that a repair structure begins unloading of a defective pipeline section only when this gap is selected by the pipeline due to radial deformation under the action of internal pressure during operation. It is rational to use the specialized equipment to clamp a reinforcing structure to the pipeline during its mounting.

2. Repair structures of the type of a band and a welded coupling operate to unload the wall thinning defect zone equally. The advantage of a band is a low labour intensiveness of its mounting and the possibility of its repeated use, and the advantage of a weld coupling is the guaranteed tightness in the case of defect propagation.

3. In most cases, it is rational to use reinforcing structures, whose thickness is equal to the thickness of the pipeline. When the thickness of a repair structure is reduced, the efficiency of unloading the wall thinning defect zone is significantly reduced.

4. The use of a long-length repair structure is not rational, since when the length changes to a certain value, the efficiency of unlodaing is not changed. For a local wall thinning defect, the optimal length of a reinforcing structure can be equal to half of the pipeline diameter. The use of a repair structure with an optimal length will allow reducing the costs on the repair structure material and simplifying its mounting.

5. These results can be used mainly in the repair of NPP technological pipelines, especially in the cas-

es, where repair by traditionional methods of cutting out a defective section and welding-in a new pipeline spool is not possible or rational for various reasons.

6.The calculated unloading ratio (0.43–0.51) of a defective section when mounting a reinforcing structure of a band type with a thickness equal to the wall thickness, showed high efficiency of using such structures for NPP pipelines of different sizes.

7. The term of safe operation of a defective section of the pipeline with an ECW defect after mounting a reinforcing structure can be determined from the condition of the propagation of a wall thinning defect. The larger the residual thickness of the pipeline wall in the ECW zone and the lower rate of the defect propagation, the more appropriate is mounting a repair structure, since the terms of its use before the next repair will be longer.

Thus, repair technologies of mounting reinforcing structures of the type of a band or a welded coupling can effectively reinforce NPP pipelines sections with wall thinning defects, restore their bearing capacity and may be recommended for introduction in NPP of Ukraine, mainly when repairing technological pipelines.

REFERENCES

1. Ageiev, S. (2021) Methodology for assessing the allowable wall thicknesses of carbon steel NPP piping under erosion-corrosion wear. *J. Nuclear and Radiation Safety*, 91(**3**), 32–42, DOI: https://doi.org/10.32918/nrs.2021.3(92).04
2. Ozhygov, L., Mytrofanov, A., Krainyuk, E. et al. (2013) Operational wear of pipelines of senond circuit of WWER-1000 power units. *Visnyk TNTU,* 69(**1**), 55–62 [in Ukrainian].
3. Gribok, A., Vivek Agarwal (2015) Flow-assisted corrosion in nuclear power plants. No. INL/EXT-15-36611-Rev000. Idaho National Lab. (INL), Idaho Falls, ID (United States).
4. Poulson, Bryan (2014) Predicting and preventing flow accelerated corrosion in nuclear power plant. *Int. J. of Nuclear Energy*, **2014**, 423295. DOI: https://doi.org/10.1155/2014/423295
5. NEA (2015) CODAP Topical Report: *Flow accelerated corrosion (FAC) of carbon steel and low alloy steel piping in commercial nuclear power plants*. OECD Publishing, Paris.
6. Vorona, G.V., Ananchenko, M.S., Makhnenko, O.V. (2023) Automation of procedure for determination of acceptance of erosion-corrosion wear in NPP pipelines. *Mech. Adv. Technol.*, 7(**1**), 113–121 [in Ukrainian]. DOI: https://doi.org/10.20535/2521- 1943.2023.7.1.272443
7. Makhnenko, V.I., Velikoivanenko, O.A., Rozynka, G.F., Pivtorak, N.I. (2010) Improvement of method for estimation of the risk of fracture within the thinning zone on walls of main pipelines. *The Paton Welding J.,* **5**, 10–14 [in Russian].
8. Vengrynyuk, T.P. (2010) Restoration and strengthening of gas-and-oil pipelines. *Prospecting and Development of Oil and Gas Fields*, 35(**2**), 136–139 [in Ukrainian]. DOI: https://rrngr.nung.edu.ua/ index.php/rrngr/article/view/591
9. Jaske, Carl E., Brian O. Hart, William A. Bruce (2006) *Updated pipeline repair manual*. No. R2269-01R.
10. ASME PCC-2-2018 (Revision of ASME PCC-2-2015): *Repair of Pressure Equipment and Piping. An American National Standard*.
11. (2019) MT-T.0.03.224-18: *Procedure for determination of acceptable thicknesses of NPP pipeline elements from carbon steels subjected to erosion-corrosion wear.* NAEK Energoatom [in Russian].
12. (1989) PNAE G-7-002–86: *Norms of strength analysis of equipment and pipelines of nuclear power plants.* Moscow, Energoatomizdat [in Russian].
13. Milenin, A., Velikoivanenko, E., Rozynka, G., Pivtorak, N. (2019) Probabilistic procedure for numerical assessment of corroded pipeline strength and operability. *Int. J. of Pressure Vessels and Piping*, **171**, 60–68. DOI: https://doi.org/10.1016/j.ijpvp.2019.02.003
14. Timoshenko, S.P., Vojnovsky-Kriger, S. (1966) *Plates and shells.* Moscow, Nauka [in Russian].
15. Makhenko, V.I., Velykoivanenko, O.A., Milenin, O.S., Pivtorak, G.P. (2012) Computational assessment procedure of efficiency of couplings (bands) mounting in the zone of wall thinning of main pipeline. *Problems of service life and safety of structures, constructions and machines.* Kyiv, PWI, 15–17 [in Ukrainian].
16. Kravchenko, V.P. (2017) Increase of safety and cost effectiveness of NPP by control of service life of secondary circuit pipelines. *Yadernaya i Radiatsionnaya Bezopasnost,* **3**, 25–29 [in Russian]. DOI: https://doi.org/10.32918/ nrs.2017.3(75).04
17. (2011) GBN B.3.1-00013741-12:2011. *Main gas pipelines, repair by arc welding in operating conditions.* Kyiv, Ministry of Energy and Coal Industry of Ukraine [in Ukrainian].
18. Orynyak, I., Ageiev, S., Radchenko, S., Zarazovskii, M. (2015) Local limit load analytical model for thick-walled pipe with axial surface defect. *J. of Pressure Vessel Technology*, 137(**5**), 051204. DOI: https://doi.org/10.1115/1.4029523

ORCID

G.V. Vorona: 0000-0002-9724-3759,
O.V. Makhnenko: 0000-0002-8583-0163,
O.S. Milenin: 0000-0002-9465-7710

CONFLICT OF INTEREST

The Authors declare no conflict of interest

CORRESPONDING AUTHOR

O.V. Makhnenko
E.O. Paton Electric Welding Institute of the NASU
11 Kazymyr Malevych Str., 03150, Kyiv, Ukraine.
E-mail: makhnenko@paton. kiev.ua

SUGGESTED CITATION

G.V. Vorona, O.V. Makhnenko, O.S. Milenin (2024) Effectiveness of unloading npp pipeline section with a pipe wall thinning defect by mounting a band or a welded coupling. *The Paton Welding J.*, **2**, 33–40.

JOURNAL HOME PAGE

https://patonpublishinghouse.com/eng/journals/tpwj

Received: 02.10.2023
Received in revised form: 11.12.2023
Accepted: 30.01.2024

DOI: https://doi.org/10.37434/tpwj2024.02.07

DEVELOPMENT OF OPTICAL-DIGITAL METHODS FOR NON-DESTRUCTIVE TESTING OF AEROSPACE THIN-WALLED SHELL STRUCTURES (REVIEW)

L.I. Muravsky

G.V. Karpenko Physico-Mechanical Institute of NASU
5 Naukova Str., 79060, Lviv, Ukraine

ABSTRACT

A series of studies on diagnostics and non-destructive testing of the stress-strain state of thin-walled cylindrical shell structures of aerospace engineering by optical-digital methods, in particular, three-dimensional (3D) digital image correlation (DIC) and laser photogrammetry methods, are described. The effectiveness and continuous improvement of these methods over the past decades has been noted. The results of experimental studies of composite and metal shell structures using the methods of 3D DIC are considered. The advantages of 3D DIC methods for simultaneous measurements of surface displacement and deformation fields using several digital image correlators located around the shell structure, over those 3D or 2D DIC methods that provide simultaneous registration of only a local area of the investigated surface using one correlator, were analyzed. The effectiveness of these methods for non-destructive testing of the dynamics of changes in the processes of the surface deformation and destruction under axial and radial loads, as well as for evaluating the knockdown factor of the thin-walled shell structure, is shown

KEYWORDS: shell structure, 3D digital image correlation, digital image correlator, composite cylindrical shell, metal cylindrical shell, knockdown factor, axial loads, radial loads

INTRODUCTION

Diagnostics and non-destructive testing of the stress-strain state of cylindrical shell structures is an important link in the entire process of building flying vehicles of aerospace engineering. One of the main ideas of these studies consists in the evaluation of the knockdown factor (KF) of a shell, which is determined as the ratio of critical load of a real cylinder, which leads to its buckling during longitudinal bending, to critical load of an ideal cylinder, as well as selecting optimal methods to increase KF.

Experimental studies of mechanical characteristics of thin-walled shells of space aircraft fuel tanks under the action of dynamic and static axial loads were carried out within the NASA space projects starting from the 50s of the 20th century. In particular, methodological NASA SP-8007 recommendations were worked out for the preliminary design of thin and moderately thick cylindrical shells under the action of axial compressive loads [1]. In the recommendations, it was proposed to evaluate the stability of a real cylinder using KF.

The mentioned recommendations initiated a series of experiments with composite and metal cylindrical shells, during which optical-digital methods were used to evaluate the geometric parameters of shells under the action of axial and other types of loads on them. In particular, the authors [2] studied thin-walled polymer laminated cylindrical shells reinforced with carbon fiber under combined and torsional loads. Laminated composite cylinders of the Z-series with a height of 510 mm, a radius of 250 mm and a thickness of 1.25 mm (thickness of each layer was 0.125 mm, orientation of the fibers of each layer differed from the orientation of the fibers of the adjacent layers) were manufactured at the Institute of Composite Structures and Adaptive Systems (ICSAS) of the German Aerospace Center [3, 4]. To evaluate the geometric parameters of nine composite cylinders (Z18, Z23, Z25, Z28–Z33), photogrammetric measurements were performed before applying loads, and at the moment of applying axial loads, non-destructive testing of transverse deflections of cylindrical walls caused by longitudinal bending was carried out using the design method of moiré fringes [2]. The conducted experiments showed that the eccentricity in the strength distribution of a shell has a great influence on the value of axial bending load, and this effect is weakened at combined loads.

At the beginning of the 21st century, the methodological NASA SP-8007 recommendations no longer took into account the potential of new materials, in particular, their mechanical and physical characteristics. The obtained differences between theoretical and experimentally obtained KF were quite significant [5–9]. As a result, numerous studies ended in a large range of KF, which was explained by many factors, in particular, imperfections of real shell structures (local defects, bends, pits,

damages to layers in the composite, etc.) [6, 9]. At the same time, the main attention was paid to axial loads, while radial (transverse) loads were practically not taken into account [10]. In addition, the existing methods and means were unable to control the entire process of changing the stress-strain state of the surface of shell structures from the beginning of applying loads to them until their complete destruction. The searches for new high-speed approaches to studies of displacement fields and surface deformations of shell structures throughout the whole field simultaneously led to the introduction into practice of experimental studies of hybrid optical-digital methods of registration, processing and analysis of large two- and three-dimensional information arrays, in particular, methods of digital image correlation (DIC).

APPLICATION OF DIC FOR NON-DESTRUCTIVE TESTING OF SHELL STRUCTURES

In recent years, researchers have paid special attention to improving the technical characteristics of shell structures, reducing their weight and cost, which ultimately leads to an increase in KF. One of the key factors in achieving high KF values was the use of optical-digital methods and systems of non-destructive testing of experimental and real shell structures of rocket and space engineering. Among them, the methods of three-dimensional (3D) DIC began to play a particularly important role, since with their help it is possible to restore a complete pattern of surface displacements and deformations simultaneously over the whole shell during its loading. At the same time, the experiments performed by such methods were combined with computer simulation, in particular with finite element methods (FEM), which take into account various imperfections of shells. The results of such complex studies made it possible to calculate KF for different types of shell structures.

The effectiveness of using DIC during loads of shell structures is predetermined, first of all, by the possibility of registering large areas of the surface of the research object in real time and the ability to ensure high accuracy of forming the fields of normal and tangential surface displacements and deformations. Due to the use of high-performance algorithms for surface image processing, it is possible to achieve such an error in calculating the restored field of displacements, which is comparable to 0.01 pixels in a matrix video sensor of a digital camera [11]. DIC is based on the correlation comparison of intensity distributions of speckle patterns of optically rough surfaces, diffuse media, or images of smooth surfaces with randomly placed spots applied by dye spraying or obtained by other methods. In DIC, only the intensity of the light field is a carrier of information, and the loss of phase information is compensated by a wider range of measuring surface displacements and deformations compared to digital speckle interferometry, shearography and digital holography. The formation of fields of displacements or deformations using DIC is performed by the correlation comparison of the $(m, n)^{th}$ fragment of an image of a deformed surface with the corresponding $(m, n)^{th}$ fragment of an image of the same surface, which is in the preliminary or initial state. For this purpose, two images are recorded with a digital camera, after which they are split in the computer into $M \times N$ of square or rectangular fragments containing an odd or even number of pixels, for example 15×15; 16×16; 31×31; 64×64 etc. Distinguished are two-dimensional (2D) DIC, in which the fields of in-plane (tangential) displacements and deformations are determined, and 3D DIC, in which the three-dimensional fields of displacements and deformations are determined, i.e. both in-plane and out-of-plane at the same time. Thousands of scientific papers have been devoted to 2D and 3D DIC methods and their use in various applied studies. For an in-depth study of these methods, it can be referred, for example, to [11–18].

There are several approaches to the formation of 3D fields of displacements and deformations of research objects using DIC methods. Among them, the most common belongs to M. Sutton's group [14, 19], according to which the same area of the surface is registered by two digital cameras from two points in space and, using the stereoscopic effect, all three orthogonal components of displacements are measured. They also developed the method of angular displacements [19], where the optical axes of two cameras are intersected on the research object. The method is quite flexible and is implemented using a simple optical system. However, here a larger part of the research object is outside the depth of field of projection lenses, which leads to the distorted image of its surface due to defocusing of a part of this image. To get rid of such defocusing, the Scheimpflug condition [20] is used, which improves the image, although it does not completely eliminate geometric distortions. The works of M. Sutton's group became the basis for the creation of optical-digital systems (ODS) of 2D and 3D DIC, i.e., digital image correlators, including the corresponding software. Among them, the non-contact 3D digital image correlation ARAMIS systems (produced by Trilion Quality Systems) [21] can be distinguished, which, in combination with VIC-3D software [22], make it possible to restore the fields of dynamic displacements and surface deformations of various objects during their loading.

DIC methods also make it possible to measure deformations of the 360° surface area of cylindrical shell structures that have a relatively large curvature. There are two main approaches to remote monitoring of such structures:

1. Simultaneous measurements of fields of displacements and surface deformations using several 3D digital image correlators located around the shell or in the area where destruction of a shell is most probable;

2. Measurements of surface fields of displacements and deformations using only one 3D or 2D digital image correlator, which registers either a series of speckle patterns of a cylindrical surface during its rotation, or a part of the surface that it covers.

The first approach was used in most of the works devoted to this topic, as it provides a synchronous registration of surface displacements and deformations over the 360° area of a shell and is fast. Moreover, the frame rate can be changed in a wide range depending on the experimental conditions. The second approach requires much less material costs, however, it is less effective, as it provides a simultaneous covering only of a part of the entire surface of the shell structure [23–27]. Sometimes it is applied in combination with the first approach and using several digital correlators for a more accurate analysis of a selected surface area containing local imperfections and defects [5, 6].

NON-DESTRUCTIVE TESTING OF COMPOSITE SHELL STRUCTURES OF AEROSPACE ENGINEERING

Most likely, 3D DIC was for the first time used to study loads on shell structures for rocket and space applications in [5], and the obtained results were supplemented in [6]. The main goal was to establish a more realistic lower bound descending exponential dependence of KDF on the ratio of the radius R of a cylindrical shell to its thickness t, i.e., on R/t, which would exceed the same traditional dependences [25, 28, 29] or dependences of KDF on the Batdorf parameter [7–9]. Six polymer laminated cylindrical shells Z07–Z12 reinforced with carbon fibers, with a heigth of 510 mm and a radius of 250 mm, manufactured at the ICSAS, were used for the experiments [30]. The cylinders contained four layers of 0.125 mm thickness with different fiber orientations; the total thickness of the cylinders was 0.5 mm. To assess the quality of the produced internal and external surfaces of the cylinders before applying loads, including to detect technological local damages, imperfections and defects, non-destructive testing was carried out by ultrasonic pulse-echo and photogrammetric methods. At the same time, delaminations were detected by the pulse-echo method, and surface inhomogeneities — by photogrammetry with the use of the ATOS measuring system [31]. Axial compressive loads were applied to cylindrical specimens using a hydraulic machine designed for axial compression of specimens [32]. Measurements of 3D fields of deformations during static and dynamic loads of shells were carried out using four 3D digital correlation ARAMIS systems [21]. Each system contains two high-speed digital cameras with the sizes of 1280×1024 pixels and the maximum frame rate of 920 Hz, which register approximately 100° of the shell surface segment, and four systems cover all 360° of the surface (Figure 1). Deformations of shells were determined by the displacements of their surfaces relative to the initial state before applying loads. To achieve rapid registration of local dynamic fields of surface displacements during its deformation, all four ARAMIS systems were placed in the selected area of the Z07 cylinder, where its destruction is most probable, covering a height of 450 mm and a field of view angle of ~40° (Figure 2), and recorded this area at a rate of 3680 Hz. It is shown that surface deformations at a dynamic load start from the location of the point bend in the center of the area, are accompanied by variable patterns of displacement field during longitudinal bend and end in a stable pattern of displacement field after buckling of a cylinder area. Here, also the procedure of non-destructive testing of the surface and internal layers of cylinders were considered before applying loads in order to detect technological local damages, imperfections and defects. Testing was carried out by a pulse-echo method as well as by a photogrammetric method using ODS ATOS [31].

Two sequences of displacement distributions for the same cylinder in unloaded and loaded states were obtained by authors of [30] using four ARAMIS systems over the whole shell area. The similar studies with the specimens of four-layer composite cylindrical shells Z15U500, Z17U500, Z18U500, Z20U500 and Z22U500 (height of 500 mm, radius of 250 mm, thickness of 0.5 mm, orientation of layers [+24°/–24°/+41°/–41°] were described in [33].

A work [10] has become a logical continuation of non-destructive tests of cylindrical shells produced at the ICSAS using ODS. Two test cylindrical specimens Z36 and Z37 of laminated carbon plastic composite, reinforced with carbon fiber (sequence of laying layers is [34/–34/0/0/53/–53]), of 800 mm height, 400 mm radius and 0.75 mm thickness were investigated, by applying axial compression and transverse (radial) loads on them. The axial compression was performed with the help of specially manufactured test equipment, and transverse loads — with the help

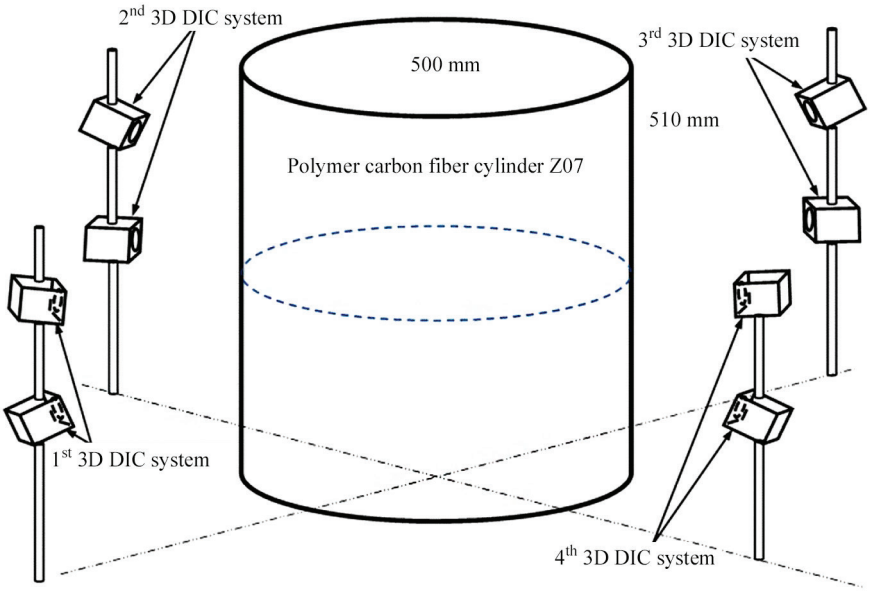

Figure 1. Simultaneous registration of 3D deformation fields of the entire outer surface of the cylinder during its static and dynamic loads with the use of four 3D DIC ARAMIS sytems

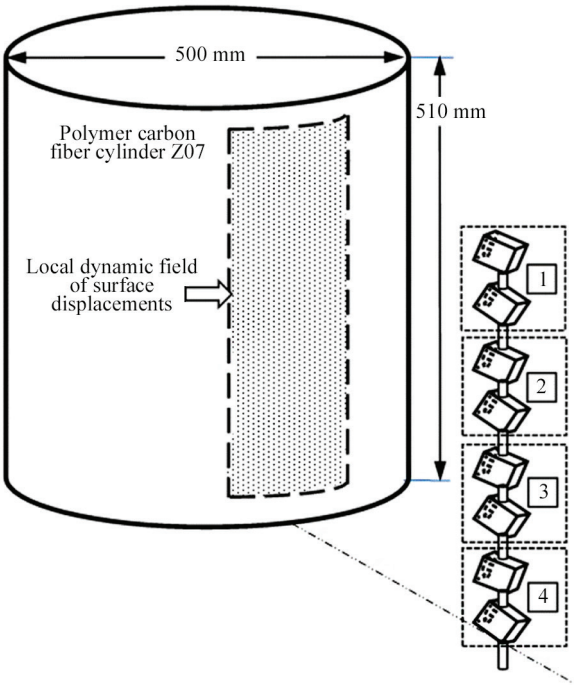

Figure 2. Simultaneous high-speed registration of the local field of surface displacements (angle of view is ~40°) during static and dynamic loads of the cylinder with the help of four 3D DIC ARAMIS systems: 1 — first system; 2 — second system; 3 — third system; 4 — fourth system

of a device containing magnets, operating in the radial direction. First, a constant transverse load, and then a monotonous growing compression load were applied. Transverse loads of 0–20 N were applied in three radial directions at angles of 30°, 150° and 210° for the specimen Z36 and at an angle of 30° for the specimen Z37. With the help of a scanning photogrammetric ATOS system, the initial geometric imperfections in the test cylinders were allocated, including surface and internal defects and damages, using the best-fit procedure (optimal approximation) to eliminate the displacement of a solid body from the results of measurements [34]. The fields of spatial deformations of the cylinder surface were determined by means of strain gauges. In addition to strain gauges, the 3D correlation ARAMIS Adjustable 12M system was also used [35] to study the spatial deformations of the surface. For this purpose, a spotty structure was deposited to the surface of the cylinder to simulate speckle pattern at the input of two digital cameras of the system. The obtained fields of displacements made it possible to detect surface depressions, convexes,

pits and other deviations from the ideal cylindricality during compression of test cylinders both before and after the appearance of a longitudinal bending of the specimens. In parallel with the experiments, FEM based on Abaqus Standard 6.14 (Implicit) software was used. By means of FEM, the dependencies between the axial load of longitudinal bend and the transverse disturbing load for the ideal model of a cylinder and the model of a cylinder with internal imperfections, including places with deviations of layer thickness and with changes in the volumetric fraction of carbon fibers were determined. It is shown that the results of calculating the spatial distribution of displacements of the surface of the cylinder model with the introduced imperfections are quite well correlated with the results of experiments with Z36 specimen performed using the ATOS scanner and the ultrasonic broadband scanner.

Due to the need in reducing the weight of structural elements of the aircraft engineering, the problem of manufacturing adapters of useful load and intermediate stages of a launch vehicle from composite materials is quite relevant. To solve the problem, in [36] it is proposed to use the methodology of FEM to predict the behavior of a shell structure during its longitudinal bend and compare the results of simulation with experimental data, obtained with the 3D digital correlation systems and strain gauges located on the cylinder surface. To simulate the real sizes of cylindrical shells of aerospace engineering, a new analytical scaling methodology was proposed. The methodology was used to design a composite cylinder of a reduced size, which has the same characteristics during buckling as a full-size multilayered composite cylinder. Such designing included, first and foremost, comparison of the dimensionless parameters of a scaled structure with a full-scale one [37]. Based on the results of designing, an experimental cylinder NDL-1 was produced of layers of a carbon fiber, joined by an epoxy material of 800 mm diameter, 1200 mm height and with a sequence of laying the composite layers [23/0/–23]. The NDL-1 design was a reduced version of a multilayered composite cylinder CTA8.1 with a diameter of 2.4 m, which was designed and tested as a part of the NASA SBKF project (Shell Buckling Knockdown Factor) [38]. Non-destructive testing of the experimental cylinder NDL-1 was carried out by the methods and means of photogrammetry and 3D DIC. To evaluate the available imperfections and deviations from cylindricality before applying axial loads to the experimental specimen NDL-1, optical scanning of the internal and outer surfaces was performed by the photogrammetric method. During the experiments, at the NASA Research Center in Langley, Virginia, surface displacements and deformations were measured by the system of strain gauges attached to the cylinder and 3D digital image correlators. In order to register artificial speckle patterns by the 3D DIC method, black ovals and circles of 4.5–6.0 mm were randomly applied to the light-coloured surface of the cylinder. Axial compressive loads of up to 3000 kN were performed using a specially designed test load installation. At the initial stage of the experiment, four 3D DIC systems were used with a slow rate of registering speckle patterns, which is equal to 1 frame/s. The cameras were placed at angles of 90° relative to each other. With an increase in the compressive axial load during the development of the longitudinal bending process and until buckling of the cylinder, four high-speed 3D DIC systems were used, the rate of registering speckle patterns in which was 20,000 frames/s. The comparative analysis of deformations of the cylinder surface during loads obtained on the one hand by 3D DIC systems, and on the other by means of FEM using ABAQUS 2017 product showed a satisfactory convergence of the experimental and simulation data. In particular, at the initial stage, axial loads calculated by FEM, differ from experimental ones by 0.04 %, and the estimated stiffness ratio by 1 % from the measured experimental one. However, the difference between these data increased during the longitudinal bending of the cylinder material. The behavior of the surface after buckling during the experiment was similar to its behavior. However, damages during longitudinal bending and after buckling that were registered experimentally, were not taken into account in FEM, which led to differences between the simulation and experimental data. The obtained results showed the possibility of using the method of studying full-scale cylindrical shell structures proposed by authors.

NON-DESTRUCTIVE TESTING OF METAL SHELL STRUCTURES OF AIRCRAFT ENGINEERING

In parallel with composite shell structures, metal ones made of aluminium alloys were also investigated. Starting from 2011, in NASA within the frames of designing and creation of a super-heavy launch vehicle Space Launch System (SLS) for a manned spacecraft, the research program was fulfilled to improve the KF evaluation procedures for full-scale specimens of metal shell structures made of aluminium alloys [39]. In particular, Correlated Solutions, Inc. submitted information on its website regarding a successful test of a full-scale cylindrical experimental specimen with a diameter of 27.5 feet (8.38 m) and 242 in (6.15 m) made of Al–Li 2195 alloy, in March 2011 at the NASA Marshall Space Flight Center [40]. The spec-

imen simulated the SLS fuel tank and was an analogous to the external fuel tank of a spacecraft Space Shuttle. Generating of displacement and deformation fields of the entire surface while applying axial, radial and other types of loads, was carried out with the help of 3D digital image correlators together with the VIC-3D software, developed and produced at the Correlated Solutions, Inc. On the outer white surface of the specimen, randomly distributed black ovals and circles of preset sizes that simulated a speckle structure were applied. In the experiment, seven 3D digital image correlators were used that covered the entire surface from 0 to 360° and tested it almost continuously. The specimen was gradually loaded up to more than 800,000 lbs, and the 3D DIC digital cameras registered the displacement fields at a rate of 3000 frames/s until the cylinder was completely destroyed.

More comprehensive information on the results of further studies with the full-scale cylindrical specimens and with the specimens of a smaller scale at the NASA Marshall Space Flight Center is reflected in [41, 42]. Data on the creation of two metal full-scale 27.5-foot test cylindrical shells and a deep study of their behavior during application of axial compressive loads, combined loads and internal pressure of the order of 1 psi (6895 Pa) is given in [41]. Here, the authors report about the designing and creation of eight small-scale cylinders with a diameter of 8 feet (2.44 m) and 6.5 feet (1.98 m) height, as well as two full-scale ETTA1 and ETTA2 cylinders. All of them were made of Al–Li 2195 alloy. ETTA1 and ETTA2 cylinders consisted of eight panels, welded between each other along the axial direction by the method of friction with stirring. The panels contained reinforced stiffened areas, weld zones and transitional areas between the weld zones and reinforced areas. ETTA1 was designed to evaluate the process of buckling under the action of axial uniform compression and therefore the panels in it had a low reinforcement. ETTA2 was designed to evaluate the same process for combined compression and bending loading. Therefore, it contained both panels presented in ETTA1 and much rigid panels.

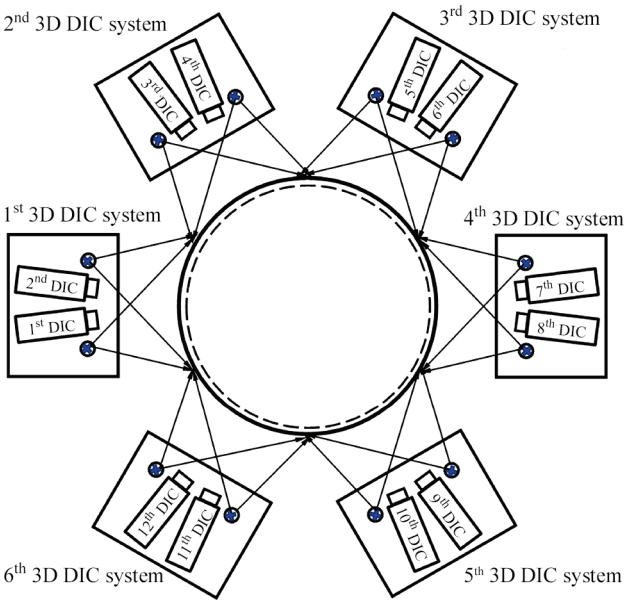

Figure 3. Scheme of experimental equipment for testing a metal full-scale cylinder containing six 3D DIC systems, each of which contains two digital cameras (DC) and two sources for illumination of the registered surface area

During the tests of full-scale cylinders, sensors of linear displacements, strain gauges, pressure sensors, photo/video systems and 3D DIC systems were used. 842 strain gauges were attached to ETTA1 and 1168 strain gauges were attached to ETTA2. Three-dimensional displacement and deformation fields of the outer surface were measured using six 3D DIC high-speed systems located round a circle around the cylinders (Figure 3). The systems monitored the transitional processes of a longitudinal bend of the surface and buckling of cylinders during their loads. For spatial referencing of these systems on the cylinders surface, markers in the form of a letter *L* were applied on the cylinder surface, which was formed with the help of a set of randomly distributed black squares that had approximately the same sizes as black circles and ovals on the white surface of the specimens. 3D DIC systems also measured local displacements and deformations between the markers pairs. The results of measurements with the help of these systems made it possible to evaluate the effect of local bending of elements of the outer lining of the cylinder and welds on the process of buckling of ETTA1 and ETTA2 cylinders. In particular, it is shown that the bend and groove of the lining adjacent to the axial welds in the specimens leads to the nonlinear reaction of loading on the axial deformation at lower levels of loading than it was supposed.

The work [42] shows the results of studies of two small-scale 8-ft test cylindrical shells TA07 and ITA02, made of Al–Li 2195 alloy. Each such cylinder contained three 120° arc segments welded with each other by friction with stirring. The configuration of stiffening elements was chosen on the basis of the NASA launch vehicle cylinder from the Ares 1 acceleration unit. For the multichannel testing, the data of displacements and deformations of the load surface, sensors of linear displacements and strain gauges were used. However, the main attention was paid to restoring three-dimensional displacement and deformation fields of the surface, which was measured with four two-camera 3D DIC. This system contained eight cameras and eight light radiation sources locat-

ed around the cylindrical shells. Digital cameras with the sizes of matrix video sensors of 2448×2048 pixels were located at angles of 45° relative to each other, which made it possible to cover the surface of the cylinder around the entire circle. To simulate speckle patterns, chaotically arranged black oval spots with the sizes of 0.45–0.70 in (1.14–1.78 cm) were applied to the white surface of the cylinders. The spot sizes were calculated taking into account the spatial resolution of the cameras. The frequency of image registration was 0.2 Hz. The obtained images were processed using the VIC-3D software developed in the Correlated Solutions, Inc. The largest errors of measured displacements of the cylinder surface were observed near their edges, and the smallest — along the central line round a circle of each cylinder, where the correlation between the installed 3D DIC was maximum. The results of measurements of 3D displacements of the surface of two 8-foot cylinders made it possible to upgrade the process of simulating loads of cylinders using FEM and thereby improving the forecasting of the phenomena of their buckling.

The similar studies with metal shells of smaller sizes were performed at the NASA Langley Research Center (Hampton, Virginia) [43, 44]. In [43], 3D DIC were used to determine the fields of displacements and deformations of surfaces of metal cylindrical shell structures. Round cylinders of 31 in length (0.7874 m), 9 in radius (0.2286 m) and 0.04 in thickness (0.102 cm) were manufactured of aluminium 2024 alloy. The tests were performed under the axial compression load and lateral disturbing load, which were applied in the radial direction in the middle of the cylinder length. To capture a complete pattern of displacement field over the entire cylindrical shell area during loads, three 3D DIC were used. To evaluate the test digital models of cylinder surface with an initial unloaded state and during axial and radial transverse loads, analysis using FEM and software Abaqus Standard and Abaqus Explicit products was performed. Simulation results and experimental data obtained by the 3D DIC method, performed during axial and transverse loads, showed some consistency between the restored axial and radial displacement fields, although FEM calculations of predicted local and global critical buckling loads exceeded those measured experimentally.

At the NASA Langley Research Center, a series of experiments with the abovementioned test cylinder TA07 with a diameter of 8 feet (2.44 m) and 6.5 feet (1.98 m) length made of Al–Li 2195 alloy was also conducted [44]. A number of new results were obtained and, in particular, it is shown that the cylinder load expected by FEM was 14.4 % less than that measured by 3D DIC. Four 3D DIC provided both slow registration of displacement field of the entire outer surface of the cylinder from 0° to 360° with a frequency of 0.2 Hz, as well as its rapid registration with a frequency of 5 kHz.

In [24], a cylindrical shell with a diameter of 1 m, height of 0.6 m and thickness of 1.5 mm was made of aluminium 2A14 alloy for evaluation of KF. 36 strain gauges, a laser scanning HandySCAN 3D system for panoramic optical surface measurements, as well as 3D DIC with the VIC-3D software were used to evaluate deformations of the surface under the action of axial loads. Using the HandySCAN 3D system, laser scanning of the cylinder surface before applying axial loads was performed to detect surface heterogeneities. 3D correlator was used to detect the mode structure of the deformed cylinder only after buckling of the cylinder under the action of compressive axial load. At the same time, it was moved six times around the cylinder to measure the shape of the entire surface. In the next work of almost the same author's team [25], four more cylinders of the same size and from the same aluminium 2Al4 alloy were manufactured for research. Here, the main attention was paid to the evaluation of defects and their heterogeneities, which were performed also by 3D DIC. At the same time, it is worth noting that the use of only one 3D DIC did not contribute to the reliable restoring of the displacement field throughout the cylinder surface field and it practically performed auxiliary functions during the experiment.

CONCLUSIONS

Versatile experimental studies conducted by a number of scientists in scientific laboratories and, in particular, at the NASA Langley Marshall Space Flight Center, as well as at the ICSAS of the German Aerospace Center, have shown high efficiency of procedures of construction and measuring surface fields of displacements and deformations and the detection of imperfections in the shell structures of aerospace engineering by means of non-destructive remote optical-digital methods, in particular, 3D DIC methods. The rationality of their use for both composite and metal shells has been shown. 3D DIC systems are ever more intensively used to obtain experimental data on the fields of deformations of shell cylindrical structures during axial compression and radial loads. Moreover, a tendency to increase a number of such systems during the synchronized registration of the cylinder surface is observed in order to increase an accuracy of restoring of all stages of applying such loads up to buckling and destruction of a shell. The use of photogrammetric systems of non-destructive testing of the cylindricity of shell structure surface in

an unloaded state in order to identify a variety of imperfections on the inner surface of cylindrical shells was also traditional. A prerequisite for the successful tests of experimental shell structures is a combination of FEM method with optical-digital non-destructive testing methods, in particular, with the 3D DIC method, and establishing a correspondence between the simulation results according to the experiment data.

REFERENCES

1. Weingarten, V.I., Seide, P., Peterson, J.P. (1968) *Buckling of thin-walled circular cylinders* (No. NASA SP-8007), NASA.
2. Meyer-Piening, H.R., Farshad, M., Geier, B., Zimmermann, R. (2001) Buckling loads of CFRP composite cylinders under combined axial and torsion loading–experiments and computations. *Composite. Structures*, 53(**4**), 427–435. DOI: https://doi.org/10.1016/S0263-8223(01)00053-8
3. Geier, B., Klein, H., Zimmermann, R. (1991) Buckling tests with axially compressed unstiffened cylindrical shells made from CFRP. In*: Buckling of Shell Structures, on Land, in the Sea and in the Air. Proc. of Int. Colloq. (Lyon, France)*, 498–507.
4. Geier B, Singh, G. (1997) Some simple solutions for buckling loads of thin and moderate thick cylindrical shells and panels made of laminated composite material. *Aerospace Sci. and Technol.*, **1**(1), 47–63. DOI: https://doi.org/10.1016/ S1270-9638(97)90023-7
5. Hühne, C., Rolfes, R., Tessmer, J. (2005) A new approach for robust design of composite cylindrical shells under axial compression. *Spacecraft Structures, Materials and Mechanical Testing,* **581**, 1–8.
6. Hühne, C., Rolfes, R., Breitbach, E., Teßmer, J. (2008) Robust design of composite cylindrical shells under axial compression — simulation and validation. *Thin-Walled Structures*, 46(**7–9**), 947–962. DOI: https://doi.org/10.1016/j.tws.2008.01.043
7. Wagner, H.N.R., Hühne, C., Niemann, S., Khakimova, R. (2017) Robust design criterion for axially loaded cylindrical shells — Simulation and validation. *Thin-Walled Structures*, **115**, 154–162. DOI: https://doi.org/10.1016/j.tws.2016.12.017
8. Wagner, H.N.R., Hühne, C. (2018) Robust knockdown factors for the design of cylindrical shells under axial compression: Potentials, practical application and reliability analysis. *Int. J. of Mechanical Sci.*, **135**, 410–430. DOI: https://doi.org/10.1016/j.ijmecsci.2017.11.020
9. Wagner, H.N.R., Hühne, C., Janssen, M. (2020) Buckling of cylindrical shells under axial compression with loading imperfections: An experimental and numerical campaign on low knockdown factors. *Thin-Walled Structures*, **151**, 106764. DOI: https://doi.org/10.1016/j.tws.2020.106764
10. Khakimova, R., Castro, S.G., Wilckens, D. et al. (2017) Buckling of axially compressed CFRP cylinders with and without additional lateral load: Experimental and numerical investigation. *Thin-Walled Structures*, **119**, 178–189. DOI: https://doi.org/10.1016/j.tws.2017.06.002
11. Pan, B., Qian, K., Xie, H., Asundi, A. (2009) Two-dimensional digital image correlation for in-plane displacement and strain measurement: A review. *Measurement Sci. and Technol.*, 20(**6**), 062001. DOI: https://doi. org/10.1088/0957-0233/20/6/062001
12. Sutton, M.A., Wolters, W.J., Peters, W.H. et al. (1983) Determination of displacements using an improved digital correlation method. *Image and Vision Computing*, 1(**3**), 133–139. DOI: https://doi.org/10.1016/0262-8856(83)90064-1
13. Sjödahl, M. (1998) Some recent advances in electronic speckle photography. *Optics and Lasers in Engineering*, 29(**2–3**), 125–144. DOI: https://doi.org/10.1016/S0143-8166(97)00081-X
14. Sutton, M.A., McNeill, S.R., Helm, J.D., Chao Y.J. (2000) Advances in two-dimensional and three-dimensional computer vision. In: *Photomechanics, Berlin, Heidelberg*, 323–372.
15. Sutton, M.A., Orteu, J.J., Schreier, H. (2009) *Image correlation for shape, motion and deformation measurements: Basic concepts, theory and applications.* Springer Science & Business Media.
16. Muravskyi, L.I. (2010) *Methods of speckle-correlation for study of mechanical properties of structural materials.* Kyiv, Naukova Dumka [in Ukrainian].
17. Dufour, J.-E., Hild, F., Roux, S. (2015) Shape, displacement and mechanical properties from isogeometric multiview stereocorrelation. *The J. of Strain Analysis for Engineering Design*, 50(**7**), 470–487. DOI: https://doi.org/10.1177/0309324715592530
18. Lobanov, L.M., Muravskyi, L.I., Pivtorak, V.A., Voronyak, T.I. (2017*) Monitoring of stressed state of structure elements using electromagnetic waves of optical range. Vol. 3: Technical diagnostics of materials and structures:* Refer. Book, In: 8 Vol., Ed. by Z.T. Nazarchuk. Lviv, Prostir-M [in Ukrainian].
19. Luo, P.F., Chao, Y.J., Sutton, M.A., Peters, W.H. (1993) Accurate measurement of three-dimensional deformations in deformable and rigid bodies using computer vision. *Experimental Mechanics*, 33(**2**), 123–132. DOI: https://doi. org/10.1007/BF02322488
20. Prasad, A.K., Jensen, K. (1995) Scheimpflug stereocamera for particle image velocimetry in liquid flows. *Applied Optics*, 34(**30**), 7092–7099. DOI: https://opg.optica.org/ao/abstract.cfm?URI=ao-34-30-7092
21. *Trilion Quality Systems*. https://www.trilion.com/aramis
22. *Correlated Solutions, Inc. VIC-3D.* https://www.correlatedsolutions.com/vic-3d
23. Zhao, C., Matsuda, H., Lou, S. et al. (2013) Visualization of buckling on thin-walled cylindrical shell by digital image correlation method. *Applied Mathematics and Information Sci.*, 7(**3**), 999–1004. DOI: https://digitalcommons.aaru. edu.jo/amis/vol07/iss3/18
24. Wang, B., Zhu, S., Hao, P. et al. (2018) Buckling of quasi-perfect cylindrical shell under axial compression: A combined experimental and numerical investigation. *Int. J. of Solids and Structures*, **130–131**, 232–247. DOI: https://doi.org/10.1016/j.ijsolstr.2017.09.029
25. Wang, B., Du, K., Hao, P. et al. (2019) Experimental validation of cylindrical shells under axial compression for improved knockdown factors. *Int. J. of Solids and Structures*, **164**, 37–51. DOI: https://doi.org/10.1016/j. ijsolstr.2019.01.001
26. Labans, E., Bisagni, C. (2019) Buckling and free vibration study of variable and constant-stiffness cylindrical shells. *Composite Structures*, **210**, 446–457. DOI: https://doi.org/10.1016/j.compstruct.2018.11.061
27. Castro, S. G., Almeida Jr, J.H.S., St-Pierre, L., Wang, Z. (2021) Measuring geometric imperfections of variable — angle filament–wound cylinders with a simple digital image correlation setup. *Composite Structures*, **276**, 114497. DOI: https://doi.org/10.1016/j.compstruct.2021.114497
28. Peterson, J.P., Seide, P., Weingarten, V.I. (1968) *Buckling of thin-walled circular cylinders. NASA SP-8007* (Technical Report).
29. Arbocz, J, Starnes Jr., J.H. (2002) Future directions and challenges in shell stability analysis. *Thin-Walled Structures*, **40**(9), 729–754. DOI: https://doi.org/10.1016/S0263-8231(02)00024-1

30. Degenhardt, R., Kling, A., Klein, H. et al. (2007) Experiments on buckling and postbuckling of thin-walled CFRP structures using advanced measurement systems. *Int. J. of Structural Stability and Dynamics*, 7(**2**), 337–358. DOI: https://doi.org/10.1142/S0219455407002253
31. *ATOS Compact Scan. Mobile 3D scanner for a wide range of applications.* https://www.gom.com/en/products/3d-scanning/atos-compact-scan?keyword=atos%20compact%20 scan&device=c&network=g&gclid=Cj0KCQjw1OmoBhDXARIsAAAYGSFwdUnAc-Y5Q4QgmagrJ-khc0hV-e-Dx_jQMVBlQsaQp71M8fQuoMcaAq5AEALw_wcB
32. Hühne, C., Zimmermann, R., Rolfes, R., Geier, B. (2002) *Sensitivities to geometrical and loading imperfections on buckling of composite cylindrical shells.* In: *Proc. of the European Conf. on Spacecraft Structures, Materials And Mechanical Testing*, *CNES, Toulouse, France*.
33. Degenhardt, R., Kling, A., Bethge, A. et al. (2010) Investigations on imperfection sensitivity and deduction of improved knock-down factors for unstiffened CFRP cylindrical shells. *Composite Structures*, 92(**8**), 1939–1946. DOI: https://doi.org/10.1016/j.compstruct.2009.12.014
34. Khakimova, R., Wilckens, D., Reichardt, J. et al. (2016) Buckling of axially compressed CFRP truncated cones: Experimental and numerical investigation. *Composite Structures*, **146**, 232–247. DOI: https://doi.org/10.1016/j.compstruct.2016.02.023
35. *ARAMIS Adjustable.* https://www.gom.com/en/products/3d-testing/aramis-adjustable
36. Rudd, M.T., Eberlein, D.J., Waters, W.A. et al. (2023) Analysis and validation of a scaled, launch-vehicle-like composite cylinder under axial compression. *Composite Structures*, 304(**1**), 116393. DOI: https://doi.org/10.1016/j. compstruct.2022.116393
37. Uriol Balbin, I., Bisagni, C., Schultz, M.R., Hilburger, M.W. (2020) Scaling methodology applied to buckling of sandwich composite cylindrical shells. *AIAA J.*, 58(**8**), 3680–3689. DOI: https://doi.org/10.2514/1.J058999
38. Schultz, M.R., Sleight, D.W., Gardner, N.W. et al.(2018) Test and analysis of a buckling-critical large-scale sandwich composite cylinder. In: *2018 AIAA/ASCE/AHS/ASC Structures, Structural Dynamics, and Materials Conf.*, 1693.
39. "*Focus on Marshall" Highlights 10 Years of Space Station Support and World's Largest "Can Crusher"*. YouTube, May, 20, 2013. https://www.youtube.com/watch?v=NLkzSchXXzE
40. *NASA Buckling Test with Real Time Module (Correlated Solutions, Inc., 2023)*. https://www.correlatedsolutions.com/ application/nasa-buckling-test-real-time
41. Lovejoy, A.E., Hilburger, M.W., Gardner, N.W. (2018) Test and analysis of full-scale 27.5-foot-diameter stiffened metallic launch vehicle cylinders. In: *2018 AIAA/ASCE/ AHS/ASC Structures, Structural Dynamics, and Materials Conf., 1989*.
42. Gardner, N.W., Hilburger, M.W., Haynie, W.T. et al. (2018) Digital image correlation data processing and analysis techniques to enhance test data assessment and improve structural simulations. In: *2018 AIAA/ASCE/AHS/ASC Structures, Structural Dynamics, and Materials Confer.,* 1698.
43. Haynie, W., Hilburger, M., Bogge, M. et al. (2012) Validation of lower-bound estimates for compression-loaded cylindrical shells. In: *53rd AIAA/ASME/ASCE/AHS/ASC Structures, Structural Dynamics and Materials Conf. 20th AIAA/ ASME/ AHS Adaptive Structures Conf. 14th AIAA, 1689*.
44. Hilburger, M.W., Lindell, M.C., Waters, W.A., Gardner, N.W. (2018) Test and analysis of buckling-critical stiffened metallic launch vehicle cylinders. In: *2018 AIAA/ASCE/ AHS/ASC Structures, Structural Dynamics, and Materials Conf.,* 1697.

ORCID

L.I. Muravsky: 0000-0001-8839-2819

CORRESPONDING AUTHOR

L.I. Muravsky
G.V. Karpenko Physico-Mechanical Institute of NASU
5 Naukova Str., 79060, Lviv, Ukraine.
E-mail: muravskyleon@gmail.com

SUGGESTED CITATION

L.I. Muravsky (2024) Development of optical-digital methods for non-destructive testing of aerospace thin-walled shell structures (Review). *The Paton Welding J.*, **2**, 41–49.

JOURNAL HOME PAGE

https://patonpublishinghouse.com/eng/journals/tpwj

Received: 06.10.2023
Received in revised form: 11.12.2023
Accepted: 03.02.2024

SUBSCRIPTION–2024

«The Paton Welding Journal» is Published Monthly Since 2000 in English, ISSN 0957-798X, doi.org/10.37434/tpwj.

«The Paton Welding Journal» can be also subscribed worldwide from catalogues subscription agency EBSCO.

If You are interested in making subscription directly via Editorial Board, fill, please, the coupon and send application by Fax or E-mail.

12 issues per year, back issues available.

$384, subscriptions for the printed (hard copy) version, air postage and packaging included.

$312, subscriptions for the electronic version (sending issues of Journal in pdf format or providing access to IP addresses).

Institutions with current subscriptions on printed version can purchase online access to the electronic versions of any back issues that they have not subscribed to. Issues of the Journal (more than two years old) are available at a substantially reduced price.

Subscription Coupon **Address for Journal Delivery**			
Term of Subscription Since	**20**	**Till**	**20**
Name, Initials			
Affiliation			
Position			
Tel., Fax, E-mail			

The archives for 2009–2022 are free of charge on
www://patonpublishinghouse.com/eng/journals/tpwj

ADVERTISING
in «The Paton Welding Journal»

External cover, fully-colored:
First page of cover
(200×200 mm) — $350
Second page of cover
(200×290 mm) — $275
Third page of cover
(200×290 mm) — $250
Fourth page of cover
(200×290 mm) — $300

Internal cover, fully-colored:
First/second/third/fourth page
(200×290 mm) — $200

Internal insert:
(200×290 mm) — $170
(400×290 mm) — $250

- Article in the form of advertising is 50 % of the cost of advertising area
- When the sum of advertising contracts exceeds $1001, a flexible system of discounts is envisaged
- Size of Journal after cutting is 200×290 mm

Address
11 Kazymyr Malevych Str., 03150, Kyiv, Ukraine
Tel./Fax: (38044) 205 23 90
E-mail: journal@paton.kiev.ua
www://patonpublishinghouse.com/eng/journals/tpwj